Bayesian Estimation of Transient Engine Exhaust Composition from Fourier Transform Infrared Spectroscopy Measurements

David Hilton Wilson
Marquette University

Recommended Citation

Wilson, David Hilton, "Bayesian Estimation of Transient Engine Exhaust Composition from Fourier Transform Infrared Spectroscopy Measurements" (2019). *Dissertations (1934 -)*. 1016.
https://epublications.marquette.edu/dissertations_mu/1016

BAYESIAN ESTIMATION OF TRANSIENT ENGINE EXHAUST COMPOSITION FROM FOURIER TRANSFORM INFRARED SPECTROSCOPY MEASUREMENTS

by

David Wilson, M.S.M.E

A Dissertation submitted to the Faculty of the Graduate School,
Marquette University,
in Partial Fulfillment of the Requirements for
the Degree of Doctor of Philosophy

Milwaukee, Wisconsin

May 2019

ABSTRACT
BAYESIAN ESTIMATION OF TRANSIENT ENGINE EXHAUST COMPOSITION FROM FOURIER TRANSFORM INFRARED SPECTROSCOPY MEASUREMENTS

David Wilson, M.S.M.E

Marquette University, 2019

Mobile sources comprise a substantial portion of anthropogenic volatile organic compound (VOC) emissions worldwide. Many research efforts have sought to elucidate the relationships between VOC emissions and engine operating conditions, which are largely transient in real-world scenarios. However, the literature remains dominated by steady-state data and batch measurements of total emissions over entire driving cycles. Fourier transform infrared (FTIR) spectroscopy is a promising technique for obtaining instantaneous, time-resolved VOC measurements. However, FTIR measurements of chemically evolving samples are biased due to sample recirculation and signal non-stationarity. To extract accurate emissions profiles from biased FTIR measurements of transient emissions, an Unscented Kalman filter (UKF) is developed. The UKF is a model-based algorithm which incorporates sample mixing dynamics, a measurement model of non-stationarity effects, and noise statistics to infer instantaneous exhaust composition in a statistically optimal manner. The sample mixing model is developed and validated using computational fluid dynamics and mixing network simulations. Non-stationarity effects – which produce FTIR measurements that are unevenly weighted by spectral IR powers at/near the centerburst position of the modulating mirror – are mathematically and experimentally proven to emerge due to alternating scan directions. A numerical method is developed to estimate the degree of centerburst weighting on measurements of unique VOCs, which is mathematically shown to scale with spectral absorbance broadening. The UKF is experimentally validated by flowing transient, trace quantities of acetylene and propylene through a FTIR gas cell and filtering the resulting measurements. Average improvements of 58% and 51% are achieved for estimations of acetylene and propylene composition, respectively, compared to unfiltered FTIR measurements. The UKF is employed to investigate transient effects on emissions of various fuel component VOCs (cyclohexane, ethanol and pentane) and intermediates (1,3 butadiene, acetylene, ethylene, formaldehyde and methane) from a spark-ignited, port fuel-injected gasoline engine under various load ramps. Deterministic transient effects are evident, as emissions deviate from quasi-steady predictions by statistically significant quantities in 14 of the 21 species/load profile combinations explored. For the intermediate species, greater quasi-steady prediction errors correspond to faster ramp rates, while greater errors occur during moderate load ramps for fuel component species.

ACKNOWLEDGEMENTS

David Wilson, M.S.M.E

I would like to first gratefully acknowledge my advisor, Dr. Casey Allen. Five years ago, I arrived at your office as a raw, inexperienced undergraduate who was completely unaware of how graduate research worked. Whether out of faith in my abilities, or desperation for a graduate student as a recently hired assistant professor, you decided to take me on. Because of your exceptional guidance, expertise and genuine concern for my development, I exceeded my expectations as a researcher and was even able to pursue a PhD. Working with you has been gratifying and joyous. I am proud of what we have accomplished together and appreciative of the relationship we have built. Thank you for taking a chance on me.

Thank you to my dissertation committee: Drs. Somesh Roy, Simcha Singer, Henry Medeiros and Matti Maricq. Dr. Roy, thank you for your helpful input during our weekly research meetings. I greatly benefitted from having to regularly field your difficult, thought-provoking questions. Those encounters led to important research insights and improved my presentation skills. Also, thank you for sharing your CFD expertise with me. Dr. Singer, thank you for being an integral part of my entire graduate school experience. From serving on both of my graduate committees, to having me as a teaching assistant and permitting me to teach a thermodynamics lecture, you have provided me valuable opportunities for growth. Dr. Medeiros, thank you for skillfully teaching me the fundamentals and applications of Bayesian estimation. What I learned from your class undoubtedly accelerated and improved the quality of my research. Dr. Maricq, thank you for agreeing to join my committee from Ford Motor Company, and for your willingness to share your FTIR expertise via email correspondence to, at the time, two complete strangers in Dr. Allen and me. Your service and generosity is truly appreciated.

Thank you to the current and previous graduate students within Dr. Allen's group with whom I've had the pleasure of crossing paths: John Neuman, Jack Rehn, Jenna Ezzell, Mark Carioscio, Ashley Hatzenbihler, David Roulo and Dylan Lehmier. Each and every one of you has positively impacted my work and overall experience as a graduate student. Thank you for allowing me to be a part of a team of exceptional individuals. I am proud to be a T_{ad}pole.

To Lisa, thank you for your unwavering love and support throughout my entire graduate career. When I came to you almost three years ago with the news of an opportunity to continue my graduate career to pursue a PhD, part of me was expecting a response along the lines of "Maybe you should consider a well-paying industry job so we can move out of our duplex." (which I would have totally understood, by the way). Instead, it was nothing but excitement and approval, knowing fully the sacrifices it would require from both of us. Thank you for being in my corner during these last four years, and for your understanding of the occasional (perhaps frequent) late night at work. You have been my rock through this process, and your companionship has made the challenging times bearable and the good times even better.

Last but not least, I owe a special thanks to my family. Through my entire life, you have gone above and beyond to ensure that I succeed, and have lovingly pushed me to pursue whatever interest captivated me at the time, whether it was boy scouts, basketball, or combustion research. Your unrivaled love and support have made this pursuit, and life in general, worth it. To my late father, thank you for your love, strength, and being my biggest advocate in my decision to seek a PhD. You are an inspiration, and this dissertation is dedicated to you.

TABLE OF CONTENTS

LIST OF TABLES

LIST OF FIGURES

NOMENCLATURE

ANN	artificial neural network
BEM	Bayesian estimation model
BMEP	brake mean effective pressure
CAN	controller area network
CFD	computational fluid dynamics
CI	chemical ionization
CO	carbon monoxide
ECS	engine control system
FID	flame ionization detector
FTIR	Fourier transform infrared spectroscopy
FTP	Federal Test Procedure
GA	genetic algorithm
GC	gas chromatography
GHG	greenhouse gas
HC	hydrocarbons
HCCI	homogeneous charge compression ignition
IMEP	indicated mean effective pressure
IR	infrared
MN	mixing network
MOVES	Motor Vehicle Emissions Simulator
MS	mass spectrometry
NMOG	non-methane organic compounds
NO	nitric oxide
NO_x	oxides of nitrogen
OPD	optical path difference
PM	particulate matter
PNET	PowerNet control system
PTR	proton transfer reaction
TDLAS	tunable diode laser absorption spectroscopy
UKF	Unscented Kalman filter
VOC	volatile organic compounds

ms	millisecond
lpm	liters per minute
ppm	parts per million
s	seconds
sccm	standard cubic centimeters per minute
slpm	standard liters per minute

a	state transition model
b	forcing function
c	measurement model
c_w	centerburst weight
$\boldsymbol{e}$	innovation
f	frequency
I	intensity
$\boldsymbol{K}$	Kalman gain
m	mass

$\dot{m}$	mass flow rate
$\dot{m}_{pf}$	mass flow rate through plug flow pathway of the mixing network
$\boldsymbol{MW}$	molecular weights of species of interest
MW_{mix}	molecular weight of total gas cell sample
N_x	number of states
$\widetilde{\boldsymbol{P}}$	state error covariance matrix
$\boldsymbol{R}$	covariance matrix
Si	sine integral
t	time
t_s	temporal set point intervals
$\boldsymbol{u}$	input
$\dot{V}$	volume flow rate
$\boldsymbol{v}$	measurement noise
v_Z	FTIR species measurement noise
W	weight
$\boldsymbol{w}$	process noise
$w_{Z_{in}}$	gas cell inlet composition process noise
x	optical path difference
$\boldsymbol{x}$	system state
$\boldsymbol{y}$	measurement
$\boldsymbol{Z}_{cell}$	mass composition within FTIR gas cell
$\boldsymbol{Z}_{cell,0}$	mass composition within FTIR gas cell at centerburst location
$\boldsymbol{Z}_{cell,\delta}$	mass composition within FTIR gas cell at maximum optical path difference
$\boldsymbol{Z}_{cell,t-1}$	mass composition within FTIR gas cell at previous time
$\boldsymbol{Z}_{in}$	mass composition entering FTIR gas cell
$\boldsymbol{Z}_{in,t-1}$	mass composition entering FTIR gas cell at previous time

β	spectral intensity at centerburst position
γ	slope of intensity change with respect to optical path difference
δ	maximum optical path difference
κ	tuning parameter
λ	equivalence ratio
ν	wavenumber
$\boldsymbol{\xi}$	predicted measurement residual
Π	square function
$\sigma_{Z_{in}}$	inlet composition set point standard deviation
τ	effective FTIR gas cell time constant
$\boldsymbol{X}$	state sigma point
$X_{\nu}{}^{2}$	reduced chi-square statistic
$\boldsymbol{\Upsilon}$	measurement sigma point
ω	angular engine speed

^	prediction
~	error

CHAPTER 1 INTRODUCTION

Combustion is currently the primary source of power for transportation and will likely remain so during the next few decades due to its considerable power density and our current infrastructure. Despite its advantages, combustion produces harmful greenhouse gases such as carbon dioxide, oxides of nitrogen and volatile organic compounds (VOCs) which impact the radiative properties of the atmosphere, resulting in adverse effects on the climate. While substantial emissions reductions have been achieved over the past few decades, more progress is needed to meet future regulations and mitigate/reverse unfavorable climate trends that have already emerged. Despite the fact that engines are primary greenhouse gas emitters, and that real-world engine operation is predominantly transient, the relationships between engine speed/load history and emissions are currently not well understood. This is especially true of speciated VOC emissions, which are difficult to accurately measure in a time-resolved manner. Presented herein is the development, validation and application of an Unscented Kalman filter (UKF) for obtaining time-resolved, comprehensive estimations of transient engine exhaust composition from Fourier transform infrared spectroscopy (FTIR) measurements. The UKF is a model-based Bayesian estimator which effectively filters out transient biasing effects that arise during FTIR measurements of chemically evolving samples due to recirculation and signal non-stationarity. By improving the fidelity of transient speciation measurements, clearer insights into the relationships between engine operation conditions and VOC emissions can be uncovered.

This dissertation is outlined as follows. First, background information regarding transient VOC emissions is provided in Chapter 2. This includes specific atmospheric impacts and existing experimental investigations of VOC emissions, as well as an overview of diagnostic techniques capable of comprehensive speciation. FTIR spectroscopy is then introduced, followed by a discussion the biasing effects of sample recirculation and signal non-stationarity, which limit the applicability of this technique to transient analysis. This discussion motivates the development of a UKF for effectively filtering out transient biasing effects within FTIR measurements. The UKF is initially formulated in Chapter 3, which begins with a discussion of the underlying theory of Bayesian estimation and the fundamental equations within the UKF. This is followed by the development of a simple model of the mixing dynamics within a FTIR gas cell, which is validated using computational fluid dynamic and mixing network simulations. The mixing model is incorporated within the UKF to combat recirculation effects by estimating inlet composition according to the evolution of FTIR gas cell composition measurements. Chapter 4 exclusively addresses signal non-stationarity effects, which were unknown at the onset of this work. The chapter begins with an experimental illustration of non-stationarity bias, which introduces artificial oscillations into measured transient composition profiles. These oscillations are shown to be caused by uneven weighting of composition values that occur when the moving mirror within the Michelson interferometer is near the centerburst position, and alternating scan directions. A mathematical proof of uneven weighting during transient measurements confirms these observations, which is expanded to predict centerburst weighting values for unique species. The UKF is modified to include the effects of centerburst weighting. Experimental validation of the modified UKF is performed by flowing known, transient quantities of acetylene and propylene through a FTIR, and filtering the resulting measurements. Chapter 5 details an experimental investigation of transient effects on the emissions of various VOCs (such as cyclohexane, ethanol, pentane, acetylene, ethylene, formaldehyde and methane) from a gasoline engine using FTIR spectroscopy and the UKF. The findings from each chapter are then summarized in Chapter 6, which also provides future research suggestions. These include opportunities for improving the UKF and potential experimental investigations where the UKF could provide important insight.

1.1 Original Contributions

A brief summary of the original research contributions of this dissertation are outlined below.

- Development and validation of a Bayesian estimator for filtering out transient biasing effects from FTIR measurements. These biasing effects emerge due to sample recirculation and signal non-stationarity of the incident IR beam. This tool improves estimated engine exhaust composition from FTIR measurements during transient operation.
- Identification of period-dependent artifacts in FTIR measurements of chemically evolving samples. These artifacts occur due to non-stationarity of the incident IR beam, which results in the measured/calculated IR spectrum being unevenly weighted by spectral intensities during low levels of optical path difference. The magnitude of these artifacts alternate for every other measurement, and depend on whether the moving mirror within the interferometer is scanning in the forward direction (increasing optical path difference) or backward direction (decreasing optical path difference).
- Mathematical proof that the Fourier transform of an interferogram from a non-stationary IR beam is unevenly weighted by spectral intensities that occur at low levels of optical path difference, and that the degree of weighting scales with spectral broadening. Thus, centerburst weighting magnitude varies from species to species, with greater centerburst weighting occurring for measurements of broadly absorbing species. These mathematical formulations are corroborated by experimental observations.
- Experimental evidence that volatile organic compound emissions from a spark-ignited, gasoline engine are substantially influenced by transient and historical operation, with the degree of influence depending on the particular species and whether it’s a fuel component or combustion intermediate.

CHAPTER 2 BACKGROUND AND MOTIVATION

2.1 Volatile Organic Compound Emissions

VOCs are a group of carbon-based, gaseous compounds that participate in atmospheric photochemical reactions [1]. VOC emissions substantially influence the radiative properties and quality of the atmosphere, most notably by reacting with nitrous oxides (NO_x) to produce tropospheric ozone, a potent greenhouse gas and fundamental component of smog [2]. Atmospheric lifetimes of other greenhouse gases are also increased in the presence of VOCs, due to competition for oxidants [3]. Furthermore, VOCs form secondary aerosols which scatter sunlight and promote cloud formation [4], [5]. The extent to which particular VOCs influence the atmosphere depend on many factors such as atmospheric lifetime, reactivity, and reaction mechanisms [6], [7]. For example, numerous studies have found that aromatics and alkenes possess high ozone creation potential relative to other VOC groups [8]–[10]. Certain VOCs are also highly toxic [11]. For instance, exposure to benzene and 1-3 butadiene is linked with elevated cancer risk [12]–[15]. Thus, species distribution should be considered when addressing the impact of anthropogenic VOC emissions.

According to the National Emissions Inventory, vehicles were responsible for over 23% of anthropogenic VOCs emitted in the U.S. in 2014, with the other major contributors being industrial processes and fires [16]. Even greater contributions from vehicles are typical in urban areas [17]–[21], where elevated levels of smog and poor air quality are common [22]. For example, approximately 71 and 80% of VOC emissions were attributed to mobile sources in an air quality study of two regions in Los Angeles [18]. Vehicle and marine vessel-related sources contribute 40-54% of the VOC emissions in Hong Kong in an air quality study that transpired in 2006-2007 [19]. Furthermore, exhaust and evaporative emissions from gasoline vehicles were found to comprise 52% of the VOC emissions in Beijing from ambient composition measurements conducted in August 2005 [20]. Thus, vehicles have become a primary target for reducing VOC emissions, as evidenced by the increasingly stringent regulations being placed on VOC emissions in the U.S. The maximum allowable fleet average non-methane organic compound (NMOG)+NO_x emissions for a light-duty vehicle manufacturer will decrease from 79 to 30 mg/mile from 2018 to 2025 under the Tier 3 regulations of the U.S. EPA in the absence of policy change [23]. Similar reductions are in place for heavy-duty vehicles. In 2012, the California Air Resources Board (CARB) implemented the LEV III emissions regulations, which tighten existing hydrocarbon emissions limits from vehicles. Under LEV III standards, all new passenger cars (including light-duty trucks and medium-duty passenger vehicles) with model years between 2015 and 2019 must emit fewer than 160 mg/mile of (NMOG)+NO_x and 4 mg/mi of formaldehyde [24]. Even stricter reductions are imposed for vehicles within the ULEV and SULEV ((Super) Ultra-Low Emissions Vehicle) categories. Achievement of these VOC emissions reductions requires further progress in engine efficiency and control strategies. Such progress necessitates elucidation of the relationships between engine conditions and the quantity and distribution of VOC emissions.

Numerous studies have explored the relationships between VOC emissions and engine speed/load. Wang et al. measured the comprehensive composition of exhaust gas collected from three light-duty gasoline vehicles operating under the ECE and EUDC test cycles using gas chromatography-mass spectrometry (GC-MS) [25]. It was found that the VOC emissions under the ECE, an urban, low speed driving cycle are 16 times greater than the VOC emissions of the EUDC, a faster, suburban driving cycle. In addition, aromatics and alkanes are the most emitted groups during ECE and EUDC tests, comprising 38 and 37% of the distribution, respectively. Higher levels of the carcinogens toluene and benzene were also detected in the EUDC tests. Nakashima et al. measured concentrations of 54 different VOCs from exhaust from three gasoline vehicles operating under nine different driving cycles using gas chromatography-flame ionization detection [26]. The distributions of alkanes, alkenes, aromatics and aldehydes vary according to driving cycle. For “cold” driving cycles, the alkanes and alkenes are present in roughly equal quantities in exhaust samples, while alkanes are dominant in “hot” cycles. In a review of VOC emission studies in China, Wang et al. compares VOC distributions of emissions for vehicles operating at idle and a steady speed of 20 km/hr [27]. It was found that alkanes (66%) and alkenes (50%) are dominant during idle and steady operation, respectively. Ethylene and propene, among a few other VOCs are present in high quantities in the idle tests, while VOC distribution is more uniform during steady operation.

The studies presented above illustrate that species distribution is a strong function of engine operating conditions. This suggests that speed/load points can be strategically selected within engine control algorithms to achieve emissions with desired VOC distributions. However, the development of such an algorithm requires a direct input-output relationship between engine speed/load and emissions. The emissions data from the studies presented above are from batch measurements, which provide total emissions over an operational regime but provide no information on emissions at specific speed/load points. Furthermore, previous research has shown that instantaneous and integrated engine emissions are a function of the speed-load history of an engine for real-world driving conditions [28]–[30], which are largely transient [31]. Thus, a thorough understanding of transient effects on VOC emissions is required to formulate a model that maps emissions to engine operational conditions. While the literature currently lacks direct illustrations of transient effects on comprehensive VOC emissions, an abundance of time-resolved, transient emissions data of major species, particulates and a few selective VOCs exist. A review of these studies is provided below.

2.2 Transient Engine Emissions

Numerous research efforts have explored the differences between engine emissions during steady and transient operation in a given speed/load regime. Some studies have gone a step further and attempted to model transient effects to ultimately predict emissions during a given driving cycle. However, few of these studies have investigated transient effects on VOC emissions distribution, despite ample evidence of these effects on individual VOCs, major species and particulates. Thus, to illustrate the future opportunities for uncovering, predicting and controlling transient effects on VOC distribution, a general review of transient engine emissions is provided. This includes an overview of experimental examinations of transient emissions, as well as existing modelling techniques that could be applied to predict transient VOC emissions given sufficient time-resolved measurement data.

Gullet et al. measured benzene and carbon monoxide (CO) emissions for cold starts of a medium duty diesel engine operating at power output of 45 kW [32]. The maximum benzene and CO emissions measured during startup are 20 and 3 times greater than the emissions during steady-state, respectively. These elevated emissions during the cold start are indicative of incomplete combustion during the warm-up process, which is mostly attributed to reduced temperatures and greater fuel injection mass within the engine. A cold start is an extreme example of a speed/load change. Numerous examples of the influence of gradual or minor speed/load changes on emissions also exist in the literature. Hagena et al. studied NO_x and particulate emissions from a diesel engine for tip-ins from 1 to 9 bar at varying ramp rates [33]. Particulate emissions during an instantaneous load change reaches values 10 times greater that of a tip-in spanning 5 seconds. Furthermore, predictions from a quasi-steady engine map underpredict the peak particulate and NO_x emissions by about an order of magnitude and 33%, respectively. In another work, positive and negative speed and load ramps were applied to two turbocharged non-road diesel engines [34]. Unburned hydrocarbons (HC), CO and NO_x emissions during the ramps differ significantly (by factors of 2 or 3 in some cases) from the steady-state emissions for a given speed/load point, with the magnitude of these differences scaling with ramp rate. For most of the cases, emissions increase for both positive and negative ramps. Increased emissions during ramps is partially attributed to a time-lag in the turbocharger, which supplies additional air to the engine during load increases. This time-lag leads to non-ideal equivalence ratios within the engine, and is a reoccurring problem in turbocharged diesel engines [35], [36].

Speed/load history has also been demonstrated to alter gasoline engine emissions. In one study, benzene emissions were measured for a variety of gasoline-driven EURO-2 vehicles driven on the European UDC and U.S. FTP cycles using chemical ionization mass spectrometry [37]. To quantify the effects of velocity/acceleration, the data were sorted into different velocity classes. Emissions within identical velocity classes differ substantially for varying levels of acceleration, illustrating the influence of speed/load history. Post-catalyst concentrations of benzene within the fastest velocity bin vary by more than 100% between different acceleration values. For slower speeds, benzene emissions fluctuate between negligible and substantial (>20 ppm) concentrations at negative and positive accelerations, respectively. In work by Heeb et al., emissions of NO, nitrogen dioxide (NO_2) and ammonia (NH_3) from gasoline-fueled Euro-3 and Euro-4 passenger cars were measured using chemical ionization-mass spectrometry for 7 different driving cycles [38]. It was found that acceleration, deceleration and gear shifts result in elevated emissions factors for NO and NH_3. Maricq et al. studied transient effects on mass and size distributions of particulate emissions from 21 gasoline vehicles under the FTP driving cycle [39]. Peaks in particulate emissions from this study correspond to periods of acceleration.

While time-resolved measurements of speciated emissions during transient operation are limited due to the difficulties associated with such measurements [40], there are a handful of techniques capable of transient speciation. The following is a brief review of studies where transient speciation of engine exhaust is conducted. In a study by CARB, a group of 20 light duty gasoline vehicles with classifications ranging from Tier 0 to partial-zero emissions (PZEV) are tested on the Unified Cycle (UC) [40]. Transient speciation measurements are executed at intervals of 6 seconds using proton-transfer-reaction mass spectrometry, which show that an overwhelming majority of total benzene, acetaldehyde and aliphatic compounds emissions during a driving cycle are emitted during the cold start. Gierczak et al. also explored cold start emissions of various VOCs using Fourier transform infrared spectroscopy [41]. They found elevated levels of ethanol, acetaldehyde, formaldehyde, and non-methane hydrocarbons during the first 100 seconds of the FTP driving cycle. In another study, compositions of benzene, toluene and C_2-benzene from emissions of various vehicles within the Swiss car fleet were measured during a driving cycle using chemical ionization-mass spectrometry [42]. Mixing ratios between these three species vary considerable throughout a driving cycle due to velocity and acceleration effects. Lastly, emissions of 27 gas-phase species from a 1999 Toyota Sienna minivan were measured using a portable Fourier transform infrared spectrometer [43]. Emissions of each species behave differently throughout the driving cycle, although spikes in toluene and m-xylene emissions occur during the cold-start, and 1,3 butadiene and benzene emissions rise steadily throughout.

The studies outlined above clearly indicate that transient effects impact engine emissions. For future engine designs and control algorithms to be updated to reduce VOC emissions, these transient effects must be modelled. Below is a review of various transient emissions modelling techniques that could be applied to predict VOC distributions given sufficient time-resolved, transient VOC measurement data.

2.2.1 Emissions Modelling

Predictive modelling is a key element of engine design and operation optimization [44], [45]. Due to the vast number of operational points of an engine, it is extremely burdensome to experimentally optimize each operational parameter (i.e. fuel injection timing, injection mass, exhaust gas recirculation level and boost pressure for diesel engines, etc.) for a sufficient number of speed/load points. This task is even more formidable if transient effects are to be captured, since experiments at the same speed/load point must be repeated for numerous speed/load histories. Hence, models are often employed for this purpose. Predictive engine models vary appreciably in approach and complexity. One of the most common approaches is quasi-steady engine mapping, where engine performance is optimized for a limited number of steady-state speed/load points, and the optimal parameters for the remaining points are estimated using binning or interpolation [46]–[49]. While this method is simple and efficient, it fails to account for speed/load history and provides an overly-simplified and inaccurate portrayal of the relationship between operating parameters and performance.

For example, in work by Ericson et al., quasi-steady maps of fuel consumption, CO, HC, NO_x and particulate matter (PM) were developed for three Euro 3-class diesel engines using steady-state experiments [46]. These values are compared with fuel consumption and emissions from experiments for four different transient cycles. Discrepancies of 60-70% between the transient experimental values and those predicted from the quasi-steady model are common. Turbocharger lag is believed to contribute to these discrepancies, as the resulting fuel-richness within the engine during a load ramp yields incomplete combustion. To account for this effect, an empirical relationship between turbocharge delay and load rate was developed. However, while this method improves transient CO emissions predictions significantly, little to no improvement is seen for PM and HC in most cases. Other various modifications to the quasi-steady model exist in the literature [46], [50]–[52]. In a study by Bishop et al., emissions maps for three different diesel-powered vehicles were generated using experimental data from transient driving cycles [50]. Each measured species from an experiment was binned according to the current speed and load. The emissions value assigned to that speed/load bin is the average of all measured values whose speed/load lie within that bin. Cumulative CO, CO_2 and NO_x predictions from this approach are shown to agree with experiments over entire driving cycles. However, there are substantial errors in instantaneous emissions at most points. These results are likely explained by the cumulative fashion in which emissions are treated. While this method fails to account for the effects of specific speed/load trajectories, the resulting errors are cancelled out when integrated over entire driving cycles.

In another approach, emissions predictions from steady-state maps are modified with a physics-based engine temperature model with empirically determined constants [52]. It is theorized in this work that emissions deviate from steady-state predictions according to temperature development within the engine. A first order differential equation for the "warmth" of the engine is prescribed which accounts for heat addition and loss mechanisms. This warmth parameter is ultimately used to modify the emissions prediction, with the steady-state and transient predictions being equal for a fully-warmed engine. Predictions of HC, CO and NO_x were compared to measured emissions from a Mercedes diesel and Saab gasoline engine over a LA4 and US06 driving cycle. Improvements in instantaneous and integrated emissions predictions from this method are achieved in most cases. However, the method has notable difficulty predicting HC emissions, with the modified method yielding significantly worse predictions than the steady-state map in some cases, especially for instantaneous emissions.

Due to the limitations of quasi-steady modelling and its modifications, more rigorous methods for predicting transient emissions have been pursued in the literature. One such implementation is the artificial neural network (ANN) [53], which is a machine learning tool that optimizes the relationships between specific inputs and outputs by training a set of "artificial neurons" on existing input/output data [54]. In transient emissions modelling, current and historic engine operation parameters (such as speed, load, equivalence ratio, etc.) serve as the input data, while transient emissions measurements serve as the output. Numerous implementations of ANN for predicting engine performance exist in the literature [55]. For example, an ANN for predicting transient NO_x emissions from a Honda 2.2L i-DTEC diesel engine according to engine speed, injected fuel mass, air-to-fuel ratio, air mass flow, boost pressure and exhaust gas temperature was developed by Fischer [56]. The ANN was trained using a variety of transient driving cycles including the New European Driving cycle (NEDC) and the US06. Cumulative estimations of NO_x for the Artemis Urban test cycle are within 1.57% of the measured values. Instantaneous NO_x emissions agree well with measured values over certain regions of the driving cycle, although the discrepancy over the entire cycle wasn't quantified. In work by Domínguez-Sáez et al., an ANN was used to predict CO_2, NO_x and particulate number concentration for a 2.0 Euro 4 diesel engine fueled with diesel fuel and animal fat using vehicle speed and acceleration, engine speed and torque, air intake temperature, boost pressure, mass air flow and fuel consumption [57]. The ANN was trained and validated over 4 repetitions of the New European driving cycle and 5 steady state conditions. Correlation (R^2) values of 0.91, 0.78, 0.87 and 0.81 were achieved for CO_2, NO_x, particles concentration and geometric mean diameter between measured and predicted values.

2.2.1.1 VOC Emissions Models

Currently, few engine emissions models of VOC speciation, or even individual VOCs exist in the literature. Perhaps the most well-known model for predicting VOC emissions is the EPA Motor Vehicle Emissions Simulator (MOVES) [58]. However, MOVES primarily serves as a tool for estimating emission inventories at the national or regional level over a time span given vehicle population and travel data. This tool estimates emissions in a bulk manner and isn't appropriate for detailed prediction of engine performance with respect to operating conditions [59]. Steady state engine maps of VOCs such as methane, ethane and formaldehyde were composed from data from a zero-dimensional stochastic reactor model of a homogeneous charge compression ignition (HCCI) engine in a study by Maurya and Akhil [60]. The emissions were tabulated with respect to engine speed and indicated mean effective pressure (IMEP). In work by Wei et al., formaldehyde and methanol emissions were measured from a three-cylinder spark-ignited engine operating at various speeds/loads at steady-state [61]. At each speed/load, tests were conducted for a variety methanol-gasoline blends. This data was used to formulate steady-state maps of formaldehyde and methanol emissions for each fuel blend. It is important to note that the two studies listed developed steady-state models.

It is apparent that the literature lacks predictive models for VOC emissions during transient engine operation. However, the development of such models requires training/validation with transient, time-resolved VOC speciation data from experiments. Such data are also sparse within the literature, since there are few routine diagnostic techniques capable of continuously measuring VOC emissions during transient engine operation. In the following sub-section, a brief review of exhaust gas speciation techniques and their limitations is provided. This is followed by an introduction to Fourier Transform Infrared (FTIR) spectroscopy, which measures VOC emissions in real-time and possesses the measurement frequencies necessary for time-resolved speciation, but is biased during transient measurements. These transient biasing effects are discussed, which ultimately motivate the implementation of a Bayesian estimation model for filtering out these effects from FTIR measurements of engine exhaust.

2.3 VOC Emissions Diagnostics

A variety of techniques are available for comprehensive speciation of VOC engine emissions during transient driving cycles. However, most conventional methods measure composition from batch samples from entire driving cycles. Thus, these techniques are limited to quantifying total emissions during lengthy driving cycles, and therefore provide scant information on transient effects. One of the most prevalent batch techniques is gas chromatography-mass spectrometry (GC-MS) [62]. This technique involves continuously drawing exhaust sample into a bag via a constant volume sampler, diluting the mixture, and eluting the contents through the capillary tubes of a GC. The GC separates each component of the sample according to its characteristic elution time, which is a function of its tendency to remain in the stationary phase of the capillary tubes. Each component exits the GC and enters the MS, where the sample is ionized. The mass-to-charge ratio of the ionized molecules – which indicate their chemical structure – is then determined by simultaneously accelerating the sample and exposing it to a magnetic field. A detector with multiple channels senses the deflected ions and their relative abundance, with the particular channel indicating the deflection of the ion, and therefore mass-to-charge ratio [63]. While very accurate and sensitive due to the concurrent use of two separation techniques, the elution process is slow and there performed offline, preventing transient measurements. A similar technique that is often employed is GC-Flame Ionization Detection (FID) [64], [65]. In this method, a FID is placed downstream of the GC, which measures the masses of each separated compound according the number of ions detected during oxidation of the sample with a hydrogen flame [66]. It should be noted that the FID itself is a fast-response technique, but requires a separation technique which may be slow (such as a GC), or only effective for certain compounds (such as a non-methane cutter) [67]. Instances of using high-performance liquid chromatography (LC)-MS by reacting sample VOCs with an acid solution and measuring the resulting stable products are also found in the literature [68].

Although less widespread than batch measurements, there are a few online techniques capable of time-resolved, transient speciation. One such method is to eliminate the GC in the GC-MS system and simply perform mass spectrometry. Such approaches usually employ chemical ionization by introducing the sample to a chemically-charged reagent gas [69], [70]. This method is less prone to fragmentation of the sample VOCs than electron ionization [71]. One disadvantage with chemical ionization-mass spectrometry (CI-MS) is that it detects components based on mass only, and therefore cannot differentiate isomers and isobaric compounds. Furthermore, the species that can be detected with CI-MS are limited to those with sufficient affinity for ionization. For example, a specific CI-MS method called proton-transfer-reaction mass spectrometry (PTR-MS) utilizes hydronium (H_3O^+) as the reagent, which induces a proton transfer to species with proton affinities greater than that of water . This prevents the detection of important alkanes (such as methane, ethane and pentane) and ethylene [72]. Different reagents can be selected to relax these proton affinity restrictions. However, using such reagents requires significant dilution of the sample to prevent depletion of the reagents from ionization of the substantial quantities of water/O_2 in the sample [73]. Also, typical measurement times of PTR-MS lie between 3 and 10 seconds [72], which may be inadequate to capture certain transients.

Another online technique used for transient speciation is tunable laser diode absorption spectroscopy (TDLAS). As the name suggests, this method uses a tunable diode laser to emit modulated light over a relatively narrow wavenumber range (1-2 cm^{-1}) by altering current injection density. The light travels through the optically accessible sample and onto a photodiode, where its incident intensity is measured [74]. Incident intensity is indicative of absorbance and therefore sample concentration. For engine exhaust applications, the sample is usually drawn through a White cell, which contains directly facing mirrors which increase the traversed distance of emitted light through the sample, thereby improving sensitivity [75]. While advantageous for transient and cycle-by-cycle analysis due to its exceptional measurement frequency (up to 10 GHz), each diode laser is capable of measuring only a single species due to its narrow frequency range. Thus, the number of species that can be measured is limited to the number of mirror pairs that can fit within a White cell [76]. A similar transient speciation technique that also utilizes the characteristic light absorbance features of specific compounds is Fourier transform infrared (FTIR) spectroscopy. FTIR spectroscopy and its applicability to transient speciation is a primary focus of this work. Thus, its operating principles, advantages and drawbacks are discussed in detail.

2.3.1 Fourier Transform Infrared Spectroscopy

FTIR spectroscopy utilizes broadband, infrared radiation to infer the light absorbance of a sample over a wide spectral range, permitting comprehensive speciation with a single measurement. A FTIR determines absorbance by traversing an IR beam composed of broad spectral components through a sample and measuring the incident intensity. The interference properties of light are utilized to modulate the IR beam in a predictable manner that allows its incident spectral components to be deduced from the resulting measurement via the Fourier transform. Figure 2-1 displays a general schematic of a FTIR. A typical FTIR consists of a Michelson interferometer (right) which produces the modulated IR beam, a White gas cell (left) that contains the sample, and a detector for measuring the downstream incident intensity of the modulated IR beam.

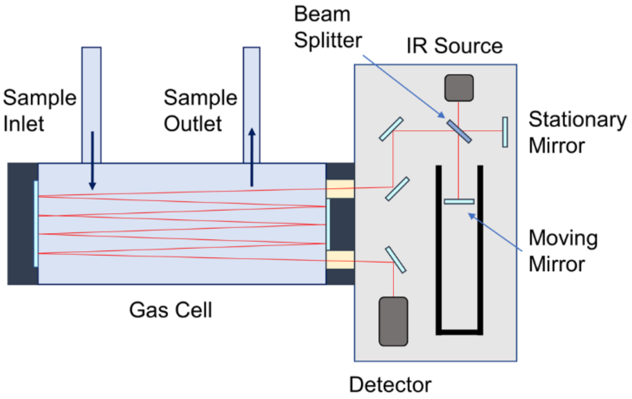

Figure 2-1: General Schematic of an FTIR spectrometer.

The detailed operating principles of FTIR spectroscopy are as follows. A source is heated to elevated temperatures (~1500 K) to induce the emittance of broadband, IR radiation at intensities near that of a blackbody. This IR radiation is focused and directed toward a beam-splitter, where half of the beam is reflected/transmitted toward a moving mirror, the other half toward a stationary mirror. The two beams reflect off their respective mirrors and coalesce at the beam splitter having travelled separate optical path distances. Due to constructive/destructive interference between photons of identical wavenumbers, the intensity of each spectral component within the IR beam modulates in a sinusoidal fashion as a function of optical path difference, with the wavenumber of these modulations equaling the wavenumber of the spectral component. The modulated spectral components of the IR beam also interfere with one another, yielding a total beam intensity that is also a function of optical path difference. The coalesced, modulated beam travels through the sample, contained within the gas cell, where its intensity is reduced due to absorption. After making multiple passes through the gas cell, the coalesced beam reaches a detector, where its intensity is measured. This process is repeated for numerous optical path differences, beginning with the initial moving mirror position called the centerburst – where all light constructively interferes, yielding a “burst” of intensity – and ending with the maximum mirror position. The measured intensity profile is Fourier transformed with respect to optical path difference to deduce the spectrum of incident intensity versus IR wavenumber. This spectrum is subtracted from a background spectrum obtained from a non-absorbing sample (usually N_2) to determine the intensity of IR absorbed at each wavenumber of interest. Since certain species absorb IR at specific wavenumbers and the level of IR absorption scales with mole fraction via Beer-Lambert’s law, this information can be used to quantitatively determine the chemical composition of the sample. A illustration of the composition quantification process is provided in Figure 2-2.

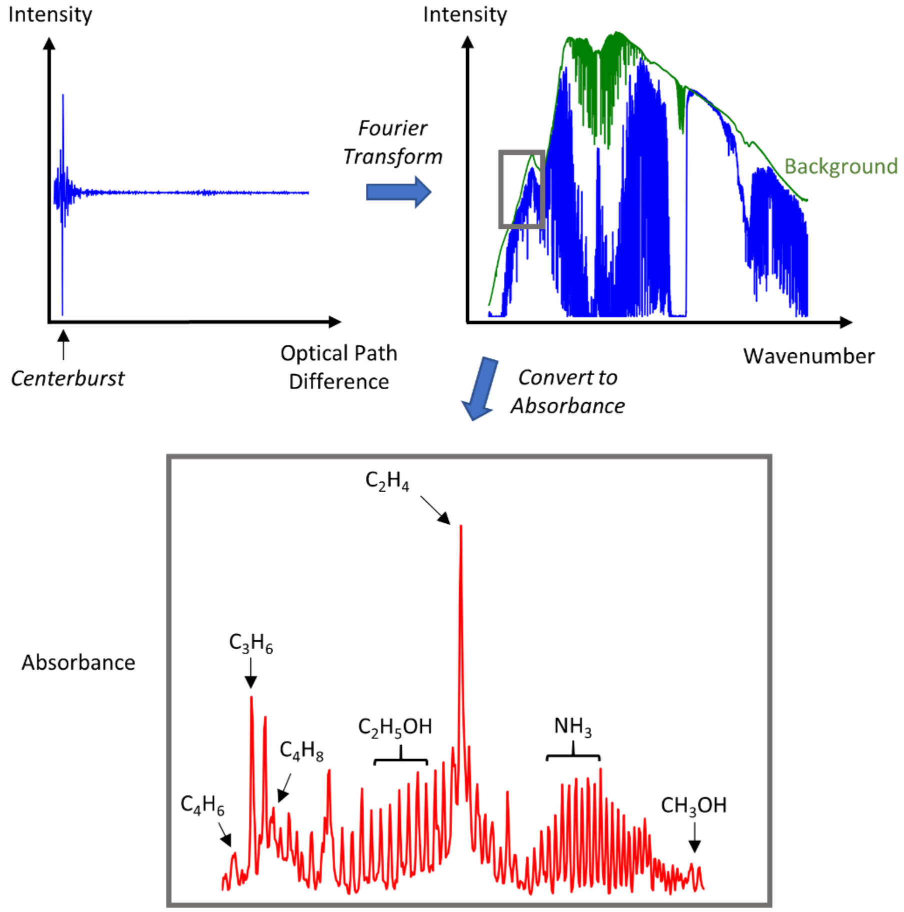

Figure 2-2: Illustration of the process for inferring composition from FTIR measurements. An interferogram (intensity with respect to optical path difference) is measured, which is Fourier transformed to yield the spectral components of the incident IR beam. The resulting spectral absorbance is calculated using the baseline spectrum, from which compositions are inferred according to the known absorbance features of specific chemical species.

2.3.2 FTIR Limitations for Transient Measurements

FTIR spectroscopy presents many advantages for engine exhaust characterization over other conventional techniques. First, FTIR measurements are performed online and in real-time, permitting transient analysis. Furthermore, typical FTIR measurements frequencies reach as high as 5 Hz, greatly exceeding the frequencies of CI-MS. Secondly, each measurable species has a distinguished spectrum, allowing a wide range of VOCs to be measured simultaneously, unlike TDLAS. Despite the advantages of FTIR spectroscopy, its suitability for studying engine transients is limited. A FTIR gas cell must have sufficient volume to allow multiple passes of the IR beam through the sample. Because of its large volume, residence times within a gas cell can be significantly greater than the measurement period of a FTIR, with a time constant of approximately 500 ms for a flowrate of 10 slpm. Consequently, FTIR data are obscured by historical emissions, preventing time-resolved analysis. An illustration of how engine exhaust composition and an FTIR measurement at a given time can differ is shown in Figure 2-3. This issue isn't necessarily mitigated by simply increasing the sample flow rate through the gas cell to decrease residence times, as this can cause turbulence-induced scintillation which increases noise in the measured IR intensity [77], as well as reduce pressures within the gas cell, rendering absorbance calibrations invalid. FTIR flow rates for engine exhaust characterization in the literature vary, but are typically between 1 and 12 liters per minutes (lpm) [41], [78]–[85]. Another issue with transient FTIR measurements is that the spectral intensity calculated by the Fourier transform is unevenly weighted by spectral intensities at/near the centerburst optical path difference. This bias is referred to herein as non-stationarity bias, since it's caused by the intensity of certain spectral components being non-stationary due to evolving levels of absorbance during a scan. This issue, which was unknown at the onset of this work, is discussed in detail and addressed in Chapter 4.

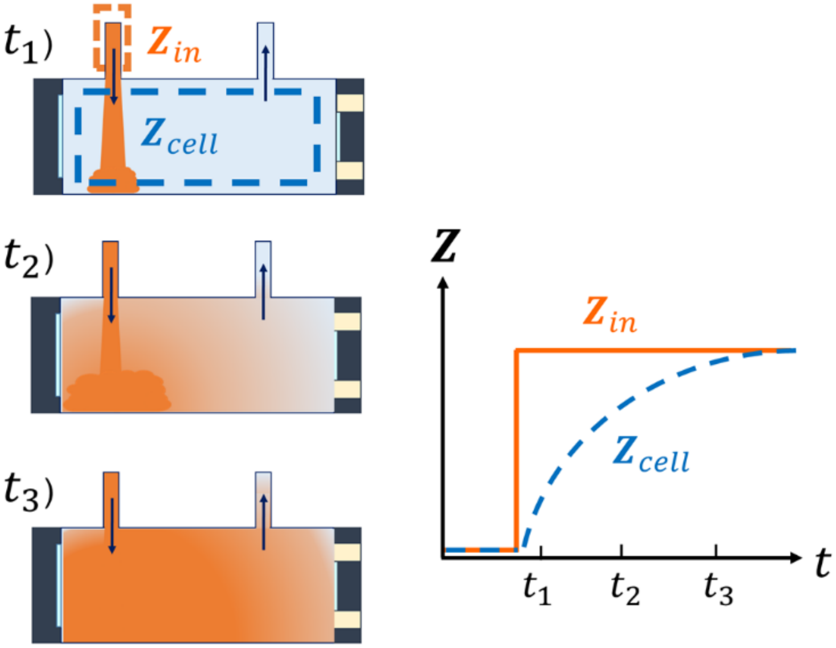

Figure 2-3: Illustration of how average composition within an FTIR gas cell evolves due to a step change in inlet composition. As shown, FTIR measurements can differ considerably from the composition of engine exhaust entering the FTIR gas cell at a given time.

One way to address sample recirculation effects on transient FTIR measurements is by estimating the instantaneous composition of exhaust entering the FTIR gas cell [86]. This requires a known/assumed relationship between gas cell inlet composition and total gas cell composition. In previous research, the FTIR gas cell was modelled as a well-mixed system [81], [87]. The equation for the well-mixed model is given in 2-1.

$$\boldsymbol{Z}_{cell}(t) = \boldsymbol{Z}_{in}(t-1)\left(1 - e^{-\frac{\Delta t}{\tau}}\right) + \boldsymbol{Z}_{cell}(t-1)e^{-\frac{\Delta t}{\tau}} \tag{2-1}$$

In the equation above, total gas cell mass composition and inlet gas cell mass composition are represented by $\boldsymbol{Z}_{cell}$ and $\boldsymbol{Z}_{in}$, respectively. These values can be vectors containing many species or a scalar for a single species. Current and previous measurement times are represented by t and $t-1$, respectively. The characteristic time scale (mass of sample inside the gas cell divided by mass flow rate) is given by τ. In work by Truex et al., the composition of exhaust entering the gas cell during a measurement period ($\boldsymbol{Z}_{in}(t-1)$) is back-calculated according to Equation 2-1 and the current and previous FTIR measurement ($\boldsymbol{Z}_{cell}(t)$ and $\boldsymbol{Z}(t-1)$) [81]. While this method improves the overall trend in estimated instantaneous engine exhaust compared to raw measurements, noise from the FTIR measurements greatly exacerbates the noise of the estimated inlet composition, yielding considerable errors in instantaneous emissions estimates. However, this issue can be mitigated by filtering the FTIR data with a Bayesian estimation model (BEM). BEMs calculate the most statistically probable values for system states (i.e. composition of sample entering a FTIR gas cell) using a system model and known/assumed measurement noise statistics [88]. This estimation technique uses *a-priori* knowledge of the underlying system dynamics to correct for errors in state estimations caused by measurement noise. Since a FTIR gas cell can be modelled as a well-mixed system, and the degree of non-stationarity bias can be reasonably approximated (as discussed in Chapter 4), the problem of estimating the composition of sample entering a FTIR gas cell is well-suited for Bayesian estimation. The work presented herein aims to develop and validate this BEM for obtaining time-resolved engine exhaust measurements. A BEM which addresses sample recirculation effects is developed and computational validated in Chapter 3. In Chapter 4, a mathematical derivation of non-stationarity bias for each measurable species is developed, which is incorporated into a modified version of the BEM. This modified BEM is then experimentally validated. Results from the application of the BEM to FTIR measurements of exhaust from a gasoline engine during transient load ramps are presented in Chapter 5.

CHAPTER 3 BAYESIAN ESTIMATOR OF COMPREHENSIVE ENGINE EMISSIONS

FTIR spectroscopy is an attractive diagnostic for time-resolved, comprehensive engine exhaust speciation due to its ability to measure concentration of individual VOCs from continuously replenished exhaust samples at high frequencies. However, sample recirculation and evolving absorbance complicate the interpretation of FTIR measurements during transient engine operation. This chapter is dedicated to the development and computational validation of a Bayesian estimation model (BEM), which extracts instantaneous exhaust composition from biased FTIR measurements of chemically evolving exhaust samples. The BEM utilizes a simple sample residence time sub-model and measurement noise statistics to estimate the composition of sample entering a FTIR gas cell during a measurement period. Only sample recirculation is addressed in the development of the BEM in this chapter, as this topic is extensive by itself. Furthermore, most of the analysis in this chapter, including the computational validation of the sample residence time sub-model and quantification of performance limits of the BEM can be performed while neglecting the effects of evolving absorbance. The introduction of a modified measurement sub-model which accounts for these effects is reserved for Chapter 4, since its derivation is rigorous and constitutes a sizable fraction of the next chapter, and its implementation is necessary for the experimental validation portion of this work.

This chapter begins with a brief discussion of the fundamentals of Bayesian estimation in Section 3.1. From this discussion, the Unscented Kalman filter (UKF), which is the Bayesian estimator employed for this work, is introduced. The underlying approach of the UKF for optimal estimation is established, followed by the overview of its equations and estimation process. Section 3.2 presents the development of specific UKF sub-models that pertain to estimating instantaneous exhaust composition from FTIR measurements. This includes the state transition and measurement models (3.2.1) and process noise covariance model (3.2.2). In Sections 3.3 and 3.4, computational methods for validating the UKF are presented.

Computational fluid dynamics (CFD) and mixing network (MN) models for simulating the flow of sample with transient composition through a FTIR gas cell are presented. CFD simulations are used to validate the well-mixed assumption utilized in the state transition model (3.4.1), as well as generate synthetic FTIR measurements from which the lower limits of composition fluctuation duration that can be captured by the UKF are quantified (3.4.2). Synthetic FTIR measurements of engine exhaust from driving cycles are generated from MN simulations. These measurements are processed by the UKF and it is demonstrated that the UKF significantly improves instantaneous exhaust composition estimations compared to raw FTIR measurements (3.4.3). The relationships between UKF performance and inlet composition process noise are also explored.

3.1 Bayesian Estimation

A Bayesian filter is a recursive algorithm that estimates the most probable states of a system at a given time based on predictions from a physical model of the underlying dynamics of the system and measurements. Fundamentally, a Bayesian filter appropriately weighs model predictions and measurements, each with their inherent uncertainty distribution, to compose a statistically optimized estimation of the state with a smaller uncertainty distribution than the model predictions and measurements alone. This is illustrated in Figure 3-1. Bayesian filters are effective signal processing tools that increase confidence in state estimations from noisy measurements.

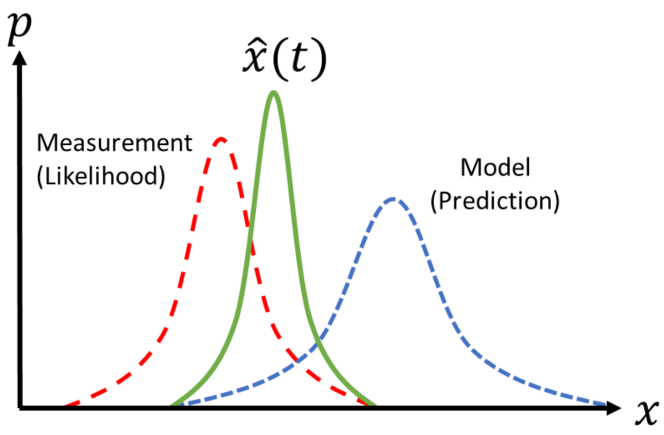

Figure 3-1: Illustration of the current state distribution calculated from a state model and measurement distribution using a Bayesian filter.

Bayesian filters ultimately emanate from Bayes theorem, which expresses the conditional probability of a set of states $\boldsymbol{X}_t \coloneqq \{\boldsymbol{x}(0), \ldots, \boldsymbol{x}(t)\}$ given a set of observations $\boldsymbol{Y}_t \coloneqq \{\boldsymbol{y}(0), \ldots, \boldsymbol{y}(t)\}$ as the conditional probability of the observations given the states, and the unconditional probabilities of the states and observations.

$$\Pr(\boldsymbol{X}_t|\boldsymbol{Y}_t) = \frac{\Pr(\boldsymbol{Y}_t|\boldsymbol{X}_t)\Pr(\boldsymbol{X}_t)}{\Pr(\boldsymbol{Y}_t)} \tag{3-1}$$

The use of Bayes theorem in measurement processing is motivated by the difficulty of calculating the conditional state distribution directly. Conversely, each of the distributions on the right-hand side of Equation 3-1 are estimated with relative ease. For typical measurement processing applications, the current state $\boldsymbol{x}(t)$ is of primary interest. Furthermore, it is advantageous if the conditional probability of the current state can be expressed using values at the current/immediately previous time step only, as this enables the algorithm to be recursive. This is accomplished by invoking the first order Markov assumption, which states that the current state conditional distribution is independent of states prior to the immediately previous state. The current observation conditional distribution is also assumed to depend only on the current state. Both assumptions are reasonable for most applications.

$$\Pr(\boldsymbol{x}(t)|\boldsymbol{X}_{t-1}) \rightarrow \Pr\big(\boldsymbol{x}(t)\big|\boldsymbol{x}(t-1)\big)$$

$\Pr(\boldsymbol{y}(t)|\boldsymbol{X}_t, \boldsymbol{Y}_{t-1}) \rightarrow \Pr\big(\boldsymbol{y}(t)\big|\boldsymbol{x}(t)\big)$

It can be shown that the application of the above assumptions results in the following form of Bayes theorem, which is the basis of recursive Bayesian algorithms.

$$\overbrace{\Pr(\boldsymbol{x}(t)|\boldsymbol{Y}_t)}^{\text{Posterior}} = \frac{\overbrace{\Pr(\boldsymbol{y}(t)|\boldsymbol{x}(t))}^{\text{Likelihood}}\ \overbrace{\Pr(\boldsymbol{x}(t)|\boldsymbol{Y}_{t-1})}^{\text{Prediction}}}{\underbrace{\Pr(\boldsymbol{y}(t)|\boldsymbol{Y}_{t-1})}_{\text{Evidence}}} \tag{3-2}$$

Equation 3-2 divides Bayes theorem into three key components:

Prediction: Predicted conditional distribution of the current state given previous measurements.

Likelihood: Conditional probability of the current observation given a current state.

Evidence: Normalizing factor for the prediction and likelihood.

Although the prediction and evidence probabilities are conditioned on the complete set of previous measurements, it can be shown that both distributions are functions of distributions from the current/immediately previous time steps due to the Markov and measurement assumptions. In fact, the evidence is the product of the prediction and likelihood integrated over all possible values of $\boldsymbol{x}(t)$, and thus serves as a normalization value in Equation 3-2. Thus, Equation 3-2 is recursive.

A Bayesian filter seeks the current state $\boldsymbol{x}(t)$ that maximizes the posterior. This is accomplished by estimating the distributions of the prediction, likelihood and evidence and applying Equation 3-2. While each Bayesian filter approximates these distributions differently, most filters fall within two categories: particle filters and Kalman filters. Particle filters represents each distribution with a set of discrete particles with distinct values. Prior particles are transformed by the state transition and measurement models to approximate the prediction and likelihood distributions, respectively. The evidence is also calculated from the transformed particles, and Bayes theorem is applied to yield a discrete estimate the posterior distribution. While particle filters are robust for a wide variety of systems, including those with exotic distributions and non-linear transformations, they require a substantial number of particles and are therefore computationally expensive.

When the distributions are Gaussian and transformations are linear, the mean and variances of prediction, likelihood and evidence are known precisely. These distributions form the basis from which the Kalman filter is developed. The distributions are given in Equations 3-3 through 3-5.

$$\Pr\big(\boldsymbol{y}(t)\big|\boldsymbol{x}(t)\big) \sim N\big(c[\boldsymbol{x}(t)], \boldsymbol{R}_{\boldsymbol{vv}}(t)\big) \tag{3-3}$$

$$\Pr(\boldsymbol{x}(t)|\boldsymbol{Y}_{t-1}) \sim N\big(\widehat{\boldsymbol{x}}(t|t-1), \widetilde{\boldsymbol{P}}(t|t-1)\big) \tag{3-4}$$

$$\Pr(\boldsymbol{y}(t)|\boldsymbol{Y}_{t-1}) \sim N\left(\widehat{\boldsymbol{y}}(t|t-1), \boldsymbol{R}_{\xi\xi}(t)\right) \tag{3-5}$$

c → measurement model (relates states to corresponding observations)

$\boldsymbol{R}_{\boldsymbol{vv}}$ → measurement noise covariance

$\widetilde{\boldsymbol{P}}$ → state error covariance

$\boldsymbol{R}_{\xi\xi}$ → innovation covariance (covariance of error between the predicted and true measurement)

The predicted states $\widehat{\boldsymbol{x}}(t|t-1)$ are calculated from the state transition model, which transforms the prior expected states according to the underlying dynamics of the system, while the predicted measurements $\widehat{\boldsymbol{y}}(t|t-1)$ are calculated by operating on the predicted state with the measurement model, which relates measurements to corresponding state values. State error and innovation covariances are calculated by propagating the prior state error covariance through the state transition/measurement models as well, with added terms to account for deviations from the state transition model and measurement noise. The Kalman filter is derived by plugging the distributions in Equations 3-3 through 3-5 into Bayes theorem, and then taking the derivative with respect to $\boldsymbol{x}(t)$ to find the current state that maximizes the posterior. Relative to particle filters, Kalman filters are simple and efficient, and therefore have a far-reaching influence in signal processing. They are implemented in a wide range of applications, including global positioning systems [89], real-time computer vision and image processing [90], prediction of electricity demand [91] and fault detection in gas turbines and other machinery [92].

Despite the ubiquity of the Kalman filter, its application is limited to systems with linear state transition and measurement models. When the transformations are non-linear, the distributions in Equations 3-3 through 3-5 can no longer be calculated directly and must be approximated. Two primary extensions of the Kalman filter that apply to non-linear systems exist. These are the Extended Kalman filter (EKF) and the Unscented Kalman filter (UKF). The Extended Kalman filter approximates the distribution of non-linear transformations in the state/measurement models using first order linearization. While the conversion of the standard Kalman filter to the EKF is straightforward, it is highly susceptible to discretization errors. Thus, the EKF tends to perform poorly for transformations governed by highly non-linear functions, such as exponential functions, which deviate substantially from linear approximations. However, EKFs remain relevant in signal processing due to their simplicity. The UKF, on the other hand, is a more robust algorithm which achieves up to third order accuracy. It uses a small set of deterministic sampling points to capture the first and second moments of the distributions given in Equations 3-3 through 3-5. These sampling points are transformed individually by the state transition and measurement models to develop the prediction and likelihood distributions, ultimately leading to the posterior distribution of a system.

The state transition model that governs the evolution of composition inside of a FTIR gas cell is non-linear with respect to flow rate. Since a non-linear Bayesian filter is required and high accuracy is desired for the estimation of transient emissions, the UKF is chosen as the filter for this work. The UKF is implemented to estimate the instantaneous composition of sample entering the FTIR gas cell during a measurement period, permitting transient emissions profiles to be accurately resolved. Therefore, the following section is devoted to describing the UKF in detail and providing its equations.

3.1.1 Unscented Kalman Filter

The UKF was developed based on the idea that approximating a Gaussian distribution is easier than approximating a non-linear transformation [93]. This statistical approximation is accomplished by deterministically sampling from a prior distribution. The sampling points, called sigma points, are selected to capture the true means and covariances of the prior. To estimate the statistics of a non-linear transformation of a prior state, each of the prior sigma points undergo the non-linear transformation. The collective transformation of each sigma point is called an Unscented transformation (UT). The resulting set of transformed sigma points provide an accurate approximation of the first and second moments of the transformed state, which are calculated by multiplying the value of each sigma point and its deviation from the mean by weights, respectively, and summing. UTs are more effective than linearization (the EKF) at preserving the statistics during a transformation, since the distribution itself is transformed rather than estimated from a linearized trajectory from the prior expected values, which may accumulate discretization errors. This benefit is demonstrated in Figure 3-2, where the sigma points and their associated resulting distribution are represented by the green circles and oval, respectively, and the distribution represented by a first order transformation is represented by the pink oval. The first and second moments of the transformed distribution from an UT are captured to the third and second order of accuracy for Gaussian and non-Gaussian prior distributions, respectively [94]. Thus, the UKF provides some relaxation in the requirement that the distributions in Equations 3-3 through 3-5 be Gaussian, as long as the distribution can be decently characterized by its first two moments. UTs are performed within the UKF to estimate the prediction and likelihood distributions, as will be shown in detail.

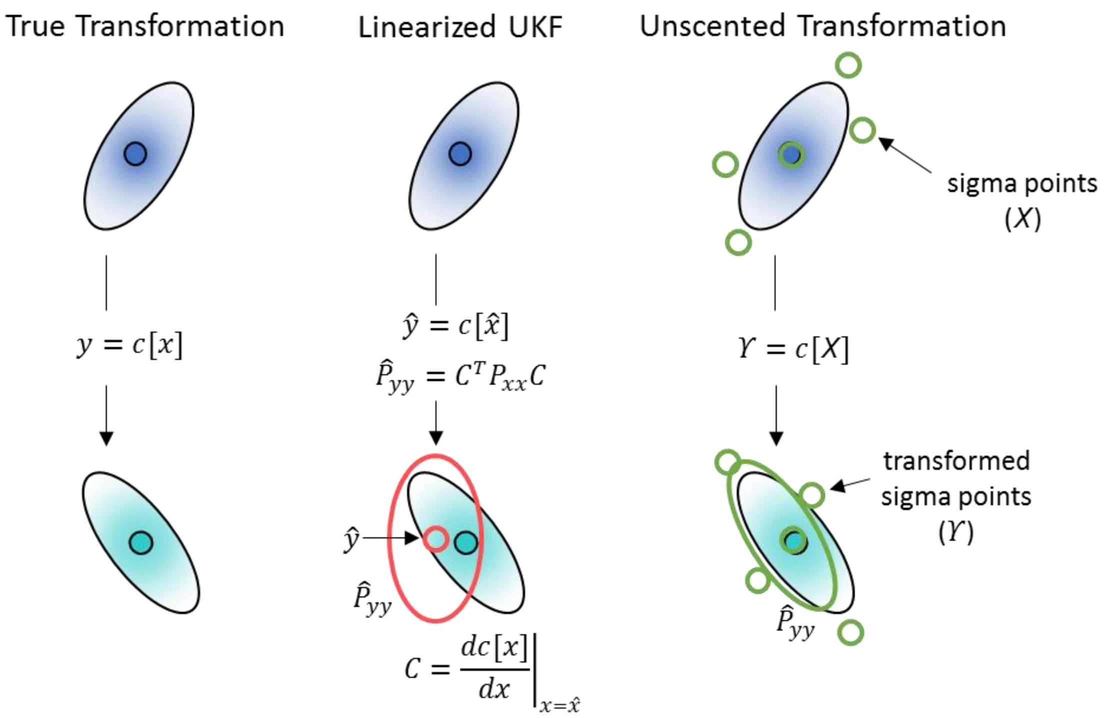

Figure 3-2: Illustration of Unscented transform and its comparison with the EKF. Overall idea borrowed from [94].

The UKF estimation process is divided into four main steps: prediction, measurement, gain and update. In the prediction step, the initial set of sigma points representing the prior state distribution undergo a UT by the state transition model to predict the current state value. The transformed state sigma points, along with the state propagation uncertainty (process noise) are used to estimate the state error distribution. A new set of state sigma points are generated to reflect the estimated distribution, which are then transformed by the measurement model. The measurement sigma points, along with the measurement noise covariance, are used to approximate the evidence distribution. The correlation between the state and measurement sigma points are then approximated, which is used as a gain to update the posterior mean and covariance, just as in the standard Kalman filter. Each step of the UKF will be now described in detail.

First, the prior sigma points ($\boldsymbol{X}$) are generated using the state ($\widehat{\boldsymbol{x}}$) and covariance ($\widetilde{\boldsymbol{P}}$) estimations from the previous time (t). If this is the first iteration of the filter, these state and covariance values are initial conditions. Otherwise, they are calculated from the posterior of the previous time step. For a Gaussian distribution, the minimum number of sigma points required to capture the first and second moments are $2N_x + 1$, where N_x is the dimensionality of the states.

$$\boldsymbol{X}_0 = \widehat{\boldsymbol{x}}(t-1|t-1) \tag{3-6}$$

$$\boldsymbol{X}_i = \widehat{\boldsymbol{x}}(t-1|t-1) + \left(\sqrt{(N_x+\kappa)\widetilde{\boldsymbol{P}}(t-1|t-1)}\right)_i \tag{3-7}$$

$$\boldsymbol{X}_{i+N_x} = \widehat{\boldsymbol{x}}(t-1|t-1) - \left(\sqrt{(N_x+\kappa)\widetilde{\boldsymbol{P}}(t-1|t-1)}\right)_i \tag{3-8}$$

Above, κ is a scalar tuning parameter, and $\left(\sqrt{(N_x+\kappa)\widetilde{\boldsymbol{P}}}\right)_i$ is the ith column/row of the Cholesky square root of the state error covariance matrix multiplied by $(N_x + \kappa)$. A κ value of $3 - N_x$ is chosen for this work, since it yields a kurtosis that is identical to that of a Gaussian distribution. Each sigma points is assigned a corresponding weight (W), which is derived so that the sum of the value of each weighted sigma point and its deviation from the mean match the first and second moments of a Gaussian distribution, as proven in [95].

$$W_0 = \frac{\kappa}{(N_x+\kappa)} \tag{3-9}$$

$$W_i = \frac{1}{2(N_x+\kappa)} \tag{3-10}$$

$$W_{i+N_x} = \frac{1}{2(N_x+\kappa)} \tag{3-11}$$

Each prior sigma point is propagated through the non-linear state transition model (a) to generate a new set of sigma points. These new sigma points are multiplied by their corresponding weights and then added together to give the initial state prediction at the current time step.

$$\boldsymbol{X}_i(t|t-1) = a[\boldsymbol{X}_i(t-1|t-1)] + b[\boldsymbol{u}(t-1)] \tag{3-12}$$

$$\widehat{\boldsymbol{x}}(t|t-1) = \sum_{i=0}^{2N_x} W_i \boldsymbol{X}_i(t|t-1) \tag{3-13}$$

The predicted state error covariance is then calculated according to the deviation of the sigma points from the mean and the uncertainty (noise) of the state transition model. The uncertainty of the state transition model is quantified in the process noise covariance matrix ($\boldsymbol{R}_{\boldsymbol{ww}}$). It should be noted that process noise refers to random error in the state propagation model, which is assumed to be Gaussian and white. This differs from systematic error, which produces a consistent offset between the estimated and true state value. The development of $\boldsymbol{R}_{\boldsymbol{ww}}$ as it pertains to this work is presented in section 3.2.2 Process Noise Covariance Matrix.

$$\widetilde{\boldsymbol{X}}_i(t|t-1) = \boldsymbol{X}_i(t|t-1) - \widehat{\boldsymbol{x}}(t|t-1) \tag{3-14}$$

$$\widetilde{\boldsymbol{P}}(t|t-1) = \sum_{i=0}^{2N_x} W_i \widetilde{\boldsymbol{X}}_i(t|t-1)\, \widetilde{\boldsymbol{X}}_i{}'(t|t-1) + \boldsymbol{R}_{\boldsymbol{ww}}(t-1) \tag{3-15}$$

The state sigma points are then updated to represent the predicted state error distribution at the current time.

$$\widehat{\boldsymbol{X}}_0 = \widehat{\boldsymbol{x}}(t|t-1) \tag{3-16}$$

$$\widehat{\boldsymbol{X}}_i = \widehat{\boldsymbol{x}}(t|t-1) + \left(\sqrt{(N_x+\kappa)\widetilde{\boldsymbol{P}}(t|t-1)}\right)_i \tag{3-17}$$

$$\widehat{\boldsymbol{X}}_{i+N_x} = \widehat{\boldsymbol{x}}(t|t-1) - \left(\sqrt{(N_x+\kappa)\widetilde{\boldsymbol{P}}(t|t-1)}\right)_i \tag{3-18}$$

The sigma points are propagated through the measurement model (c) to generate the measurement sigma points ($\boldsymbol{Y}$). Each measurement sigma point is multiplied by its corresponding weight and summed to yield the measurement prediction ($\widehat{\boldsymbol{y}}$), or the mean of the likelihood distribution.

$$\boldsymbol{Y}_i(t|t-1) = c\left[\widehat{\boldsymbol{X}}_i(t|t-1)\right] \tag{3-19}$$

$$\widehat{\boldsymbol{y}}(t|t-1) = \sum_{i=0}^{2N_x} W_i \boldsymbol{Y}_i(t|t-1) \tag{3-20}$$

The likelihood covariance ($\boldsymbol{R}_{\boldsymbol{\xi\xi}}$) is then calculated according to the residuals of the measurement sigma points ($\boldsymbol{\xi}$) and the measurement noise. $\boldsymbol{R}_{\boldsymbol{vv}}$ is the measurement noise covariance matrix. Like the process noise, measurement noise is assumed to be Gaussian and white.

$$\boldsymbol{\xi}_i(t|t-1) = \boldsymbol{Y}_i(t|t-1) - \widehat{\boldsymbol{y}}(t|t-1) \tag{3-21}$$

$$\boldsymbol{R}_{\boldsymbol{\xi\xi}}(t|t-1) = \sum_{i=0}^{2N_x} W_i \boldsymbol{\xi}_i(t|t-1)\,\boldsymbol{\xi}_i{}'(t|t-1) + \boldsymbol{R}_{\boldsymbol{vv}}(t) \tag{3-22}$$

The cross-covariance between the predicted state and measurement regressions is then calculated by multiplying the weighted state and measurement regression sigma points and summing. This value is then multiplied by the inverse of the measurement residual covariance to yield the gain.

$$\boldsymbol{R}_{\widetilde{\boldsymbol{X}}\boldsymbol{\xi}}(t|t-1) = \sum_{i=0}^{2N_x} W_i \widetilde{\boldsymbol{X}}_i(t|t-1)\,\boldsymbol{\xi}_i{}'(t|t-1) \tag{3-23}$$

$$\boldsymbol{K}(t) = \boldsymbol{R}_{\widetilde{\boldsymbol{X}}\boldsymbol{\xi}}(t|t-1)\boldsymbol{R}_{\boldsymbol{\xi\xi}}{}^{-1}(t|t-1) \tag{3-24}$$

The estimated measurement is then subtracted from the actual measurement $(\boldsymbol{y})$ at the current time to yield the innovation. This quantity is multiplied by the gain and added to the prior state estimation to yield the posterior estimation at the current time. The posterior state error covariance matrix is calculated as well. Due to the Bayesian estimation strategy of incorporating model and measurement statistics, the confidence in the resulting posterior estimation is greater than that of the model and measurements alone. In other words, the covariances within $\widetilde{\boldsymbol{P}}(t|t)$ are less than that of $\widetilde{\boldsymbol{P}}(t|t-1)$ and $\boldsymbol{R}_{\boldsymbol{\xi\xi}}(t|t-1)$, resulting in a statistically optimized estimation of $\hat{\boldsymbol{x}}(t|t)$.

$$\boldsymbol{e}(t) = \boldsymbol{y}(t) - \hat{\boldsymbol{y}}(t|t-1) \tag{3-25}$$

$$\hat{\boldsymbol{x}}(t|t) = \hat{\boldsymbol{x}}(t|t-1) + \boldsymbol{K}(t)\boldsymbol{e}(t) \tag{3-26}$$

$$\widetilde{\boldsymbol{P}}(t|t) = \widetilde{\boldsymbol{P}}(t|t-1) - \boldsymbol{K}(t)\boldsymbol{R}_{\boldsymbol{\xi\xi}}(t|t-1)\boldsymbol{K}'(t) \tag{3-27}$$

This completes a single iteration of the UKF. In the next iteration, the current state and state error covariance become the initial conditions and the next model prediction and measurement are filtered.

$\hat{\boldsymbol{x}}(t|t), \widetilde{\boldsymbol{P}}(t|t) \rightarrow \hat{\boldsymbol{x}}(t-1|t-1), \widetilde{\boldsymbol{P}}(t-1|t-1)$

An overview of an entire iteration of the UKF is illustrated in Figure 3-3. The sub-models within the UKF – the state transition model, measurement model and process noise covariance matrix – are introduced in the following sub-section.

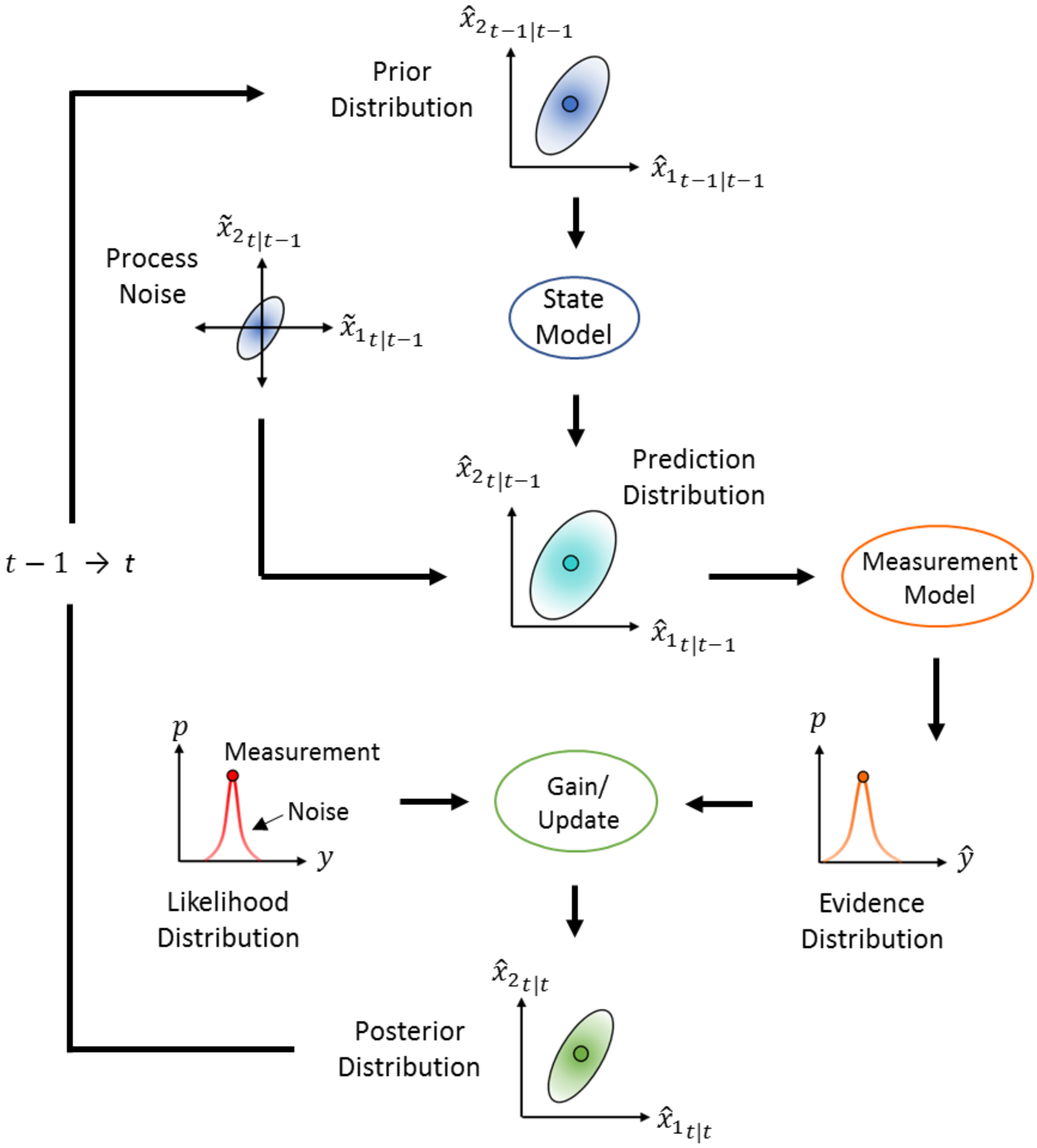

Figure 3-3: Example flowchart of the Unscented Kalman filter estimation process for a system with two states and one observation.

3.2 UKF Sub-Models for Exhaust Composition Estimation

In this section, the state transition model, measurement model and process noise covariance matrix within the UKF are formulated in detail. These components of the UKF are specific to an application, and are therefore unique for each filter. The sub-models in this work are designed to ultimately yield accurate, instantaneous estimations of the exhaust gas emitting from an engine and entering a FTIR gas cell. Thus, models and state variables are selected to connect FTIR measurements to gas cell inlet composition.

3.2.1 State Transition/Measurement Models

The state transition model propagates the state values through time according to the systems dynamics. It is a critical element of the UKF, as it provides the initial prediction for the current state values. The system is described by 3 states: composition entering the FTIR gas cell ($\boldsymbol{Z}_{in}$), total gas cell composition ($\boldsymbol{Z}_{cell}$), and mass flow rate ($\dot{m}$). It should be noted that the dimensionality of $\boldsymbol{Z}_{in}$ and $\boldsymbol{Z}_{cell}$ is equal to the number of species. Total gas cell composition is modelled using the well-mixed assumption. Mass flow through the gas cell is assumed to be quasi-steady. The initial predictions for inlet composition and mass flow rate are the values from the previous time step. These states are modelled this way because their values are influenced by factors outside of the system. Essentially, these states are updated within the filter according to the measurements and total gas cell composition model. The state-space equations are given below.

$$\hat{\boldsymbol{x}}(t|t-1) = \begin{bmatrix} \boldsymbol{Z}_{in}(t|t-1) \\ \boldsymbol{Z}_{cell}(t|t-1) \\ \dot{m}(t|t-1) \end{bmatrix} = a \begin{bmatrix} \boldsymbol{Z}_{in}(t-1|t-1) \\ \boldsymbol{Z}_{cell}(t-1|t-1) \\ \dot{m}(t-1|t-1) \end{bmatrix} =$$

$$\begin{bmatrix} \boldsymbol{Z}_{in}(t-1|t-1) \\ \boldsymbol{Z}_{in}(t-1|t-1)\left(1 - e^{-\frac{\Delta t}{\tau(t-1|t-1)}}\right) + \boldsymbol{Z}_{cell}(t-1|t-1)e^{-\frac{\Delta t}{\tau(t-1|t-1)}} \\ \dot{m}(t-1|t-1) \end{bmatrix} \tag{3-28}$$

Here, τ represents the effective time constant the gas cell, or the mass divided by mass flow rate. Mass within the gas cell is assumed to remain constant in this model. It should be noted that total gas cell mass could be included as a state variable, since FTIRs measure temperature and pressure within the gas cell, and total gas cell molecular weight could be deduced from Z. Mass could therefore be calculated via the ideal gas law. However, since FTIRs control temperature and pressure to remain constant, and the main combustion products are usually relatively consistent, mass within the gas cell should remain nearly steady.

The measurement model describes the relationship between system states and measurement output. Strictly speaking, a FTIR measures the incident intensity of the modulated IR beam relative to moving mirror position. Chemical composition is deduced from this measurement by Fourier transforming the measured intensity, calculating spectral absorbance, and applying an algorithm which estimates composition from absorbance calibrations. However, it may be impractical to include IR beam intensity within the UKF sub-models since it is measured at over 30,000 optical path difference points, and the noise statistics at each point would need to be known in addition to their propagation effects into the calculation of each species. Furthermore, this would require the reverse engineering of the FTIR composition algorithm, which is proprietary. Thus, the composition calculation from the FTIR algorithm itself is treated as a measurement. As will be shown later, reasonable estimates of the composition noise statistics resulting from measurement noise can be obtained by various methods. Since FTIRs are calibrated to yield mole fractions from spectral absorbance, the model for FTIR measurements is simply the element-wise conversion from total gas cell mass fraction to mole fraction. It should be noted that later in the dissertation, the FTIR measurement model will be updated to account for non-stationarity effects. The current version is introduced now for simplicity. Mass flow rate is also treated as a direct measurement. The equations for the measurement model are given below.

$$\hat{\boldsymbol{y}}(t|t-1) = \begin{bmatrix} \boldsymbol{Z}_{cell}(t|t-1) \cdot \frac{MW_{mix}}{\boldsymbol{MW}} \\ \dot{m}(t|t-1) \end{bmatrix} \tag{3-29}$$

$\boldsymbol{MW}$ and MW_{mix} represent the molecular weights of the species of interest and the molecular weight of the total gas cell sample, respectively.

3.2.2 Process Noise Covariance Matrix

In addition to measurement noise statistics, the statistics of unmodelled, stochastic fluctuations in the state values must be reasonably known for the UKF to perform optimally. These statistics are represented in the process noise covariance matrix $\boldsymbol{R_{ww}}$, which contributes to the total modeling uncertainty at the current time. Reasonable approximations for physical fluctuation statistics are imperative for determining the relative contributions of true state value fluctuations vs. measurement noise for outlying measurements that disagree with model predictions.

In the approximation of $\boldsymbol{R_{ww}}$, it is assumed in that fluctuations originally occur in the inlet composition and mass flow rate due to influences outside of the system (namely engine transients). These fluctuations are assumed to propagate throughout a measurement period to yield fluctuation in the total gas cell composition as well, via the well-mixed model. The covariance matrix of these original fluctuations (Φ) is provided in Equation 3-30.

$$\Phi = \begin{bmatrix} \Phi_{Z_{in}} & 0 & 0 \\ 0 & 0 & 0 \\ 0 & 0 & \Phi_{\dot{m}} \end{bmatrix} \tag{3-30}$$

Here $\Phi_{Z_{in}}$ and $\Phi_{\dot{m}}$ represent the stochastic noise variances for inlet composition and mass flow rate, respectively. Fluctuations of these two states are assumed to be uncorrelated, although some correlation likely exists since they are both caused by engine transients. However, correlations vary between species and with engine load ramp rate, and are therefore difficult to estimate. Furthermore, correlations between inlet composition and engine conditions are exactly what the implementation of the UKF is designed to uncover. Making poor initial assumptions about these relationships could yield undesired bias in the estimations.

The propagation of these original fluctuations into total gas cell composition and the resulting covariances are estimated using sigma point transformations conveniently similar to those of the UKF. This process is analogous to that of estimating the total model uncertainty in equations 3-6 through 3-15. First, a set of sigma points ($\boldsymbol{X}_{i,\boldsymbol{w}}$) are generated to represent the distribution of the states due to the original fluctuations in Φ.

$$\boldsymbol{X}_{0,\boldsymbol{w}} = \hat{\boldsymbol{x}}(t-1|t-1) \tag{3-31}$$

$$\boldsymbol{X}_{i,\boldsymbol{w}} = \hat{\boldsymbol{x}}(t-1|t-1) + \left(\sqrt{(N_x+\kappa)\Phi}\right)_i \tag{3-32}$$

$$\boldsymbol{X}_{i+N_x,\boldsymbol{w}} = \hat{\boldsymbol{x}}(t-1|t-1) - \left(\sqrt{(N_x+\kappa)\Phi}\right)_i \tag{3-33}$$

These fluctuation sigma points are then transformed by the state transition model (a) to yield a new set of sigma points that represent the distribution of fluctuations propagated throughout the measurement period.

$$\boldsymbol{X}_{i,\boldsymbol{w}}(t|t-1) = a\left[\boldsymbol{X}_{i,\boldsymbol{w}}(t-1|t-1)\right] \tag{3-34}$$

The variance of this distribution is then estimated by first subtracting each sigma point from the expected value of the sigma point population. The matrix product of these sigma point deviations are then multiplied by their corresponding weights and summed to yield the values within $\boldsymbol{R}_{\boldsymbol{ww}}$.

$$\widetilde{\boldsymbol{X}}_{i,\boldsymbol{w}}(t|t-1) = \boldsymbol{X}_{i,\boldsymbol{w}}(t|t-1) - \sum_{i=0}^{2N_x} W_i \boldsymbol{X}_{i,\boldsymbol{w}}(t|t-1) \tag{3-35}$$

$$\boldsymbol{R}_{\boldsymbol{ww}}(t-1) = \sum_{i=0}^{2N_x} W_i \widetilde{\boldsymbol{X}}_{i,\boldsymbol{w}}(t|t-1)\, \widetilde{\boldsymbol{X}}_{i,\boldsymbol{w}}{}'(t|t-1) \tag{3-36}$$

Estimated values for $\boldsymbol{R}_{\boldsymbol{ww}}$ are recalculated at each iteration to reflect the new initial state values.

Another way to estimate $\boldsymbol{R}_{\boldsymbol{ww}}$ is through propagating the original fluctuations throughout a measurement period via linearization. To provide the reader with an idea of the process noise covariances in terms of $\Phi_{Z_{in}}$ and $\Phi_{\dot{m}}$, the approximate covariances calculated by linearization are provided in Equation 3-37. The linearized covariances are similar to those estimated from sigma point transformations, with the only differences occurring in the terms that include mass flow rate, which has a non-linear relationship with total gas cell composition.

$$\boldsymbol{R_{ww}} \approx \begin{bmatrix} \Phi_{Z_{in}} & \Phi_{Z_{in}}\left(1-e^{-\frac{\Delta t}{\hat{\tau}}}\right) & 0 \\ \Phi_{Z_{in}}\left(1-e^{-\frac{\Delta t}{\hat{\tau}}}\right) & \Phi_{Z_{in}}\left(1-e^{-\frac{\Delta t}{\hat{\tau}}}\right)^2 + \Phi_{\dot{m}}\left[\frac{\Delta t}{m}e^{-\frac{\Delta t}{\hat{\tau}}}\left(\hat{Z}_{in}-\hat{Z}_{cell}\right)\right]^2 & \Phi_{\dot{m}}\frac{\Delta t}{m}e^{-\frac{\Delta t}{\hat{\tau}}}\left(\hat{Z}_{in}-\hat{Z}_{cell}\right) \\ 0 & \Phi_{\dot{m}}\frac{\Delta t}{m}e^{-\frac{\Delta t}{\hat{\tau}}}\left(\hat{Z}_{in}-\hat{Z}_{cell}\right) & 0 \end{bmatrix} \tag{3-37}$$

3.3 FTIR Simulations

To validate and determine the performance limitations of the UKF, simulations are performed of sample with transient composition flowing through a FTIR gas cell at a constant flowrate. Two types of simulations are performed: CFD and MN. In the CFD simulations, the sample consists of nitrogen mixed with a tracer component with identical properties (density and viscosity). The CFD simulations are used to verify the accuracy of the well-mixed model by comparing total gas cell composition calculated by the two models for identical inlet composition profiles. Synthetic FTIR measurements are also generated from the total gas cell composition calculations from CFD, which are used to explore the limitations of the filter and how inlet composition process noise influences performance. In the MN simulations, simulated engine exhaust from an FTP driving cycle flows through the FTIR gas cell. The total gas cell nitric oxide (NO) composition calculated in these simulations is used to produce synthetic FTIR NO measurements. MN simulations are used for cases involving simulated exhaust, since the FTP driving cycle lasts over 1800 seconds, a simulation time that would be computationally prohibitive for CFD. Engine-out NO emissions are simulated using the model from [95], which determines emission levels for a given vehicle speed and acceleration. The vehicle parameters used for this study are the same as those in [95]. An illustration of the process of generating synthetic FTIR measurements from the total gas cell composition values of the CFD/MN simulations is presented in Figure 3-4. This process consists of adding random noise from a Gaussian distribution to total gas cell composition calculations.

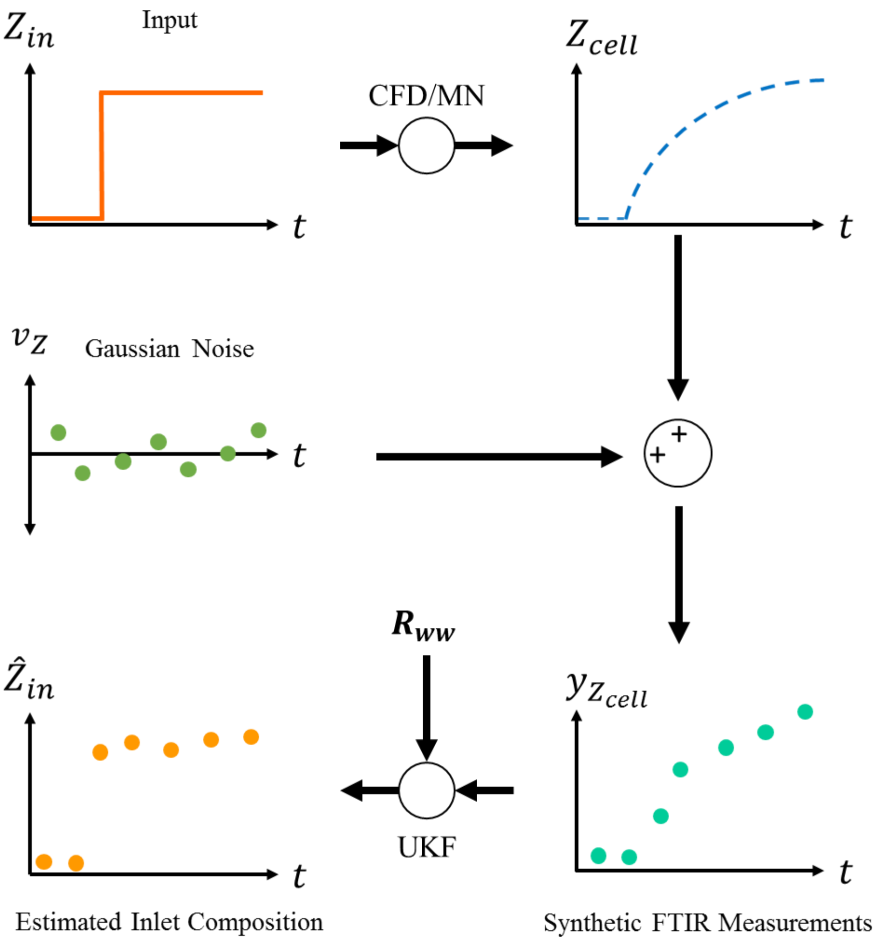

Figure 3-4: An illustration of the process for generating synthetic FTIR measurements from CFD/MN simulations, which are subsequently filtered by the UKF to generate inlet composition estimations.

Sample flow rates of 10 and 25 lpm are explored for both types of simulations. The lower flow rate is within the typical range used for FTIR experiments involving engine exhaust characterization. However, simulations with a flow rate of 25 lpm are also conducted to quantify the improvements in inlet composition estimation when flow rate is maximized. At higher flow rates, sample within the FTIR gas cell is displaced more quickly, yielding a total gas cell composition that more closely resembles the inlet composition and reduces the lagging effect between inlet and gas cell composition. However, it should be reiterated that high flow rates can increase measurement noise, limiting the advantages of increasing flow rate beyond a certain point. Also, increasing flowrate reduces the pressure within the FTIR gas cell due to restrictive upstream particulate filters which are necessary to maintain the quality and reflectance of the mirrors within the gas cell. The farther that gas cell pressure is from the calibrated pressures, the less reliable the measurements. Furthermore, reducing pressure results in lower absorbance of the sample, diminishing sensitivity. The details for the CFD and MN simulations will now be discussed.

3.3.1 Computational Fluid Dynamics

The computational domain used for the CFD simulations is based on the gas cell of the MKS 2030 HS FTIR, which has a volume of approximately 200 mL and inlet/outlet pipes with diameters of 3/8”. Unsteady, compressible, RNG k-ε turbulence simulations are performed using Converge CFD software. The RNG k-ε model is chosen over the standard k-ε model, as the RNG k-ε outperforms the standard model for cases involving impingement [96], which occurs within the gas cell on the opposite wall from the inlet. A temperature of 191°C is imposed at the domain boundaries and inlet, since the MKS 2030 is controlled to maintain this temperature. Near-boundary velocity is calculated using the law of the wall. Flow through the gas cell is induced through pressure boundary conditions set at the inlet and outlet. For the 10 and 25 lpm cases, approximately 70,000 and 250,000 cells are used, respectively. Grid refinement is applied within the inlet jet and near the boundaries of the gas cell and surrounding pipes to resolve composition and velocity gradients. Mesh independence is verified by increasing the number of computational cells until gas cell tracer composition changed by no more than 1% at any time during the simulation. To allow the inlet flow to adequately develop, 2 inches of the inlet pipe are included in the computational domain. Results from an additional simulation with a 4-inch inlet pipe at a flow rate of 25 lpm suggest that 2 inches is an adequate length, as the total gas cell tracer composition changed no more than 1% at any time. 3D and 2D diagrams of the computational domain are shown in Figure 3-5.

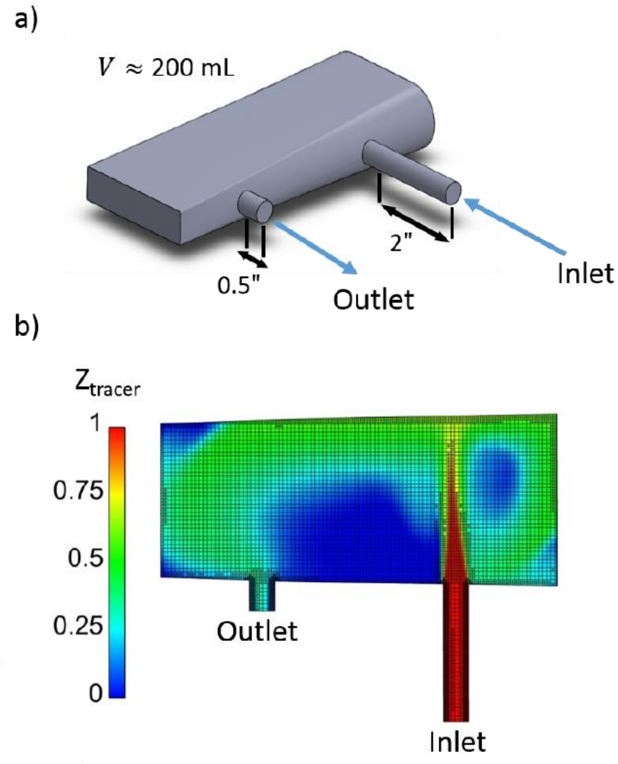

Figure 3-5: a) 3-D schematic of the FTIR gas cell used for CFD simulations. b) Top-down slice of the CFD computational grid, colored according to tracer mass fraction. The snapshot is taken 0.15 seconds after tracer is introduced at the gas cell inlet for the 25 lpm case.

3.3.2 Mixing Network

The MN model is a combination of plug-flow and well-mixed systems which collectively represent the FTIR gas cell. This model is designed to provide a simple yet accurate portrayal of the gas cell mixing dynamics and their effect on total gas cell composition. Ultimately, the MN calculates total gas cell composition for a given inlet composition profile and flow rate by summing the composition of each system normalized by its respective size. Figure 3-6 shows the layout of the MN. As shown, the model consists of a well-mixed system, followed by two plug-flow systems in parallel. An additional well-mixed system follows one of the plug-flow systems. The initial well-mixed system (1) represents an arbitrary volume immediately adjacent to the gas cell inlet. As shown in Figure 3-5, a well-mixed system is appropriate here, since the inlet sample quickly mixes with the surrounding sample, as indicated by the steep gradients in tracer composition near the inlet. The plug-flow system (2) accounts for sample from the well-mixed system that “short-circuits” or exits the gas cell without thoroughly mixing with the remaining gas cell contents. Mixing effects between system 1 and the remainder of the gas cell are modelled with an additional well-mixed system (4). The preceding plug flow system (3) creates a time delay for when sample exits system 1 and mixes into system 4, which is necessary to prevent inlet sample from immediately exiting the gas cell.

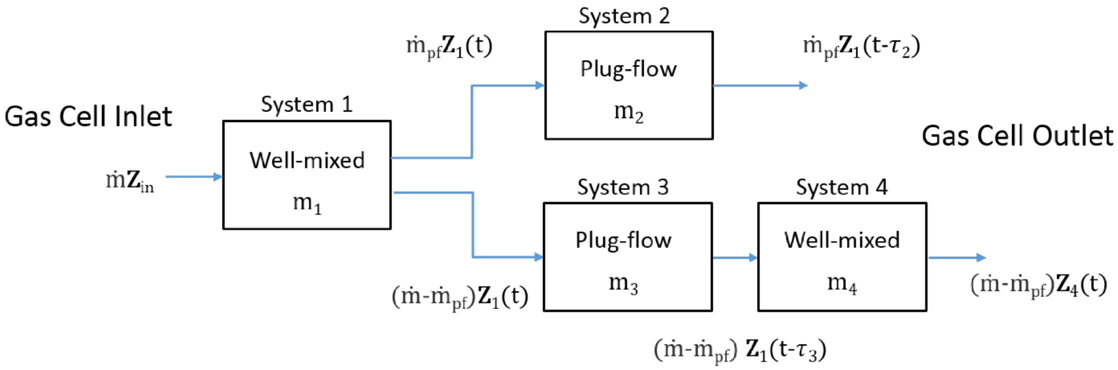

Figure 3-6: MN model used to determine composition inside FTIR gas cell.

To achieve accurate total gas cell composition calculations by the MN for a given inlet composition profile, the masses and flow rates of each system are optimized. Specifically, the optimized parameters are the masses occupied by systems 1-4 (m_1, m_2, m_3 and m_4), and the mass flow rate which passes through system 2 ($\dot{m}_{\mathrm{pf}}$). Optimization is achieved with a genetic algorithm (GA). The GA optimizes these parameters based on total gas cell tracer composition profiles from CFD simulations. Fitness for a given population of parameters is calculated by summing the absolute deviation of the total gas cell composition between the MN and CFD simulations for identical inlet composition profiles. Training is performed with two inlet composition profiles: a step change from nitrogen to tracer, and a tracer “impulse”, where tracer is introduced at the inlet for 0.2 seconds. Population sizes of 100 with an elitism replacement and mutation rate of 0.03 and 0.04 are utilized in the GA, respectively. 2000 generations are performed. The optimal parameters for each flow rate are given in Table 3-1.

$\dot{V}$ (lpm)	$\dot{m}_{\mathrm{pf}}/\dot{m}$	m_1/m	m_2/m	m_3/m	m_4/m
10	0.512	0.168	0.107	0.237	0.488
25	0.483	0.152	0.106	0.227	0.515

Table 3-1: Optimized system masses and plug-flow pathway flow rates for the MN model.

3.4 Computational Validation

This section is outlined as follows. First, results from CFD, MN and the well-mixed model simulations are presented. Total gas cell composition for the step and impulse tracer profiles are compared for each simulation type. Next, inlet tracer composition profiles estimated by the UKF for the step change profile are presented, demonstrating how the performance of the UKF varies with respect to measurement noise and inlet composition process noise. Estimated inlet tracer composition profiles for step and sine wave profiles of various frequencies are then presented. These results illustrate the limitations of the UKF in terms of accuracy and response time in detecting instantaneous and gradual composition changes. Next, UKF estimations of synthetic NO emissions for the FTP driving cycle are presented. The improvement in the estimation of instantaneous NO emitted from an engine compared to raw, unfiltered FTIR measurements for different measurement noise levels is demonstrated. Finally, the NO emission estimations from the UKF are compared to estimations from the well-mixed model uncoupled from the UKF, illustrating the importance of using a filter for mitigating measurement noise effects.

3.4.1 Evaluation of Well-Mixed Model

For the UKF to perform well, the well-mixed model must accurately represent how total gas cell composition changes with respect to time for a given inlet composition profile. To verify the fidelity of the well-mixed model, total gas cell composition calculations from the well-mixed model are compared to compositions calculated by CFD simulations for various inlet profiles and flow rates. Figure 3-7 shows the calculated total gas cell composition for the step and impulse inlet tracer composition profiles for flow rates of 10 and 25 lpm. There is reasonable agreement between the well-mixed model and the CFD results in every case. The maximum percent error for both step profiles is about 11%, while the maximum error for the impulse case for 10 and 25 lpm are about 16% and 14%, respectively. Maximum discrepancy between the two models for 10 and 25 lpm occur at about 300 and 100 milliseconds after the tracer is introduced, respectively, for both the impulse and step cases. In every case, the well-mixed model under-estimates total gas cell composition early after the onset of the composition change.

Discrepancy between the two models is explained by the plug-flow-like behavior predicted from the CFD. The well-mixed model assumes that sample entering the gas cell mixes instantaneously with the remaining contents, which causes some of the entering tracer to immediately escape the gas cell. However, the CFD results indicate that a finite minimum residence time exists within the gas cell. This phenomenon is apparent in the impulse cases in Figure 4, where the well-mixed model calculates a sharp decrease in tracer fraction immediately after the impulse completes, while the tracer fraction from the CFD plateaus briefly before decreasing. Despite their differences early on, the two profiles fall back into alignment within 400 milliseconds of the time of maximum discrepancy. Since the well-mixed model initially under-predicts the magnitude of total gas cell composition changes, the UKF initially over-estimates the magnitude of inlet composition changes. However, since the well-mixed model quickly falls back into agreement with the CFD results after the transient, the overshoot of inlet composition estimation is momentary. Furthermore, the overshoot issue is mitigated by adding process noise to the well-mixed model in the processor, which damps the response of the Bayesian estimation to measurement changes. As will be shown in the remainder of the chapter, the well-mixed model is sufficient for the UKF.

Also shown in Figure 3-7 is the total gas cell tracer composition calculated by the MN model. The MN profile closely mirros that of the CFD in every case. Discrepancies between the two profiles are imperceptible in the figure. This shows that the MN model accurately calculates total gas cell composition and is suitable for generating synthetic FTIR data for a given emissions profile.

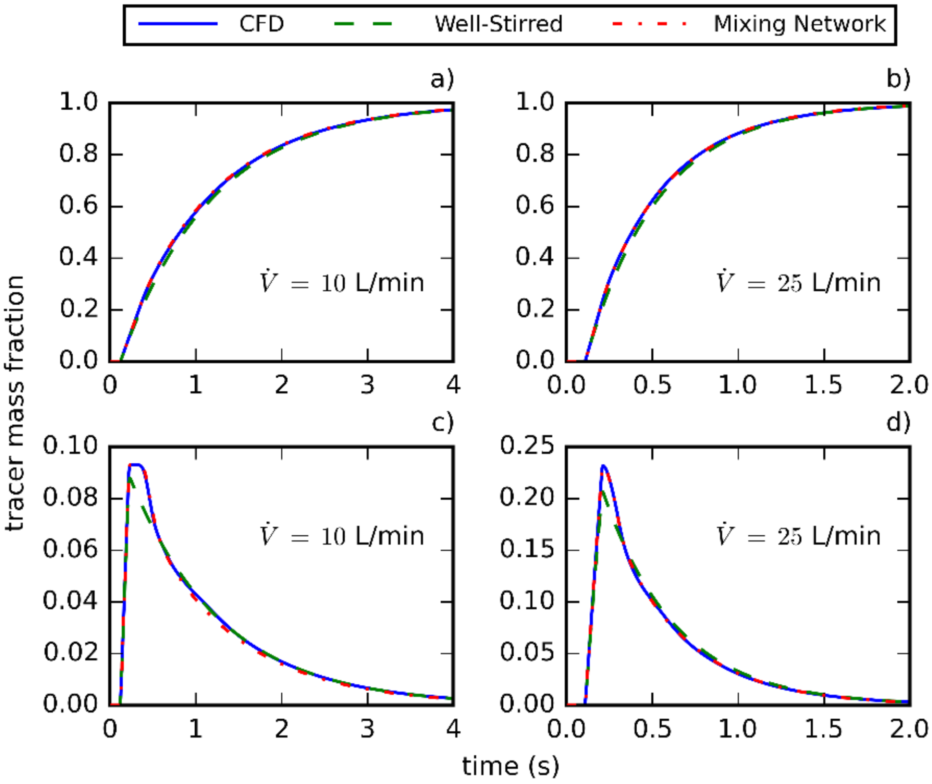

Figure 3-7: Calculated FTIR gas cell tracer composition for different inlet composition profiles and flow rates. a-b) step profile, c-d) "impulse" profile.

3.4.2 Filtered Tracer Data

To explore the effects of process and measurement noise on the response of the UKF to FTIR measurement changes, synthetic FTIR data is generated from the CFD calculations for the 10 lpm, step inlet profile case. The measurements are produced by adding white Gaussian noise to the calculated total gas cell tracer composition at intervals of 200 ms, which is the measurement period of the MKS 2030 HS FTIR. These synthetic measurements are processed with the UKF, which produced estimates for the inlet tracer composition. Figure 3-8 shows the estimated inlet tracer composition for various inlet composition process noise ($w_{Z_{in}}$) and FTIR measurement noise (v_Z) values. The inlet composition process noise term determines how readily the estimate for inlet composition is adjusted by the UKF. A higher value makes inlet composition estimations more sensitive to changes in measured gas cell composition. In this analysis, it is assumed that the measurement noise covariance is known, and the covariances of $\boldsymbol{R_{vv}}$ in Eq. 3-22 are equal to the covariances of the Gaussian noise used to generate synthetic measurements. Higher measurement noise results in the UKF estimations being less sensitive to measurement changes, since outlying measurements are more likely to be due to noise than true composition changes. In Figure 3-8, the inlet composition process noise standard deviations are varied between three values – 0.02, 0.07 and 0.12. Measurement noise standard deviations are varied between 0.01, 0.025 and 0.05. Mass flow rate noise is assumed to have a standard deviation of 1% of the flow rate.

The previously discussed trends associated with changes in inlet composition process noise and FTIR measurement noise are apparent in Figure 3-8. As the inlet composition process noise increases, the response time of the inlet composition estimations decreases. This is apparent in parts d and g of the figure, where the estimated inlet composition reaches the actual inlet composition within 3 measurement periods (600 milliseconds) after the step change. However, excessive process noise variance results in a noisy estimated inlet composition profile, as shown in g, as estimations become overly sensitive to measurement noise. The effects of measurement noise are apparent when comparing the estimated inlet composition on a column-by-column basis. Plots toward the right correspond to cases with greater measurement noise. As measurement noise increases, the lagging effect on the inlet composition estimations worsen. The case with the highest measurement and lowest process noise (c) results in an inlet composition estimation that deviates from the actual inlet composition further than the raw FTIR measurements. A standard deviation of 7% of the range of inlet composition values provides a satisfactory combination of response time and stability, and is therefore used as the process noise for the remainder of the UKF response time analysis.

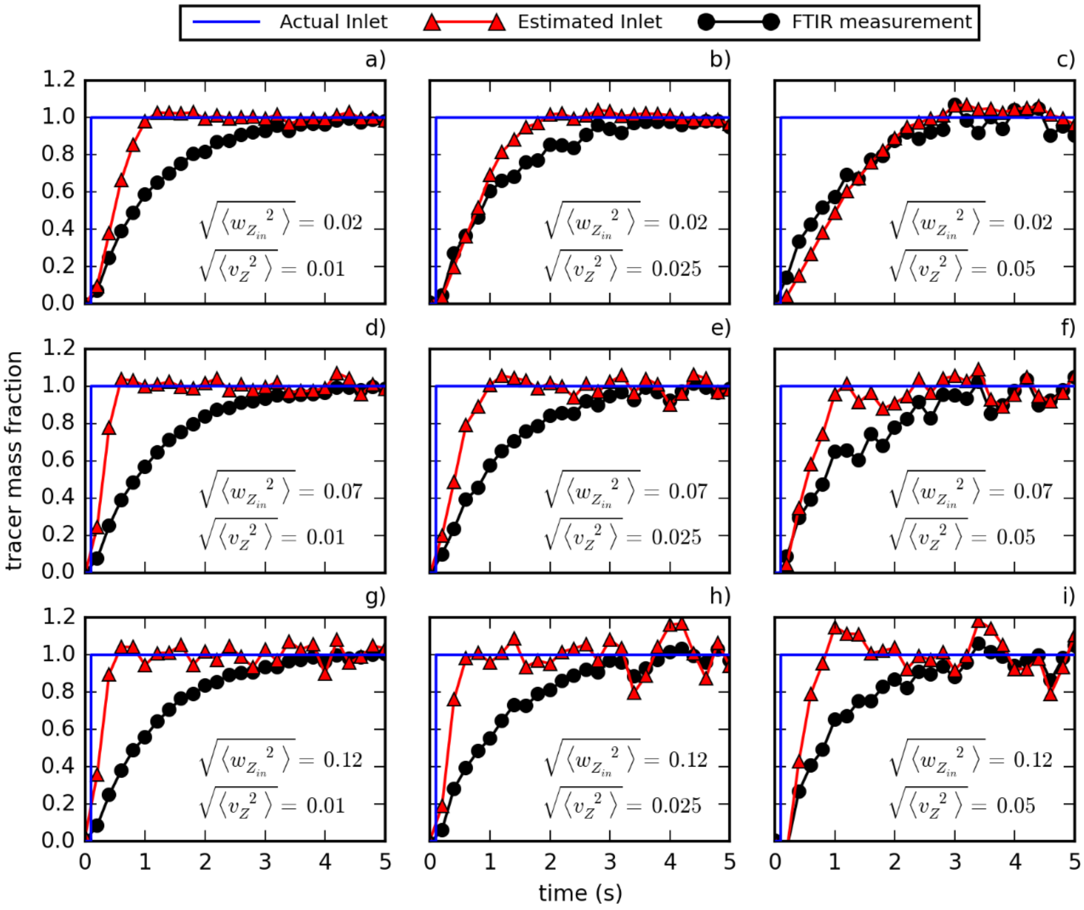

Figure 3-8: Inlet tracer composition estimations by the UKF for various process and measurement noise values. $\dot{V}$ = 10 lpm.

To quantify the limits of the UKF in terms of response time, synthetic FTIR measurements are generated for step changes in inlet tracer composition at varying frequencies. These measurements are processed with the UKF, and the results are shown in Figure 3-9. Parts a and c of the figure show estimated inlet tracer composition for a step wave with a frequency of 1.25 Hz for flow rates of 10 and 25 lpm, respectively. This frequency is half the highest frequency that can be accurately sampled by the FTIR – which measures at 5 Hz – according to the Nyquist theorem. At this frequency, the UKF estimates a reasonably accurate profile for the inlet composition, although greater accuracy is achieved for the higher flow rate. The reason better estimations are attained at higher flow rates is explained by the rate at which sample is replenished within the gas cell. For example, at lower flow rates, less sample enters/exits the gas cell during a measurement period. Therefore, substantial changes in inlet composition result in relatively modest changes in total gas cell composition/FTIR measurements. Consequently, these modest changes in FTIR measurements can be of comparable magnitude as measurement noise, preventing the UKF from detecting the inlet composition changes. Parts b and d of Figure 3-9 show estimated inlet tracer composition for a step changes at the Nyquist limit (2.5 Hz) for flow rates of 10 and 25 lpm, respectively. As shown, the overall measurement trend do not reflect the true changes in inlet composition. Thus, the UKF estimations are also poor at the Nyquist limit regardless of flow rate. These results illustrate that dramatic changes with duration less than 400 milliseconds may not be accurately detected.

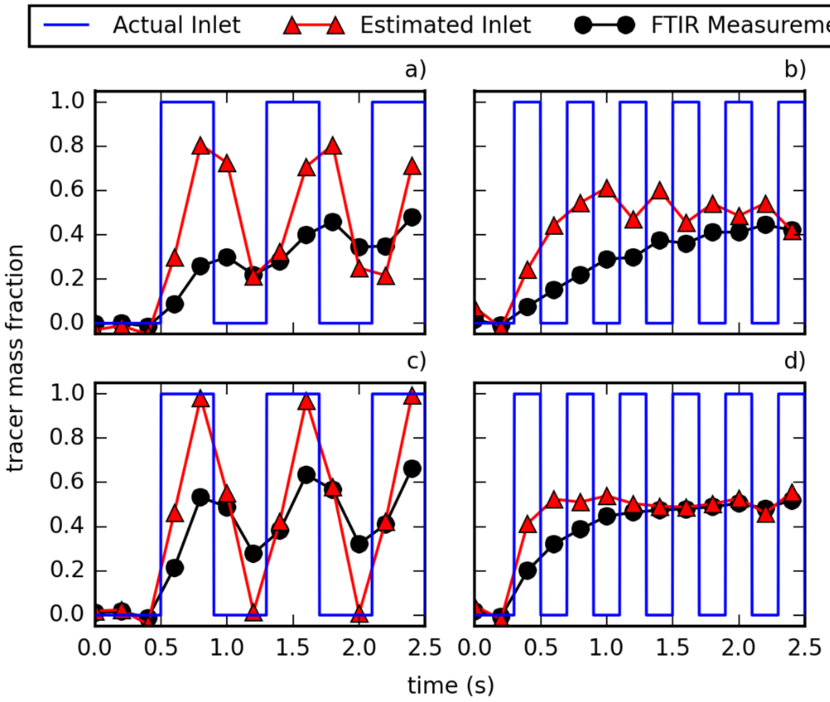

Figure 3-9: Inlet tracer composition estimations by the UKF for inlet composition step wave profiles at various frequencies and various flow rates. The standard deviation of the measurement noise (υ_Z) is 0.01. a) $\dot{V}$ = 10 lpm, f = 1.25 Hz; b) $\dot{V}$ = 10 lpm, f = 2.5 Hz; c) $\dot{V}$ = 25 lpm, f = 1.25 Hz; d) $\dot{V}$ = 25 lpm, f = 2.5 Hz.

Thus far, only Bayesian estimation results for instantaneous changes in composition have been presented. Since composition profiles are likely to contain gradual changes, the UKF is applied to synthetic data generated from sine wave tracer composition profiles with frequencies of 1.25 and 0.4 Hz. The results are shown in Figure 3-10. In all cases, the estimated inlet composition lags the actual inlet composition. This lagging effect is due to the quasi-steady nature of the UKF. Since the profile of the inlet composition between measurements is unknown, the UKF assumes that inlet composition remains constant during a measurement period and calculates its estimation accordingly. The estimation lag is more pronounced for sine waves with higher frequency, since the inlet composition evolves more rapidly between measurements. This can be seen by comparing the first column and second columns of plots in Figure 3-10, which have inlet composition frequencies of 1.25 Hz and 0.4 Hz, respectively. Just as in the step wave cases, better estimations are achieved for higher flow rates, which can be seen by comparing the plots on a row-by-row basis. Despite the lag in estimated inlet composition, nearly every estimation is closer to the true inlet composition than the raw FTIR measurement. Moreover, the overall profile of the estimated inlet composition resembles the actual inlet composition more closely than the profile of the FTIR measurements in every case.

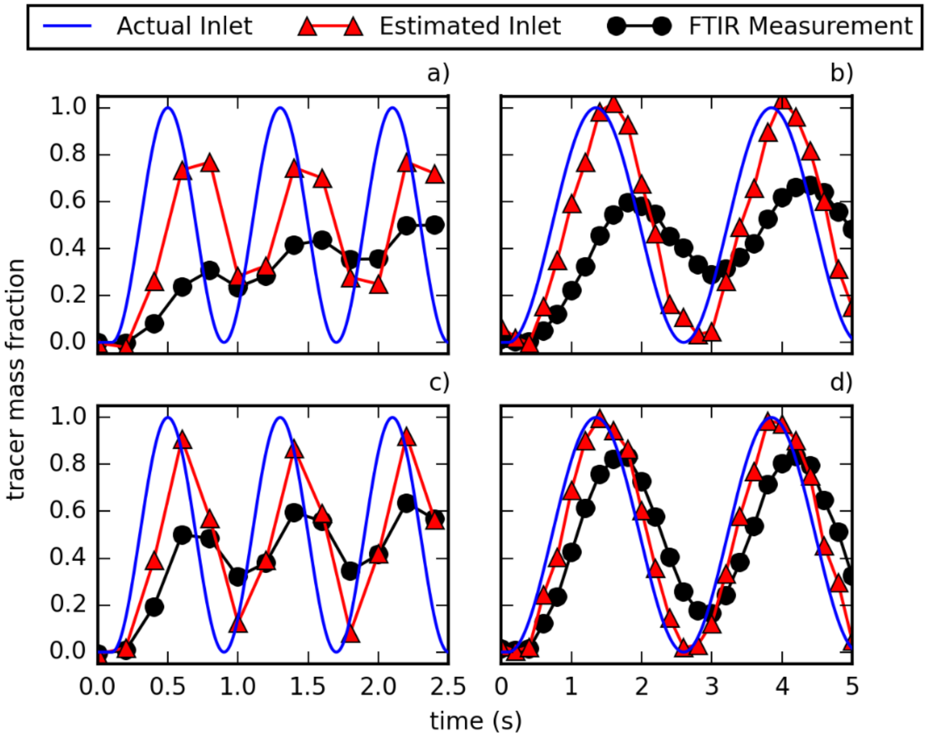

Figure 3-10: Estimated inlet tracer composition for inlet composition sine wave profiles at various frequencies and various flow rates. The standard deviation of the measurement noise (v_Z) is 0.01. a) $\dot{V}$ = 10 lpm, f = 1.25 Hz; b) $\dot{V}$ = 10 lpm, f = 0.4 Hz; c) $\dot{V}$ = 25 lpm, f = 1.25 Hz; d) $\dot{V}$ = 25 lpm, f = 0.4 Hz.

3.4.3 Filtered Synthetic Emissions Data

To evaluate how the UKF may perform when processing emissions data, synthetic NO emissions from the FTP driving cycle are generated using the emissions model from [95]. These synthetic NO measurements are then processed with the UKF, and the resulting NO estimations are compared with the true synthetic NO emissions at each measurement time. The emissions model is calibrated to estimate emissions of a limited number of species given vehicle speed, acceleration, and parameters (such as mass and drag coefficient). The vehicle parameters used to produce the synthetic NO measurements are identical to the parameters used to generate the example data in [95]. MN simulations are conducted with the synthetic NO emissions data used as the gas cell inlet composition profile. Synthetic FTIR measurements are produced by adding white Gaussian noise to the total gas cell NO composition calculated from the MN simulations. It should be noted that although the MN model yields more accurate calculations of gas cell composition than the well-mixed model, the well-mixed model is still preferred as the state-transition model for the UKF, since the system masses and pathway flow rates of the MN model are optimized for specific total flow rates and gas cell geometry of this work, are not likely not generally applicable to other FTIRs. Another key point to be noted is that the UKF is equally applicable to all other measurable species (aside from non-stationarity and spectral noise effects, which can vary between species and are discussed in more detail in Chapters 4 and 5, respectively). NO is selected arbitrarily, as the purpose of this analysis is to simply demonstrate how the UKF combats sample recirculation effects for more realistic emissions profiles. This task can be accomplished with any of the species within the emissions model. Inlet composition process noise covariance ($\Phi_{Z_{in}}$) is set as the covariance of NO emissions fluctuations between consecutive measurement times over the entire driving cycle.

Figures 3-11 and 3-12 show a snippet of the NO emissions profiles estimated by the UKF for sample flow rates of 10 and 25 lpm, respectively. The snippet of the driving cycle from 20 to 40 seconds is presented since it contains a combination of gradual and abrupt transients, as well as a steady-state portion. Estimated NO emissions are presented for a range of measurement noise levels, since noise levels vary according to a wide range of factors such as the absorptivity, the quantity of the species of interest and the presence of interfering compounds [97]. The UKF generally improves the estimation of the simulated NO emissions compared to raw FTIR measurements, although this improvement becomes more modest as measurement noise increases. As shown in the top subplots of both figures, when the standard deviation of the measurement noise is 10 ppm, the estimated NO profile closely follows the actual profile and accurately captures transients. However, for a measurement noise standard deviation of 80 ppm, the estimated inlet composition and raw measurements are of comparable resemblance to the actual NO profile, as shown in the bottom subplots. The UKF provides greater improvement from raw measurements for the lower flow rate. This is due to residence times within the gas cell being shorter at higher flow rates, reducing the lagging effect of historic emissions on the total gas cell composition. In other words, measurements at higher flow rates have less room for improvement. However, some improvement in NO estimation is still present at the higher flow rate case, especially for smaller measurement noise values.

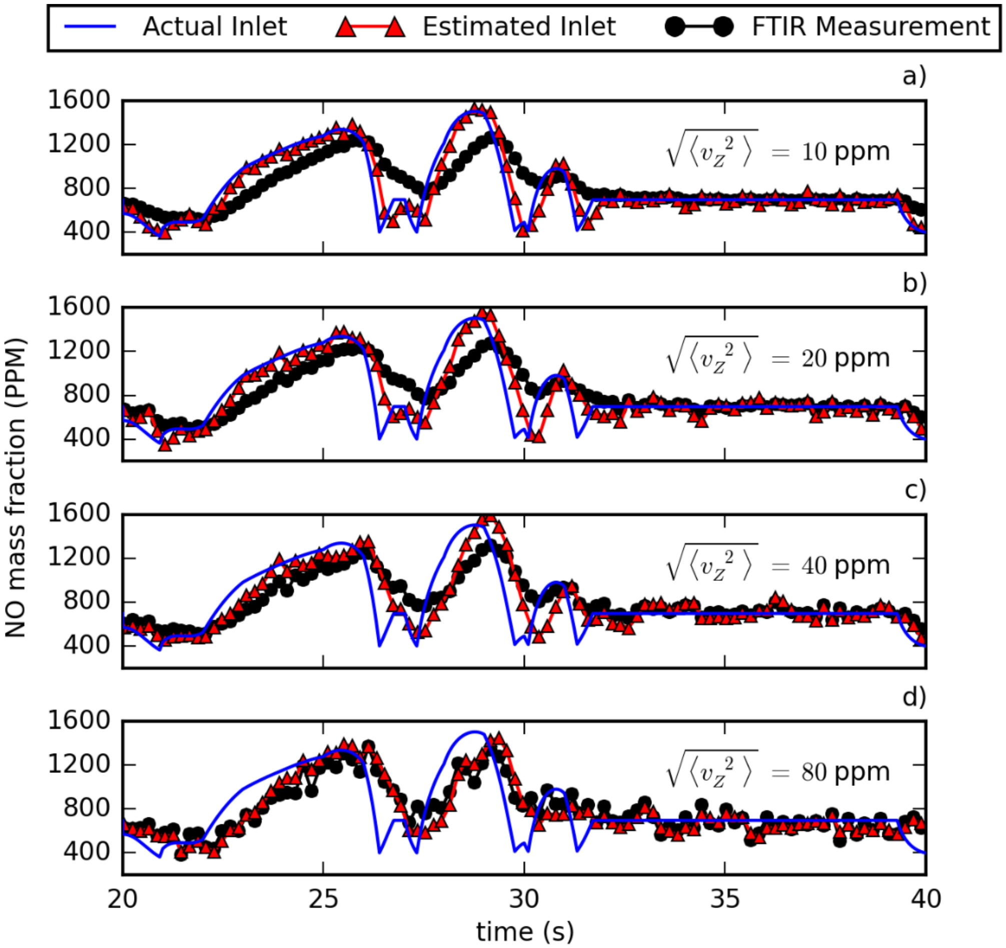

Figure 3-11: Estimated NO emissions from an FTP driving cycle from 20 to 40 seconds for a FTIR flow rate of 10 lpm.

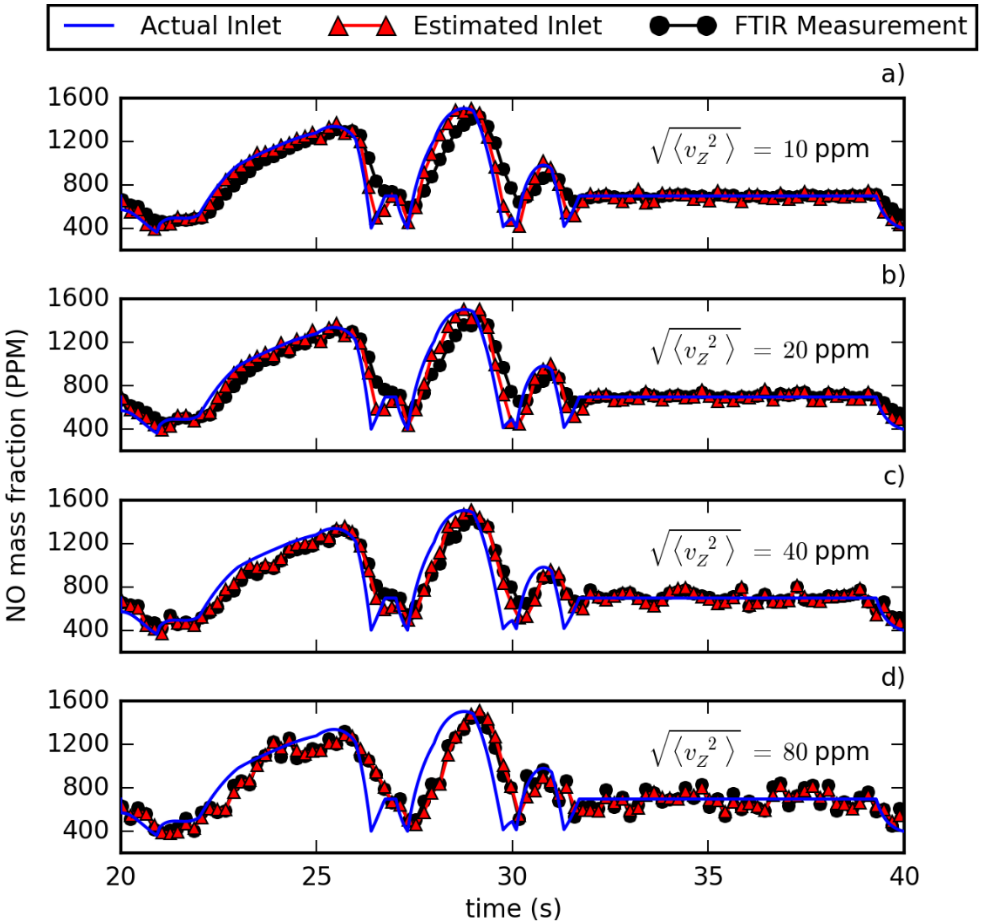

Figure 3-12: Estimated NO emissions from an FTP driving cycle from 20 to 40 seconds for a FTIR flow rate of 25 lpm.

The improvement in estimated emissions from the UKF compared to raw FTIR measurements is quantified in terms of instantaneous and integrated emissions in Figures 3-13 and 3-14, respectively. As shown Figure 3-13, the UKF improves the estimation of instantaneous NO emissions by more than 40% on average compared to raw FTIR measurements for the lowest measurement noise presented. As measurement noise increases, this improvement declines. At a measurement noise standard deviation 80 ppm, the UKF provides modest improvement in instantaneous emission estimates for either flow rate. Decreased performance of the UKF for high measurement noise values is explained by the contribution of noise to measurement error, and the fact that measurement noise desensitizes the NO emission estimates to measurement changes. At measurement noise standard deviations as high as 80 ppm for these emissions profiles, the contributions of noise to measurement changes regularly exceed that of true gas cell composition changes, completely masking the true gas cell composition profile. Another significant contributor to the average instantaneous NO estimation error is the noisiness of the estimations during steady-state. In fact, the raw FTIR measurements often resemble the actual NO emissions during steady-state more closely than the UKF estimations for noise standard deviation of 10 and 20 ppm. The noisiness of the estimations during steady-state is due to slight oversensitivity to measurement noise, which is ultimately caused by high inlet composition process noise. However, high process noise is necessary since it permits NO estimations to be properly adjusted during steep transients. Further improvement in performance of the UKF could be achieved by using an adaptive process noise covariance matrix, where process noise would increase during transients and decrease during steady-state [98], [99]. This would allow the UKF to readily adjust emissions estimations during abrupt transients, while providing stability for gradually evolving or steady emissions.

Figure 3-14 shows the error in integrated NO emissions with respect to time over the entire driving cycle from the UKF and raw FTIR measurement. Again, the UKF yields significantly improved integrated emissions calculations compared to raw data, especially for low measurement noise levels. However, the integrated emissions calculated from FTIR measurements are also accurate, with the greatest percent error being less than 3%. The lower errors for integrated emissions compared to instantaneous emissions are due to the cancellation of positive and negative errors in instantaneous emissions during integration.

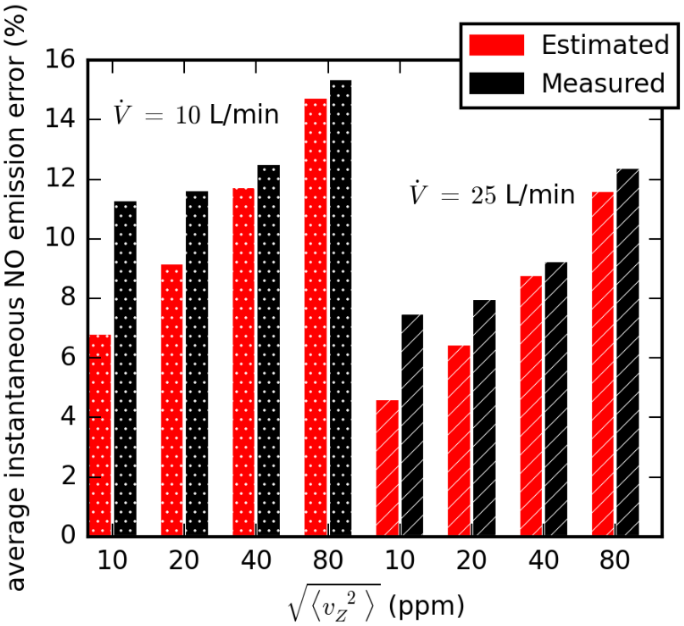

Figure 3-13: Average absolute percent error of instantaneous NO emissions calculated from estimations from the UKF (red) and raw synthetic FTIR measurements (black) for different flow rates and measurement noise levels.

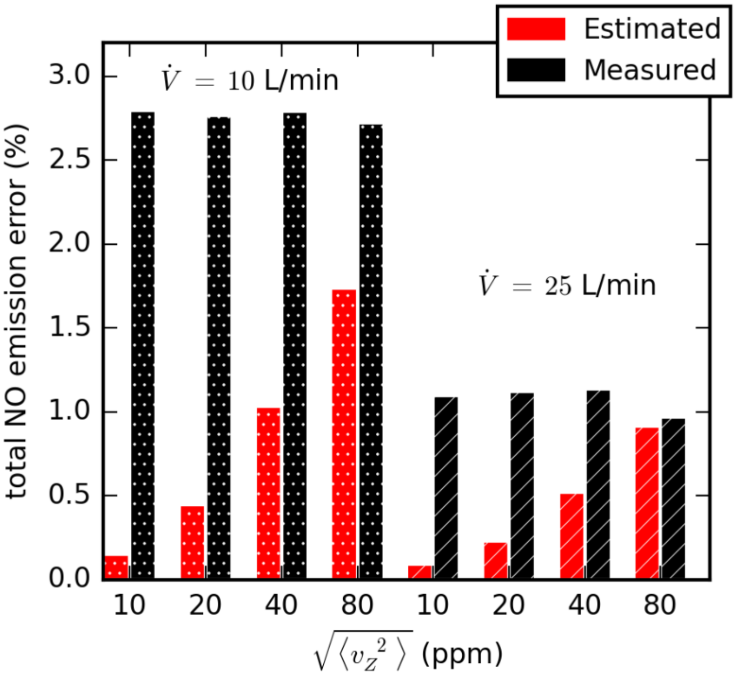

Figure 3-14: Percent error of integrated NO emissions calculated from estimations from the UKF (red) and raw synthetic FTIR measurements (black) for different flow rates and measurement noise levels.

To prove the necessity of a Bayesian filter for accurately estimating emissions, NO estimations calculated from the UKF are compared to estimations from the well-mixed model uncoupled from a filter for the FTP driving cycle. The stand-alone well-mixed model estimates the inlet composition solely by deducing the inlet composition from measurement changes and takes no account of measurement noise. Comparisons of estimated NO composition between the two models for two different flow rates and measurement noise values are shown in Figure 3-15. The stand-alone well-mixed model yields noisy estimations which oscillate above and below the true NO emissions, although the degree of estimation noise depends on flow rate and measurement noise. Emissions estimations become noisier as measurement noise increases and flow rate decreases. For the 10 lpm, 40 ppm noise standard deviation case, emissions estimations are chaotic and contain many erroneous oscillations that are not present in the true emissions profile. By comparison, the UKF and stand-alone well-mixed model perform similarly for the 25 lpm, 20 ppm case, although the stand-alone model still produces a few erroneous spikes, which are very apparent during the steady-state. Overall, it is clear that the Bayesian filter becomes more impactful as measurement noise increases and flow rate decreases.

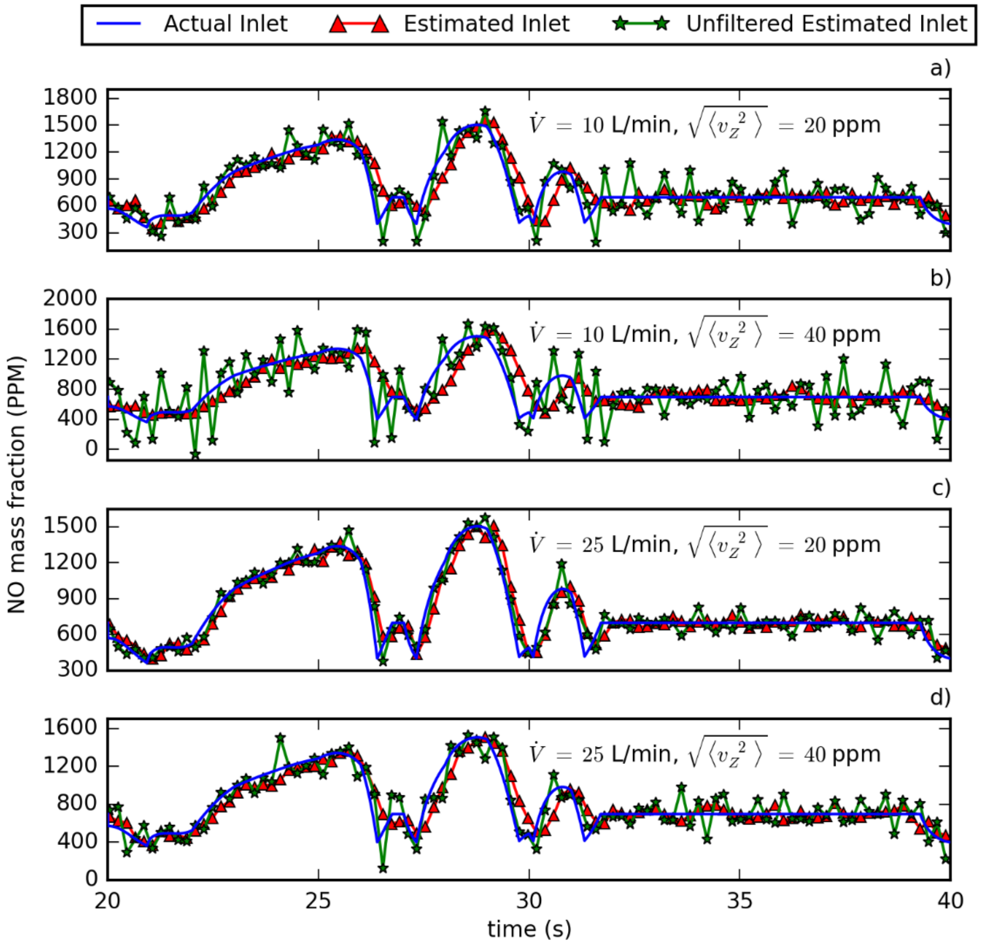

Figure 3-15: Estimated NO emissions from an FTP driving cycle from 20 to 40 seconds from the UKF and the well-mixed model uncoupled from a filter for various noise levels and FTIR flow rates.

To quantify the performance differences between the UKF and the stand-alone well-mixed model, errors in instantaneous and integrated NO emissions from each model are presented. Figure 3-16 shows the average error in instantaneous NO emissions for the entire FTP driving cycle for different flow rates and measurement noise values. As expected given the results in Figure 3-15, errors in instantaneous NO emissions are significantly greater for the stand-alone well-mixed model compared to the UKF for a flow rate of 10 lpm. For noise standard deviations of 20 and 40 ppm, the average errors of the uncoupled well-mixed model calculations are nearly double and triple the errors of the UKF calculations, respectively. At the higher flow rate, performance improvements by the UKF over the stand-alone well-mixed model are less significant. For the 25 lpm, 20 ppm noise standard deviation case, the UKF achieves a mere 20% relative improvement over the stand-alone well-mixed model, and the error of the stand-alone model itself is already low at 8%. Again, the favorable results at higher flow rates are due to short residence times within the gas cell, which makes inlet composition estimates less sensitive to measurement noise. However, it should be noted that the lagging effect becomes more impactful as the frequencies of inlet composition oscillations increase. For a more erratic emissions profile with oscillation durations that rival gas cell residence times, the Bayesian filter would become more essential. It should be reiterated that there is an upper limit on the allowable sample flow rates of FTIR measurements due to noise and pressure effects. The purpose of presenting results for higher flow rates is to demonstrate the benefit of maximizing flow rate up until the introduction of these additional sources of error.

Figure 3-17 shows the error in integrated emissions from the UKF and the stand-alone well-mixed model. Interestingly, the integrated emissions from the stand-alone well-mixed model are more accurate in every case, despite the instantaneous emissions estimations from the stand-alone model being consistently worse than those from the UKF. Again, lower integrated emissions errors compared to instantaneous errors are due to the cancellation of positive and negative errors during the integration process. The superiority of the integrated emissions from the stand-alone model is attributed to the fact that its estimations contain the unaltered effects of measurement noise. Since mean measurement noise approaches zero over many measurements, noise effects are more efficiently cancelled over integration of the entire driving cycle. Conversely, the UKF filters noise effects in a complicated way that may introduce biases that result in non-zero error means. Another possible culprit for this trend is error introduced from filter lag, where emerges due to the quasi-steady model. Nevertheless, the UKF substantially improves instantaneous emissions estimations, while errors in integrated emissions remain low for both the UKF and stand-alone well-mixed model.

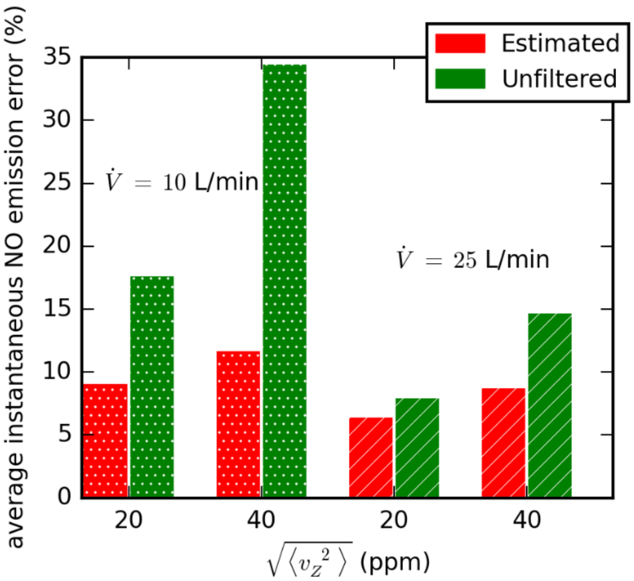

Figure 3-16: Average percent error of instantaneous NO emissions calculated from estimations from the UKF (red) and the well-mixed model uncoupled from a filter (green) for different flow rates and measurement noise levels.

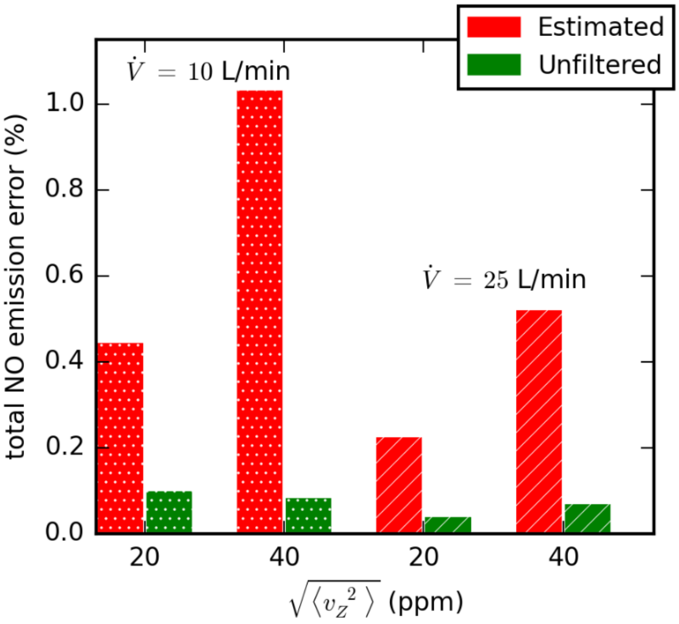

Figure 3-17: Percent error of integrated NO emissions calculated from estimations from the UKF (red) and the well-mixed model uncoupled from a filter (green) for different flow rates and measurement noise levels.

3.5 Chapter Summary

In this chapter, a UKF is developed for processing FTIR measurements to obtain accurate estimations of instantaneous engine exhaust composition during transients. The UKF addresses the biasing effects of sample recirculation by utilizing a well-mixed model, as well as estimated measurement noise and emissions fluctuation statistics to infer FTIR gas cell inlet composition from consecutive measurement changes. To validate the UKF and explore its performance limitations, synthetic FTIR measurements are generated for transient tracer gas flow sequences and simulated NO engine exhaust data from the FTP drive cycle. These synthetic measurements are processed by the UKF, which is shown to yield improved estimations of instantaneous composition compared to the raw, unfiltered FTIR measurements, although the degree of improvement depends on the magnitude of measurement noise, sample flow rate, and the magnitude and frequency of emissions oscillations and trajectory changes. For measurement noise standard deviations of 10, 20, 40 and 80 ppm, the UKF achieves improvements in estimated instantaneous NO emissions of 39.6%, 21.1%, 6.3% and 4.1%, respectively, compared to raw FTIR measurements for a sample flow rate of 10 lpm. For a sample flow rate of 25 lpm, improvements of 38.4%, 18.9%, 4.9% and 6.2% are respectively achieved by the UKF.

The computational results presented in this chapter show promise for the Bayesian approach for combating residence time effects to improve engine emissions estimations from FTIR measurements during transients. However, for the UKF to yield accurate results in an experimental setting, it must also address biasing effects due to signal non-stationarity. Signal non-stationarity refers to the evolution of spectral power of the modulated IR beam during a FTIR measurement due to evolving concentrations within the FTIR gas cell. The subsequent chapter is devoted to describing the stationarity effects on FTIR measurements in more detail, as well as the augmentation of the UKF developed in this chapter to account for these effects. Experimental validation of the augmented UKF is also presented.

CHAPTER 4 EXPERIMENTAL VALIDATION OF BAYESIAN ESTIMATOR

The work presented in this chapter addresses the biasing effects of signal non-stationarity that are shown to be present during FTIR measurements of chemically evolving samples. Such effects must be addressed and factored within the UKF to achieve reasonable inlet composition estimations in experimental applications. Non-stationarity biasing effects arise from the fact that in FTIR spectroscopy, an interferogram is Fourier transformed to estimate spectral IR intensity, which is indicative of chemical composition. While reliable when spectral intensity (and therefore composition) is constant, the Fourier transform is biased when spectral intensity is non-stationary, resulting in calculated spectral intensities that are disproportionately weighted by intensity measurements at/near the centerburst location. Coupled with the fact that the moving mirror alternates scanning directions, this biasing effect creates anomalous oscillations in FTIR measurements that obscure true composition profiles. The modified UKF developed in this chapter accounts for non-stationarity biasing while estimating gas cell composition, mitigating these anomalous oscillations. Experimental validation of the modified UKF is performed by flowing mixtures with transient, trace concentrations of acetylene and propylene through the FTIR, and filtering the resulting measurements with the UKF. The UKF is shown to yield substantially improved estimations of transient inlet composition compared to raw, unfiltered FTIR measurements.

This chapter is outlined as follows. First, the biasing effects of spectral IR non-stationarity are discussed, including its causes and implications. This is followed by a mathematical derivation of the Fourier transform of an interferogram generated by a uniformly broadened, linearly evolving spectral line. Such a simplified spectrum and power profile provides an analytical solution to the Fourier transform, which is used to explore the relationships between centerburst weighting and factors such as scan length and spectral broadening width. This mathematical analysis is expanded to produce a numerical method for estimating the degree of centerburst weighting for FTIR measurements of unique species. Centerburst weighting values for various species are then calculated and incorporated into the modified UKF, which is augmented to deduce gas cell composition from biased FTIR measurements. The procedure for experimentally validating the modified UKF is then described, and the chapter is concluded with a presentation and discussion of experimental results.

4.1 Non-Stationarity Bias

FTIRs are typically calibrated to map spectral IR absorbance to gas cell concentration, which are directly related through the Beer-Lambert law [100]. Spectral absorbance of a sample is estimated by Fourier transforming the measured interferogram, and comparing the resulting IR intensity spectrum to a background spectrum from a non-absorbing sample. While these calibrations are valid when composition is relatively steady and spectral absorbance is stationary, the relationships between the measured/calculated spectral absorbance and gas cell concentration become increasingly complicated for transient compositions. The Fourier transform calculates a single IR intensity spectrum, whether or not the spectrum is truly stationary throughout an interferogram. However, the spectral intensity of broadened absorption lines calculated by the Fourier Transform is NOT the average value of spectral intensity during a moving mirror scan, but rather is biased according to the profile of the spectral intensity with respect to optical path difference (OPD) of the split beams within the interferometer, which varies with moving mirror position. To further complicate things, the direction of the moving mirror scan alternates each measurement period in many commercial FTIRs. While this doubles the measurement frequency of the instrument (the repositioning of the moving mirror to the initial location is utilized as an additional scan), the profiles of moving mirror position relative to time are reversed for each measurement. This convolutes the task of determining composition profiles with respect to time from FTIR measurements.

To illustrate the complexities of FTIR measurements during transients, consider Figure 4-1 which shows FTIR measurements during step changes in inlet tracer composition of acetylene and propylene from approximately 70 to 170 ppm at sample flow rates of 12 slpm. Overall, the FTIR measurements follow approximately an exponential curve as expected. However, the measurements exhibit period-dependent behavior, where the composition output alternates between significant and gradual rise. These anomalous oscillations in the FTIR measurements cause the estimated inlet composition values from the UKF to oscillate as well, yielding severe errors. Furthermore, the severity of these errors is greater for propylene than acetylene. The cause of these oscillations is the alternation of the moving mirror direction for each measurement. Mathematical analysis, outlined in detail in the section 4.2, reveals that for a broadened spectral line with linearly changing ensemble-averaged intensity, the values calculated by the Fourier transform are heavily weighted by the intensity at/near the centerburst location. Here, the centerburst location is defined as the initial moving mirror position where it is equidistant from the beamsplitter as the stationary mirror, resulting in complete constructive interference between the split beams and zero OPD. The effect of centerburst weighting is illustrated in Figure 4-2. For a forward scan (from centerburst to maximum OPD), the centerburst occurs at the beginning of the scan. Therefore, the measured composition for a forward scan is heavily weighted by the composition near the beginning of the scan for a transient measurement. Conversely, the centerburst occurs at the end of the scan when the mirror moves in the backward direction, yielding a measured composition that is heavily weighted by the composition at the end of the scan. This alternation between weighing composition measurements more heavily at the beginning and ends of mirror scans is what causes the oscillatory behavior. Periods of gradual rise in the FTIR measurements in Figure 4-1 occur between successive backward/forward scans, since the centerburst position for these two scans occur closely together in time. Conversely, periods of significant rise occur for successive forward/backward scans, due to the centerburst locations being separated by two full scans.

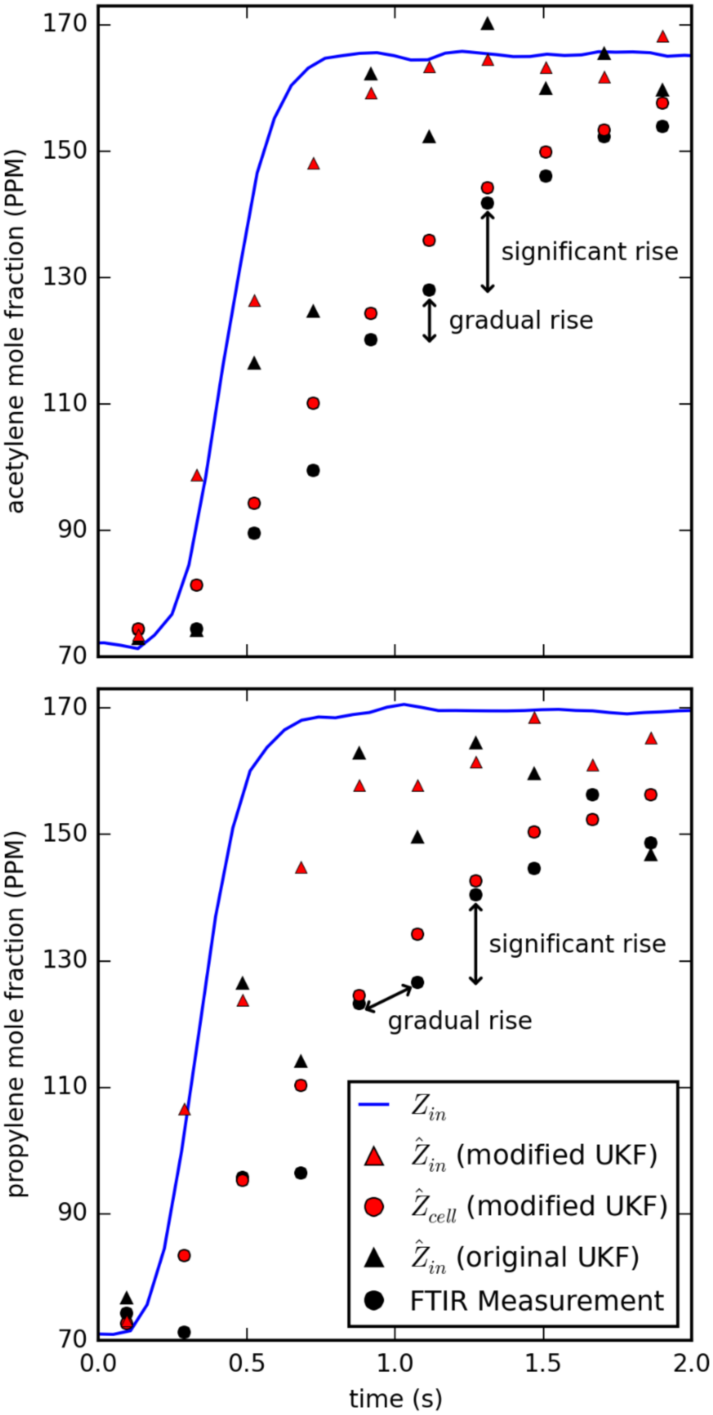

Figure 4-1: Estimated tracer inlet composition from the modified (red) and original (black) UKF. The modified UKF accounts for period dependent behavior of FTIR measurements.

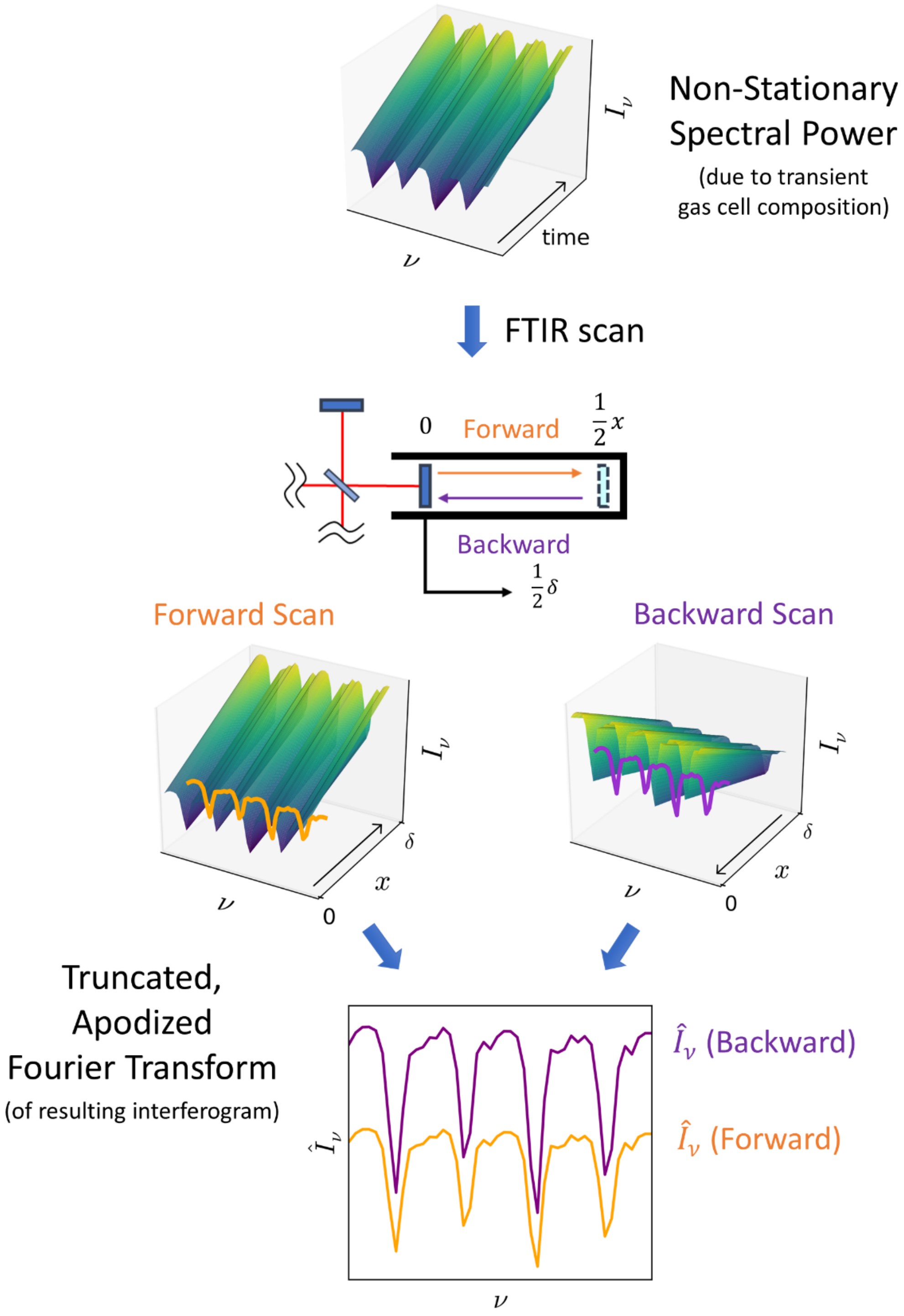

Figure 4-2: Illustration of how scan direction affects FTIR output. The upper figure shows an example IR spectrum with linearly increasing intensity (I) at various wavenumbers (ν). Different spectral intensities are calculated by the truncated, apodized Fourier transform depending if the mirror is scanning in the forward or backward direction. The variables x and δ represent OPD and maximum OPD, respectively.

4.2 Mathematical Model

To mathematically confirm that the period-dependent behavior observed in the FTIR measurements from Figure 4-1 are indeed due to centerburst weighting/alternating scan directions, Fourier transforms of synthetic interferograms generated from non-stationary frequency components are performed. First, the Fourier transform of an interferogram from a single, uniformly broadened spectral line with linearly evolving power with respect to OPD is derived. The resulting calculation for this spectrum and power profile is analytical, permitting the quantification of centerburst weighting with respect to maximum OPD and spectral broadening width. This analysis serves as a basis for the subsequent derivation of a numerical method for estimating centerburst weighting for practical FTIR measurements. The derivation utilizes true calibrated absorbance spectra for specific species, as opposed to a single, arbitrarily broadened spectral line. Again, the resulting absorbance spectrum from the Fourier transform of an interferogram generated as absorbance evolves linearly is calculated. The resulting spectrum is compared to the centerburst/maximum OPD spectra to determine centerburst weighting for each species.

4.2.1 Uniformly Broadened Spectral Absorbance Line

To provide an analytical illustration of centerburst weighting in Fourier transforms of interferograms of non-stationary spectral components, the Fourier transform of a simple, uniform spectrum with linearly evolving power with respect to OPD is derived. An illustration of this spectrum and its intensity profile is provided in Figure 4-3.

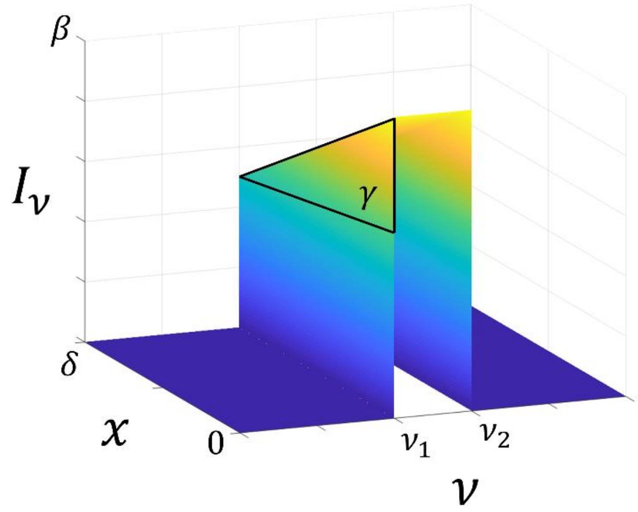

Figure 4-3: A uniformly broadened spectral line with linearly diminishing amplitude with respect to OPD.

Intensity (I) of the broadened spectral line takes on a value of β at the centerburst location (0). It evolves with a slope of γ with respect to OPD (x), whose maximum value is δ. Since only the region containing the broadened spectral line is of interest, intensities outside this region are assigned a value of zero to simplify analysis. The interferogram that this transient, broadened spectral line would produce within an interferometer can be expressed as an inverse Fourier transform of the spectrum, given in Equation 4-1. By neglecting phase errors within the interferogram, which are usually corrected for in commercial FTIRs [100], the inverse Fourier transform becomes equivalent to the inverse cosine transform.

$$I(x) = (\beta + \gamma x) \int_{-\infty}^{\infty} \Pi_{\nu_1,\nu_2}(\nu) \cos(2\pi \nu x) d\nu = (\beta + \gamma x) \frac{\sin(2\pi\nu_2 x) - \sin(2\pi\nu_1 x)}{2\pi x} \qquad (4\text{-}1)$$

Π is the square function, which has a value of 1 when the wavenumber (ν) is between the two subscripted values and is zero otherwise.

Fundamentally, the Fourier transform is only valid for an interferogram generated from a spectrum with stationary power (constant I_ν throughout a scan). This fact is intuitive, since the Fourier transform returns a single, time-invariant spectrum. While the Fourier transform can still be applied to interferograms generated from non-stationary spectrums, the calculated spectrum will be heavily influenced by profile of the spectral power with respect to OPD. Consider the Fourier transform of the non-stationary interferogram given in Equation 4-1.

$$\hat{I}_\nu(\nu) = 2\int_0^\infty (\beta + \gamma x)\ \frac{\sin(2\pi\nu_2 x) - \sin(2\pi\nu_1 x)}{2\pi x} \cos(2\pi\nu x)dx \tag{4-2}$$

Here, the hat (^) symbol refers to the fact that this is a calculated/estimated spectrum, as the true spectrum is time-varying. It is well known that the Fourier transform of the product of two functions is the convolution of the Fourier transform of each function. Thus, the calculated spectrum can be simplified further.

$$\hat{I}_\nu(\nu) = 2\int_0^\infty (\beta + \gamma x)\cos(2\pi\nu x)dx \ * \ 2\int_0^\infty \frac{\sin(2\pi\nu_2 x) - \sin(2\pi\nu_1 x)}{2\pi x} \cos(2\pi\nu x)dx \tag{4-3}$$

The right side term is recognized as the Fourier transform of an interferogram generated from a stationary unit square, and is therefore simply the unit square function. For a FTIR measurement, only a finite maximum OPD can be achieved. Therefore, the upper limit of the integral on the left side of Equation 4-3 is δ for a truncated interferogram. Furthermore, commercial FTIRs multiply the interferogram by an apodization function to mitigate spectral artifacts that emerge due to truncation. Apodization turns out to contribute significantly to the centerburst weighting effect, and is therefore included in this analysis. The triangular apodization function $(1 - \frac{x}{\delta})$ is employed due to its abundance in the literature and similarity to more complicated functions that are used in commercial FTIRs, such as the Norton-Beer functions. It should be noted that centerburst weighting is still prevalent in the absence of an apodization function. The calculated spectrum from an FTIR interferogram generated by the broadened line in Figure 4-3 is given in Equation 4-4.

$$\begin{aligned}
\hat{I}_\nu(\nu) &= 2\int_0^\delta (\beta + \gamma x)\ (1 - \frac{x}{\delta}) \cos(2\pi\nu x)dx \ * \ \Pi_{\nu_1,\nu_2}(\nu) \\
&= \left[\frac{(\beta - \gamma\delta) - (\beta + \gamma\delta)\cos(2\pi\nu\delta)}{\delta\pi^2\nu^2} + \frac{\gamma\sin(2\pi\nu\delta)}{\delta\pi^3\nu^3}\right] \ * \ \Pi_{\nu_1,\nu_2}(\nu) \\
&= \int_{\nu-\nu_2}^{\nu-\nu_1} \frac{(\beta - \gamma\delta) - (\beta + \gamma\delta)\cos(2\pi\nu'\delta)}{\delta\pi^2\nu'^2} + \frac{\gamma\sin(2\pi\nu'\delta)}{\delta\pi^3\nu'^3}\ d\nu'
\end{aligned} \tag{4-4}$$

The final equation for the Fourier transform of the non-stationary spectrum given in Figure 4-3 is obtained by evaluating the convolution in Equation 4-4.

$$\hat{I}_{\nu}(\nu) = \frac{\beta}{\pi}\left[Si\big(2\pi\delta(\nu-\nu_1)\big) - Si\big(2\pi\delta(\nu-\nu_2)\big)\right] + \frac{\beta}{2\pi^2\delta}\left[\frac{cos\big(2\pi\delta(\nu-\nu_1)\big)}{\nu-\nu_1} - \frac{cos\big(2\pi\delta(\nu-\nu_2)\big)}{\nu-\nu_2}\right]$$

$$+ \frac{\gamma\delta-\beta}{2\pi^2\delta}\left[\frac{1}{\nu-\nu_1} - \frac{1}{\nu-\nu_2}\right] + \frac{\gamma}{4\pi^3\delta}\left[\frac{sin(2\pi\delta(\nu-\nu_2))}{(\nu-\nu_2)^2} - \frac{sin(2\pi\delta(\nu-\nu_1))}{(\nu-\nu_1)^2}\right] \tag{4-5}$$

Here, Si represents the sine integral. While complicated, this equation offers some interesting insight into the effects of Fourier transforming a truncated, non-stationary interferogram. For example, it is well-known that truncation leads to "ringing", which are mild, artificial oscillations that emerge outside of the absorption region. Ringing is responsible for the sine and cosine terms in Equation 4-5. Furthermore, this equation demonstrates that for an infinite scan length (δ=∞) and a stationary spectrum (γ=0), the true spectrum at the centerburst is returned. This is expected, since infinite scan length and stationarity result in a fundamentally sound Fourier transform. However, the equation also shows that as scan length becomes finite and decreases, the power returned by the Fourier transform diminishes. Thus, the spectral power calculated from a FTIR is lower than the true spectral power of the infrared beam. The most important piece of insight from Equation 4-5 with regards to non-stationarity is that as broadening increases, the calculated spectrum is more heavily weighted by the centerburst spectrum than the spectrum at the conclusion of the scan. This is because as the spectral line broadens, the leading term becomes dominant and the impact of the final three terms – which contain the broadening width in their denominators – diminishes. This leading term contains the spectral power at the centerburst (β), but contains no information on the transient profile of the true spectral power (γ).

4.2.1.1 Simulations

To illustrate the effects of truncation and non-stationarity on the spectrum calculated for a Fourier transform, interferograms from uniformly broadened, linearly evolving spectral lines are simulated and their resulting Fourier transforms are calculated using Equation 4-5. The parameters within Equation 4-5 are selected to resemble true FTIR spectra. Simulations are performed for three different spectral widths (ν_2-ν_1): 0.5, 1 and 2 cm^{-1}. The center of the spectral region is selected to be 950 cm^{-1}, as this is the center analysis region for acetylene in the composition algorithm of the FTIR utilized in this study. The maximum OPD for the FTIR in this work is 2 cm. Thus, this value is assigned to δ. Finally, the spectral power profile with respect to OPD is formulated so that the power within the spectral region has a value of 0.5 at the centerburst, and reaches a value of 1 at the conclusion of the scan. This results in β and γ being 0.5 and 0.25 cm^{-1}, respectively. To compare the non-stationary and stationary cases and illustrate the effects of centerburst weighting, truncated Fourier transforms of stationary spectra with powers of to β and β+ $\gamma\delta$ (which are equal to the powers at the centerburst and maximum OPD positions for the transient case, respectively) are also calculated. These are represented by $\hat{I}_{\nu,0}$ and $\hat{I}_{\nu,\delta}$ and are given in Equations 4-6 and 4-7, respectively. Throughout the remainder of this sub-section, the calculated spectral power for the non-stationary case will be referred to as $\hat{I}_{\nu,trans}$.

$$\hat{I}_{\nu,0}(\nu) = 2\beta \int_0^{\delta} \frac{\sin(2\pi\nu_2 x) - \sin(2\pi\nu_1 x)}{2\pi x} \cos(2\pi\nu x)dx \tag{4-6}$$

$$\hat{I}_{\nu,\delta}(\nu) = 2(\beta + \gamma\delta) \int_0^{\delta} \frac{\sin(2\pi\nu_2 x) - \sin(2\pi\nu_1 x)}{2\pi x} \cos(2\pi\nu x)dx \tag{4-7}$$

The calculated spectra for each case are shown in Figure 4-4.

The insights from Equation 4-5 are apparent in the figure. A truncated maximum OPD of 2 cm results in calculated powers of roughly 95% and 50% of the true values at 950 cm^{-1} for the stationary cases for spectral widths of 2 and 0.5 cm^{-1}, respectively. These relative reductions in power apply to both $\hat{I}_{\nu,0}$ and $\hat{I}_{\nu,\delta}$. For the narrow spectral width case, the calculated power is reduced substantially, demonstrating that truncation inhibits the detection of narrow spectral peaks. The calculated spectra for the non-stationary cases resemble that of $\hat{I}_{\nu,0}$, especially for the broader spectra. For the widest spectral width case (2 cm^{-1}), the calculated power at 950 cm^{-1} for

$\hat{I}_{\nu,trans}$ is 0.5. Comparing this value to the calculated power for $\hat{I}_{\nu,0}$ (0.475) and $\hat{I}_{\nu,\delta}$ (0.95) illustrates that the calculated spectrum for non-stationary cases is more significantly influenced by its power at/near the beginning of a scan. The calculated power at 950 cm^{-1} for $\hat{I}_{\nu,trans}$ only reaches approximately 5% of the difference between the $\hat{I}_{\nu,0}$ and $\hat{I}_{\nu,\delta}$ at this spectral position, indicating a 95% centerburst weighting. For the 0.5 cm^{-1} case, the centerburst weighting is milder with a value of approximately 68%. Nevertheless, centerburst weighting is present for each profile and in no case is the calculated spectra equal to the average power (considering the effects of truncation) during a scan as is often implicitly assumed in analysis of FTIR measurements.

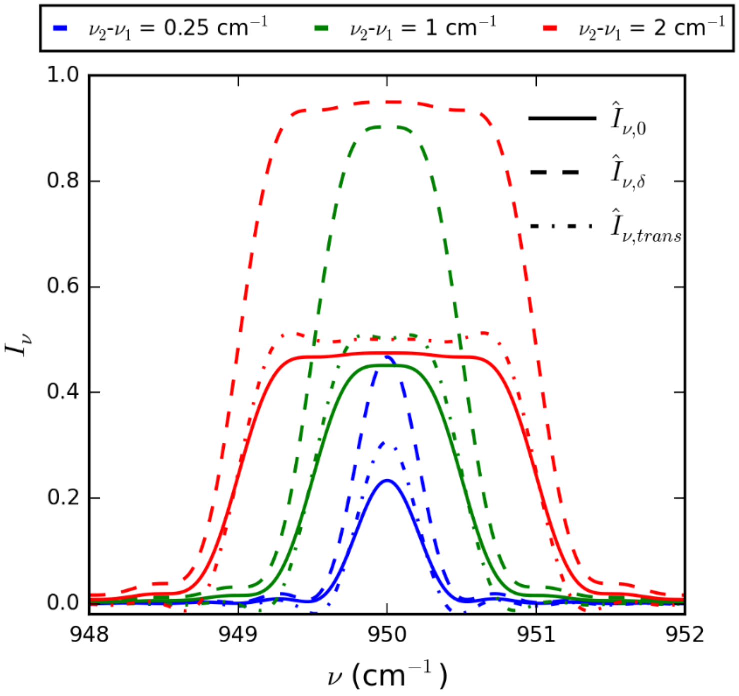

Figure 4-4: An illustration of centerburst weighting using simulated uniformly broadened spectral lines of varying widths with linearly diminishing amplitudes. Calculated spectral intensity from the truncated, apodized Fourier transform for the linearly diminishing cases ($\hat{I}_{\nu,trans}$) more closely resemble the calculated spectra at the centerburst ($\hat{I}_{\nu,0}$) than that at maximum OPD ($\hat{I}_{\nu,\delta}$), especially for highly broadened spectra. For the results above, δ = 2 cm, β = 0.5 and γ = 0.25 cm^{-1}.

The analysis presented in this sub-section contains important implications for the interpretation of FTIR spectra from engine exhaust measurements during transients. First, it provides a mathematical explanation for the bias observed in the FTIR measurements of transient quantities of acetylene and propylene and demonstrates how standard mapping techniques, which assume a stationary signal and a quasi-steady gas cell composition, can produce erroneous emissions profiles. On a positive side, these results also imply that if the absorbance/composition transients follow an approximately linear profile with respect to OPD (or some other known transient profile), then the effect of centerburst weighting can ultimately be taken into account to deduce the true spectrum (and therefore true composition) from biased FTIR measurements. Thus, the effects of centerburst weighting can be incorporated into the measurement model in the UKF, which relates a measured value to a corresponding state value (which is the gas cell species composition in our case). This technique is built upon the idea that the true composition profile follows a linear trend more closely than a stationary, or zero-order trend. Furthermore, no additional error is introduced if a measurement is indeed stationary case, since the spectral intensity slope with respect to OPD becomes zero and the Fourier transform is reduced to its fundamental form. However, Equation 4-5 also indicates that the degree of centerburst weighting is unique to a spectrum, as greater broadening results in greater centerburst weighting. The shapes of absorption spectra vary considerably between species and even between spectral regions for a single species. Furthermore, spectral lines broaden in a Lorentzian profile, not uniformly. Thus, the ability of Equation 4-5 to predict the contributions of centerburst weighting in FTIR measurements is limited. This issue is addressed in the following sub-section with the derivation of a new equation which estimates the magnitude of centerburst weighting for true FTIR measurements of a species using calibrated absorbance spectra for known, stationary compositions.

4.2.2 Calibrated Absorbance Spectra

To determine how centerburst weighting impacts the measurements of absorbance spectra – and therefore species composition – in FTIR spectroscopy, a similar analysis to that of the previous section is performed. However, the centerburst weighting for linearly evolving absorbance values are calculated for actual calibration spectra from absorbing species, as opposed to an arbitrary, uniformly broadened spectrum. In FTIR spectroscopy, calibrations are conducted to map measured spectral intensity within a specific absorbed spectral region – referred to as the analysis region – to composition of a species of interest. These calibrations are performed by introducing a sample with known composition into the FTIR gas cell and measuring the corresponding intensity/absorbance within the analysis region. A key difference between this and the previous analysis is that the true spectrum is unknown, since calibrations are altered by the effects of truncation and apodization. Consider the equation for the calibrated spectral intensity within a spectral analysis region $\hat{I}_{\nu,cal}$ as it relates to the true interferogram for a particular apodization D and composition, given in Equation 4-8.

$$\hat{I}_{\nu,cal}(\nu) \; = \; 2\int_0^{\delta} I(x)D(x)\cos(2\pi\nu x)dx \tag{4-8}$$

Now consider the case where the composition at the centerburst position of a FTIR scan is equal to the composition used in the calibration in Equation 4-8. However, the spectral intensity evolves linearly with a relative slope of γ with respect to OPD (due to changing concentration of the absorbing species within the gas cell). The spectral intensity that would be measured for this case is given in Equation 4-9.

$$\hat{I}_{\nu}(\nu) \; = \; 2\int_0^{\delta}(1+\gamma x)I(x)D(x)\cos(2\pi\nu x)dx \tag{4-9}$$

Strictly speaking, the interferogram $I(x)$ in the formula above refers only to the contribution of the spectral analysis region to the interferogram, since that is the only portion that is linearly evolving. However, due to the linearity of the Fourier transform, this analysis still stands for a general interferogram. Intensity from other spectral regions should only contribute to measured spectral intensity within those regions, aside from the contributions of ringing which are neglected in this analysis. Also, Equation 4-9 assumes that each spectral component evolves with the same slope γ.

To deduce how the spectral intensity transient alters the final measured spectral intensity, it is advantageous to present Equation 4-9 in terms of the original calibration spectrum. This is accomplished by rewriting the equation as the convolution of the transient profile with the original interferogram and apodization function. The latter term in this convolution is the original calibration spectrum.

$$\begin{aligned}\hat{I}_{\nu}(\nu) &= 2\int_{0}^{\delta}(1+\gamma x)\cos(2\pi\nu x)dx \;*\; 2\int_{0}^{\delta} I(x)D(x)\cos(2\pi\nu x)dx \\ &= 2\int_{0}^{\delta}(1+\gamma x)\cos(2\pi\nu x)dx \;*\; \hat{I}_{\nu,cal}(\nu) \qquad (4\text{-}10)\end{aligned}$$

The preceding term can be evaluated analytically, leading to the final equation for measured spectral intensity for a linearly evolving spectrum in terms of a calibration spectrum.

$$\hat{I}_{\nu}(\nu) = \frac{1}{\pi\nu}\left((1+\gamma\delta)\cos(2\pi\nu\delta) + \frac{\gamma sin(\pi\nu\delta)^2}{\pi\nu}\right) * \hat{I}_{\nu,cal}(\nu)$$

$$= \int_{-\infty}^{\infty}\frac{1}{\pi(\nu-\nu\prime)}\left((1+\gamma\delta)\cos(2\pi(\nu-\nu')\delta) + \frac{\gamma sin(\pi(\nu-\nu\prime)\delta)^2}{\pi(\nu-\nu\prime)}\right)\hat{I}_{\nu,cal}(\nu')d\nu' \qquad (4\text{-}11)$$

Before the above equation can be utilized to determine the degree of centerburst weighting for the FTIR measurement of a specific species, some caveats associated with FTIR spectroscopy must first be taken into account.

First, since FTIR absorption/intensity is nearly impossible to describe analytically, Equation 4-11 must be evaluated numerically. Second, species mole fraction X only indirectly impacts spectral intensity through its direct relationship with absorbance (A_{ν}) via the Beer-Lambert law.

$$A_{\nu}(\nu) = log\left(\frac{I_{\nu,base}}{I_{\nu}}\right) = \alpha_{eff}X \qquad (4\text{-}12)$$

Here, α_{eff} is an effective absorptivity that accounts for the pathlength of the IR beam and the volume of the gas cell. Since the baseline spectral intensity $I_{\nu,base}$ varies between FTIRs and may even change within a short timeframe for a single instrument due to degradation, calibrations are performed in terms of absorbance. Thus, to make this analysis generally applicable, Equation 4-11 is transformed to absorbance space.

$$\hat{A}_\nu = \int_{-\infty}^{\infty} \frac{1}{\pi(\nu-\nu\prime)} \left((1+\gamma_A\delta)\cos(2\pi(\nu-\nu')\delta) + \frac{\gamma_A sin(\pi(\nu-\nu\prime)\delta)^2}{\pi(\nu-\nu\prime)} \right) \hat{A}_{\nu,cal}(\nu')d\nu' \qquad (4\text{-}13)$$

Here, γ_A refers to the slope of spectral absorbance with respect to OPD, which replaces spectral intensity slope of Equation 4-11. It should be mentioned that fundamentally, this transformation is only valid if the relationship between A_ν and I_ν is linear and the base intensity $I_{\nu,\text{base}}$ is uniform. However, at small levels and moderate changes of absorbance, the relationship between A_ν and I_ν can be reasonably approximated as linear. Also, base intensity is usually relatively uniform within typical spectral widths of analysis regions (~100 cm^{-1}).

A value for the slope of the spectral absorbance (γ_A) must be selected for each species to apply Equation 4-13. In this analysis, γ_A is selected so that the absorption spectrum at the conclusion of the scan ($x = \delta$) is equal to that of a second calibration $A_{\nu,cal,2}$. This is accomplished with the following equation for γ_A.

$$\gamma_A = \frac{\hat{A}_{\nu,cal,2}(\nu) - \hat{A}_{\nu,cal,1}(\nu)}{\hat{A}_{\nu,cal,1}(\nu)\delta} \qquad (4\text{-}14)$$

It should be noted that although the absorbance calibrations are vectors, γ_A is assumed to be a scalar. Said differently, it is assumed that the absorbance at each spectral position evolves with the same relative slope. This is a reasonable assumption, since absorptivity is relatively constant with respect to absorbance, especially for moderate changes in absorbance. However, slight differences between different spectral positions exist, and a weighted average at each spectral position is used to calculate γ_A. It should also be noted that although Equation 4-14 uses the calibration spectra - which are effected by apodization and truncation – to estimate the slope of the true absorbance evolution, the resulting value will still be accurate and represent the true slope as long as γ_A is indeed a scalar. Proof of this postulation is provided in the Appendix under *4.2.2 - Proof of Validity of Absorbance Evolution Slope Calculation of Equation 4-14.*

To finally estimate the magnitude of centerburst weighting on FTIR measurements of a given species during a linearly evolving case, Equation 4-13 is applied to simulate the measured spectrum. This spectrum is fed to the algorithm within the FTIR software to calculate a corresponding composition, denoted as $\hat{X}_{cal,transient}$. The algorithm within the FTIR software is a modified version of Classical Least Squares, which selects the composition that achieves the minimal level of spectral errors with respect to calibrations. $\hat{X}_{cal,transient}$ is compared to the compositions at the centerburst and maximum OPD positions ($\hat{X}_{cal,1}$ and $\hat{X}_{cal,2}$), which correspond to calibrated spectra $\hat{A}_{v,cal,1}$ and $\hat{A}_{v,cal,2}$. The magnitude of centerburst weighting c_w is given in Equation 4-15.

$$c_w = \frac{\hat{X}_{cal,2} - \hat{X}_{cal,transient}}{\hat{X}_{cal,2} - \hat{X}_{cal,1}} \tag{4-15}$$

Centerburst weighting varies between values of 0.5 and 1. For the former value, the calculated spectrum is equally influenced by the centerburst and maximum OPD spectra, and therefore yields a composition value directly in between the two calibrations. The latter value corresponds to a case where the calculated transient spectrum closely resembles the initial calibration spectrum $\hat{A}_{v,cal,1}$, and is minimally influenced by the true spectral profile with respect to OPD. An illustration for the process for determining the degree of centerburst weighting for each species is provided in Figure 4-5.

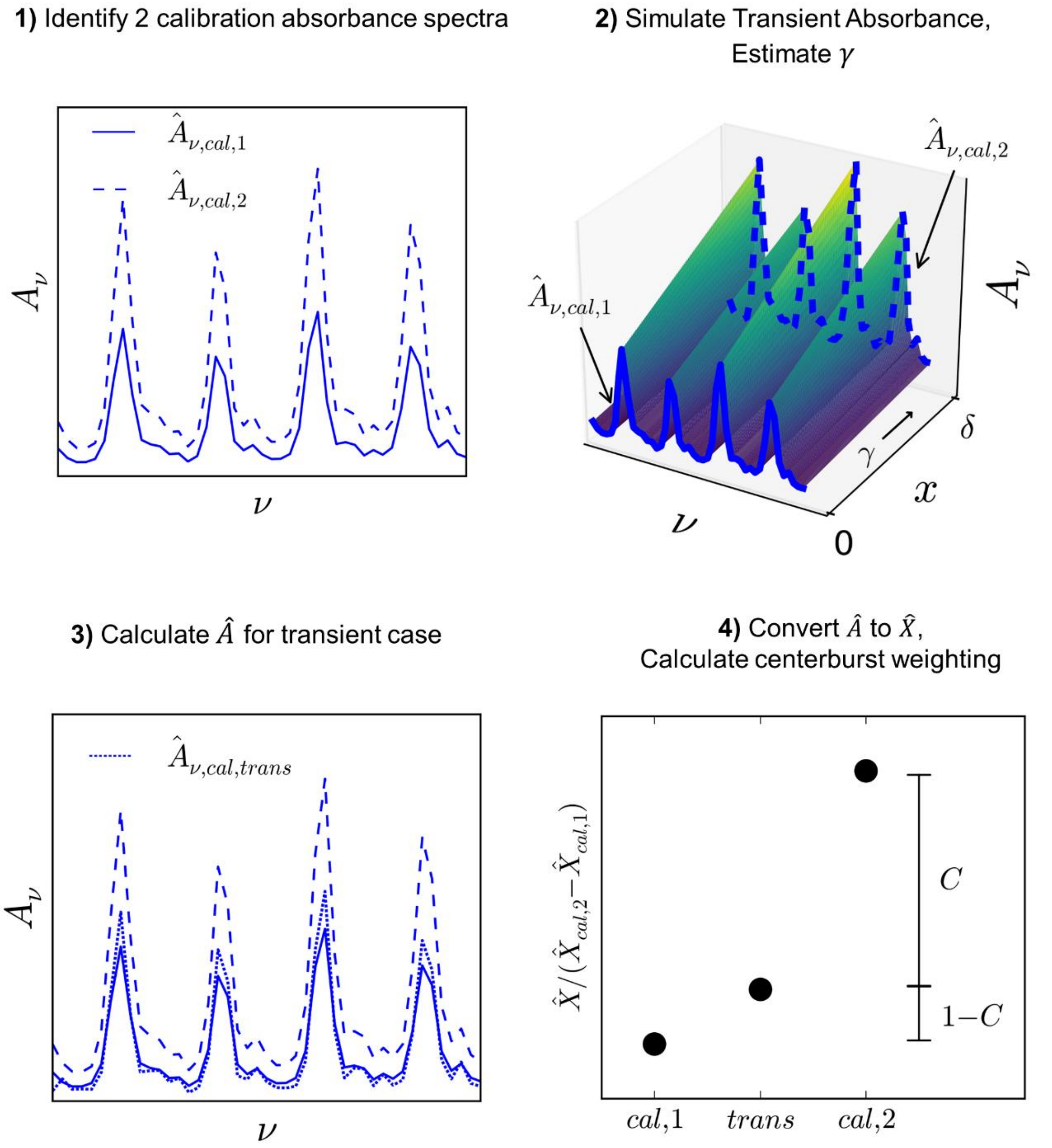

Figure 4-5: An illustration of the process for determining the degree of centerburst weighting in FTIR measurements for a given species. 1) Identify two calibration absorbance spectra that correspond to known compositions. 2) Simulate the measurement of a linearly evolving absorbance spectrum that begins as spectrum 1 at the centerburst, and ends as spectrum 2 at the conclusion of a scan. Estimate the slope of absorbance evolution with respect to OPD. 3) Apply numerical convolution (Equation 4-13) to calculate the estimated spectrum according to the Fourier transform for the transient case in step 2. 4) Convert the transient spectrum to a corresponding composition. Compare the transient composition to that of the calibration spectra to determine centerburst weighting c_w.

The process illustrated in Figure 4-5 is performed to determine the degree of centerburst weighting for each engine exhaust component within the gasoline/ethanol FTIR recipe used in this work. This recipe is used within the modified Classical Least Squares algorithm to estimate compositions from the measured spectra. Centerburst weights for each species are listed in Table 4-1. The degree of centerburst weighting varies substantially between species, with some species displaying complete centerburst weighting (cyclohexane, ethanol and isopentane) and nitrogen oxide displaying equal weighting between composition at the centerburst and maximum OPD. However, it should be noted that fundamentally, a centerburst weighting of 0.5 should only be achieved for an infinitesimally narrow absorption region. While the absorption peaks of N_2O are indeed relatively thin, the lower-than-expected value for centerburst weighting is likely due to the fact that absorptivity for N_2O decreases as absorbance increases. Thus, for a case where composition increases linearly with respect to OPD during a FTIR scan, the slope of the absorbance spectrum decreases as the scan progresses. This contradicts the assumption in the formulation of Equation 4-13 that the evolution of the absorbance spectrum is linear, and leads to an overprediction of measured absorbance (and an underprediction of centerburst weighting). Future work in this area should address the effects of absorbance non-linearity displayed by some narrow absorbing species.

Species	Centerburst Weight
1,3 butadiene (C_4H_6)	0.99
Acetaldehyde (C_2H_4O)	0.98
Acetylene (C_2H_2)	0.74
Ammonia (NH_3) - Cal 1	0.89
Ammonia (NH_3) - Cal 2	0.75
Benzene (C_6H_6)	0.97
Carbon Monoxide (CO)	0.73
Carbon Dioxide (CO_2)	0.71
Cyclohexane (C_6H_{12})	1.00
Ethane (C_2H_6)	0.73
Ethanol (C_2H_5OH)	1.00
Ethylene (C_2H_4)	0.90
Formaldehyde (CH_2O)	0.83
Water (H_2O)	0.70
Isobutylene (C_4H_8)	0.97
Isopentane (C_5H_{12})	1.00
Methane (CH_4)	0.81
Methanol (CH_3OH)	0.88
MTBE ($C_5H_{12}O$)	0.98
Nitric Oxide (NO)	0.68
Nitrogen Dioxide (NO_2)	0.59
Nitrogen Oxide (N_2O)	0.50
Pentane (C_5H_{12})	0.98
Propylene (C_3H_6)	0.92
Toluene (C_7H_8)	0.97

Table 4-1: List of calculated centerburst weights for each species within the gasoline/ethanol FTIR recipe used in this work.

As suggested by the analysis performed in Section 4.2.1, the degree of centerburst weighting appears correlated to the magnitude of spectral broadening within an absorbed region. To illustrate this point, Figure 4-6 displays the two stationary calibration spectra $\hat{A}_{v,cal,1}$ and $\hat{A}_{v,cal,2}$, as well as the calculated spectrum for the linearly evolving case $\hat{A}_{v,transient}$ for acetylene and propylene, which have centerburst weighting values of 0.74 and 0.92, respectively.

The analysis spectra of acetylene contain numerous narrow peaks with widths less than 1 cm^{-1}. Conversely, the spectra of propylene are characterized by approximately uniform absorbance spanning roughly 60 cm^{-1}, with relatively narrow absorbance peaks on the ends of this uniform region. For acetylene, the peak values of the narrow absorbing regions within $\hat{A}_{\nu,transient}$ reach nearly halfway between the corresponding peaks for $\hat{A}_{\nu,cal,1}$ and $\hat{A}_{\nu,cal,2}$. This supports the idea centerburst weighting is less pronounced for narrow peaks, and explains the moderate value calculated for acetylene. Conversely, $\hat{A}_{\nu,transient}$ for propylene closely resembles $\hat{A}_{\nu,cal,1}$, especially in the broad, uniform absorbance regions. In fact, the differences between the two spectra are practically imperceptible aside from the two peaks near 910 and 990 cm^{-1}, where the maximum values are slightly greater for $\hat{A}_{\nu,transient}$ as expected. Thus, propylene measurements contain significant centerburst weighting due to its predominantly broad absorption spectrum. If not for the two relatively narrow absorbance peaks near 910 and 990 cm^{-1}, the value for centerburst weighting would likely be very close to 1. The fact that the two relatively narrow absorption peaks display less centerburst weighting than the remainder of propylene spectrum provides further support to the idea that centerburst weighting scales with broadening. These results also corroborate the experimental differences in periodic bias observed in the measured acetylene and propylene compositions in Figure 4-1. Propylene displays significantly greater centerburst weighting, as indicated by the minuscule measurement changes that occur every other period. This is supported by its higher centerburst weighting calculation relative to acetylene.

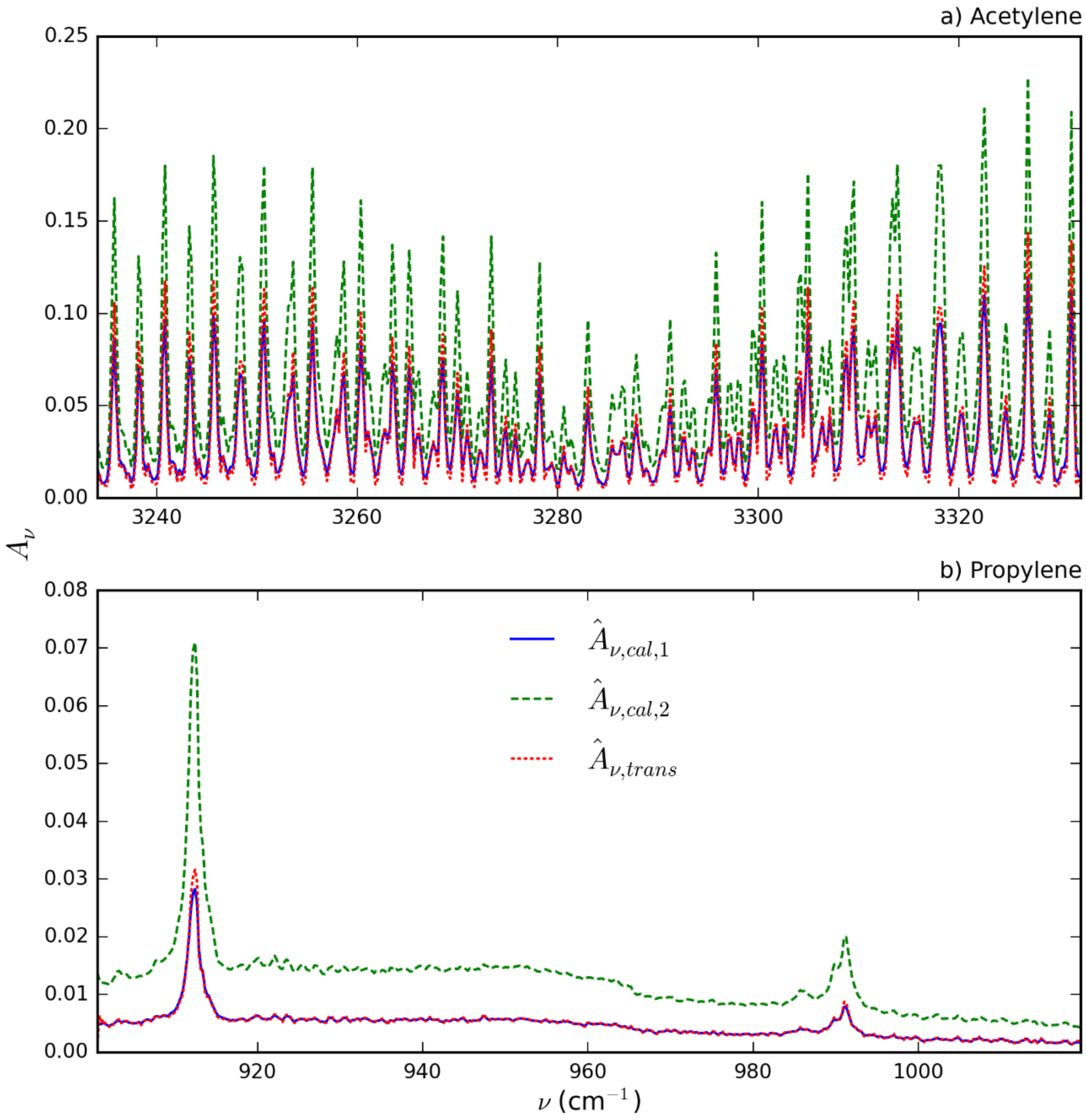

Figure 4-6: The calibration and calculated transient absorbance spectra used to determine the centerburst weighting (c_w) for acetylene and propylene. As predicted by Equation 4-5 and demonstrated in Figure 4-4, broad absorbance peaks are subject to greater centerburst weighting during transients (propylene), while narrow absorbance peaks are more heavily influenced by the absorbance history during a scan (acetylene).

Information about the degree of centerburst weighting for each species can be used to create a more accurate measurement model within the UKF. The measurement model, which describes the relationship between measurements and system states, estimates the composition within a FTIR gas cell from a measured value. Since FTIR measurements are biased during transients due to non-stationarity, the measurement model must be updated to account for this bias to accurately deduce the gas cell composition. The following section is devoted to introducing these modifications to the UKF.

4.3 Modified UKF Sub-models

To account for the effects of centerburst weighting in FTIR measurements of sample with transient composition, the UKF state transition and measurement models are updated. As proven extensively in the previous subsection, a FTIR measurement is a function of how the composition evolves during a mirror scan. Assuming that the profile of absorbance/composition evolution with respect to OPD is linear, a FTIR measurement of a given species can be described as a function of the composition values at the centerburst and maximum OPD mirror positions. This is analogous to $\hat{X}_{cal,transient}$ from the previous subsection being a function of the initial and final calibration compositions ($\hat{X}_{cal,1}$ and $\hat{X}_{cal,2}$), which are present at the centerburst and maximum OPD, respectively. As shown previously, this function is determined by the magnitude of centerburst weighting.

Assuming that measurements are reported at the conclusion of a scan, and that the subsequent scan begins immediately afterward, then the compositions at the beginning and end of a scan correspond to the previous and current measurement times, respectively. In an analogy using the composition values from the analysis in the previous subsection, the gas cell has a composition of $\hat{X}_{cal,1}$ at time $t - 1$ (at the end of the previous scan/beginning of current scan), and a composition of $\hat{X}_{cal,2}$ at time t (at the end of the current scan). Thus, the UKF state transition model is modified to include the previous inlet and total gas cell compositions (at $t - 1$), and the measurement model is modified to include weighting from the previous composition.

4.3.1 State Transition Model

The modified state transition model is identical to that of Chapter 3 aside from the additions of inlet and gas cell composition at the previous time ($\hat{\boldsymbol{Z}}_{in,t-1}$ and $\hat{\boldsymbol{Z}}_{cell,t-1}$, respectively). Current inlet composition $\hat{\boldsymbol{Z}}_{in}$ remains modelled as steady, and gas cell composition remains described using the quasi-steady, well-mixed model. $\hat{\boldsymbol{Z}}_{in,t-1}$ and $\hat{\boldsymbol{Z}}_{cell,t-1}$ are simply modelled using the previous values of inlet and total gas cell composition ($\hat{\boldsymbol{Z}}_{in}(t-1)$ and $\hat{\boldsymbol{Z}}_{cell}(t-1)$), respectively, since the two quantities are identical by definition. $\hat{\boldsymbol{Z}}_{cell,t-1}$ is included within the UKF models since, as shown previously, current FTIR measurements can be described as functions of the composition at both the previous and current times. $\hat{\boldsymbol{Z}}_{in,t-1}$ is also included, as it serves as an updated estimate for previous inlet composition that is more accurate than $\hat{\boldsymbol{Z}}_{in}(t-1)$ since it can be informed from both the previous and current measurements. Using $\hat{\boldsymbol{Z}}_{in,t-1}$ to describe the emissions profile is especially important for species with substantial centerburst weighting during forward scans, since such measurements are largely weighted by previous composition values. Thus, estimations of $\hat{\boldsymbol{Z}}_{in}(t)$ (and $\hat{\boldsymbol{Z}}_{cell}(t)$) during a forward scan will have low confidence (high variance) by themselves. However, the additional update during the subsequent backward scan provides additional information about these states, reducing uncertainty. The entire state transition model is given in Equation 4-16.

$$\hat{\boldsymbol{x}}(t|t-1) = \begin{bmatrix} \hat{\boldsymbol{Z}}_{in}(t|t-1) \\ \hat{\boldsymbol{Z}}_{in,t-1}(t|t-1) \\ \hat{\boldsymbol{Z}}_{cell}(t|t-1) \\ \hat{\boldsymbol{Z}}_{cell,t-1}(t|t-1) \\ \hat{m}(t|t-1) \end{bmatrix} = \begin{bmatrix} \hat{\boldsymbol{Z}}_{in}(t-1|t-1) \\ \hat{\boldsymbol{Z}}_{in}(t-1|t-1) \\ \hat{\boldsymbol{Z}}_{in}(t-1|t-1)\left(1-e^{-\frac{\Delta t}{\hat{\tau}(t-1|t-1)}}\right) + \hat{\boldsymbol{Z}}_{cell}(t-1|t-1)e^{-\frac{\Delta t}{\hat{\tau}(t-1|t-1)}} \\ \hat{\boldsymbol{Z}}_{cell}(t-1|t-1) \\ \hat{m}(t-1|t-1) \end{bmatrix} \quad (4\text{-}16)$$

At first glance, it may appear that $\hat{\boldsymbol{Z}}_{in,t-1}$ is unrelated to current or previous gas cell composition within the state transition model, and therefore may not be updated properly according to measurement changes. However, the reader should be reminded that the UKF also calculates covariances between variables. Since $\hat{\boldsymbol{Z}}_{in,t-1}$ and $\hat{\boldsymbol{Z}}_{cell,t-1}$ are highly correlated, $\hat{\boldsymbol{Z}}_{in,t-1}$ is indeed updated according to updates in $\hat{\boldsymbol{Z}}_{cell,t-1}$, which are informed by both the current and previous FTIR measurements.

4.3.2 Measurement Model

The measurement model within the UKF is updated to account for the effects of non-stationarity/centerburst weighting. In the modified measurement model, FTIR composition measurements are described as a function of $\hat{\boldsymbol{Z}}_{cell,t-1}$ and $\hat{\boldsymbol{Z}}_{cell}$ and the centerburst weighting value for a given species provided in Table 4-1. Since the relative time throughout a scan at which the moving mirror arrives at the centerburst position depends on scan direction, different measurement models are applied to forward and backward scans. For a forward scan, the centerburst position is the initial position, and occurs approximately at the previous measurement time. Thus, the centerburst weighting $\boldsymbol{c}$ is applied to $\hat{\boldsymbol{Z}}_{cell,t-1}$, and the remaining weight to $\hat{\boldsymbol{Z}}_{cell}$. Conversely, the centerburst position is reached at the end of a scan – when the current measurement is reported – for a backward scan. Thus, the centerburst weighting is applied to the current composition $\hat{\boldsymbol{Z}}_{cell}$ for a backward scan. The measurement model for mass flow rate remains the same as in Chapter 3. The collective modified measurement models are shown in Equation 4-17.

$$\hat{\boldsymbol{y}}(t|t-1) = \begin{bmatrix} \begin{cases} \left[\boldsymbol{c}_w \cdot \boldsymbol{Z}_{cell,t-1}(t|t-1) + (1-\boldsymbol{c}_w) \cdot \boldsymbol{Z}_{cell}(t|t-1)\right] \cdot \frac{MW_{mix}}{\boldsymbol{MW}} & \text{forward scan} \\ \left[(1-\boldsymbol{c}_w) \cdot \boldsymbol{Z}_{cell,t-1}(t|t-1) + \boldsymbol{c}_w \cdot \boldsymbol{Z}_{cell}(t|t-1)\right] \cdot \frac{MW_{mix}}{\boldsymbol{MW}} & \text{backward scan} \end{cases} \\ \dot{m}(t|t-1) \end{bmatrix} \tag{4-17}$$

The updated models above are utilized for the FTIR measurements of tracer hydrocarbons and engine emissions conducted in this work. The remainder of this chapter is dedicated to experimentally validating these updated UKF sub-models to ensure that they yield accurate estimations of inlet composition. It should be noted that scan direction is currently determined empirically, as filtering with the opposite measurement models produces obviously erroneous oscillations in the composition estimations that are easy to detect.

4.4 Experimental Validation

Experimental validation of the modified UKF presented in the previous section is performed by flowing known quantities of tracer gas with different transient profiles through the FTIR. Two tracer gases are selected for experimental validation: acetylene and propylene. These two gases are chosen due to their vastly different absorption spectrums, and therefore different magnitudes of centerburst weighting. As shown in Figure 4-6 acetylene contains numerous narrow absorption peaks which yields a moderate degree of centerburst weighting in its measurements. Conversely, the propylene spectrum contains significant broadening and uniform absorbance over a substantial portion of the spectrum, yielding significant centerburst weighting in propylene measurements. Validating the modified UKF with two gases with centerburst weightings near the upper and lower limit increases the confidence that the UKF can be applied to a wide range of species. These tracer gases are mixed with room air, which is pulled through the FTIR at a set flow rate. Experiments are conducted at sample flow rates of 12 and 25 slpm. The former flow rate is typical for FTIR measurements of engine exhaust in the literature. However, residence times within the FTIR gas cell are shorter at higher flow rates, reducing historical effects and resulting in measurements that more accurately reflect true transient emissions profiles. Experiments are conducted at the higher flow rate to demonstrate this benefit. More information on the specific profiles investigated are presented in section 4.4.2. Values of 100 ppm and 0.25 slpm are used for inlet composition process noise variance ($\Phi_{\boldsymbol{Z}_{in}}$) and mass flow rate process noise variance ($\Phi_{\dot{m}}$) in this analysis. The former is chosen as a middle-ground value that is equally applicable to the significant and modest inlet composition fluctuations explored in this work. Mass flow rate process noise variance is chosen from previous observations. Composition measurement noise variance is approximated by filling the gas cell with approximately 100 ppm of acetylene and propylene and taking continuous measurements over a 3-minute span. The measurement noise variance for each species is approximately 1.5 ppm.

4.4.1 Experimental Setup

Experimental validation of the UKF requires an architecture for controlling tracer flow and a FTIR spectrometer for measuring composition. The FTIR utilized for this study is the MKS 2030-HS. The MKS 2030-HS has a gas cell with a volume of approximately 200 mL and measures at a high frequency of 5 Hz, allowing transient composition profiles to be reasonably captured. However, the extent to which transient profiles can be captured is limited by the factors previously outlined; namely residence time effects and non-stationarity of the intensity of the IR beam. The MKS 2030-HS has a spectral resolution of 0.5 cm^{-1} and an IR pathlength of 5.11 meters. A low spectral resolution allows absorption lines in close proximity to be resolved, while the long pathlength permits low-level detectability. The FTIR is equipped with a silicon carbide radiation source at 1200°C, a liquid nitrogen-cooled mercury cadmium telluride detector, and a helium neon laser for generating a reference interferogram. A temperature of 191ºC is maintained within the FTIR gas cell and the upstream sample line with the aid of a controller. Temperature and pressure within the gas cell are measured and reported at a frequency of 5 Hz.

A diagram of the setup is shown in Figure 4-7. The tracer gases chosen for these experiments are acetylene and propylene. Tracer gas is introduced into the FTIR using MKS GM50A mass flow controllers (MFC) with a 0 to 40 sccm flow range. The flow controllers are accurate to within 1% from 20% to 100% full scale and have a reported settling time of less than 750 ms. Flow rate commands are received by the MFCs from LABVIEW at approximately 50 ms intervals. The MFCs are connected to a manifold, which also draws in room air due to suction from a pump downstream of the FTIR. Tracer gas/air is drawn into the FTIR, where the tracer mole fraction within the FTIR gas cell is measured. Downstream of the FTIR is a valve, which is used to set the flowrate, followed by a MKS GM100A mass flow meter (MFM). The MFM is capable of measuring flow rates from 2 slpm to 100 slpm, with 0.2% accuracy from 2 to 20 slpm, and 1% accuracy from 20 to 100 slpm. Tracer mass fraction of the sample is calculated by dividing the tracer flow rate from the MFCs by the total sample flow rate measured by the MFM. To directly compare estimated FTIR inlet composition from the UKF with the known composition from the MFC/MFM data, the time-lag between the introduction of tracer from the MFCs to the tracer reaching the FTIR must be considered. This time-lag is estimated by dividing total volume of the line between the MFC and FTIR by the volume flow rate, corresponding to time-lags of approximately 0.5 and 0.25 seconds for flow rates of 12 and 25 slpm, respectively.

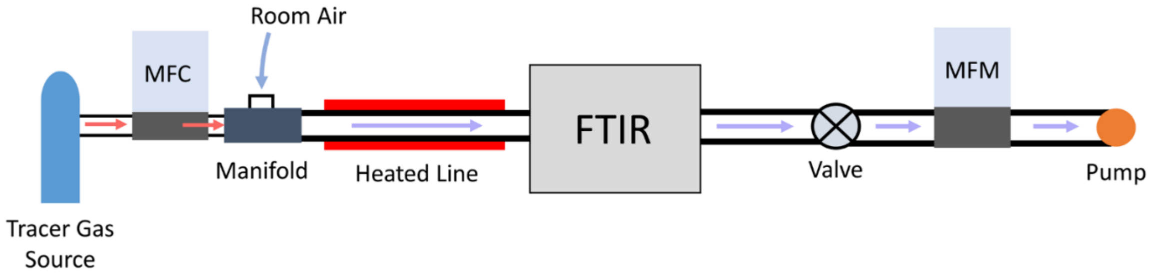

Figure 4-7: Experimental setup for UKF validation.

4.4.2 Results

Presented in this subsection are experimental results for the validation of the modified UKF. Estimated tracer composition from the UKF is compared to the known composition profiles. It is shown that the UKF yields significant improvements over unfiltered FTIR measurements, which are susceptible to residence time and stationarity issues. The UKF is validated over a wide range of transient profiles to ensure its robustness. First, results for wave profiles at frequencies ranging from 0.75 to 1.5 Hz are presented. Different frequencies are investigated to explore the relationship between filter performance and transient duration and to determine the duration limit at which a fluctuation in emissions can be adequately captured. The amplitudes of these waves are varied from 10 to 100 ppm to explore the relationship between filter performance and magnitude of emissions fluctuations, and how measurement noise can mask fluctuations of smaller magnitude. To simulate the irregularities of real-world emissions profiles, experiments are conducted for spline tracer profiles, where the tracer set points are randomly selected from a distribution. The results of these experiments demonstrate the ability of the UKF to predict complicated emissions profiles. To explore the effects of duration and magnitude of emission fluctuations on estimates from the UKF, experiments are conducted for spline profiles with varying scales and time between set points, respectively. More detail on the spline profiles is provided in Section 4.4.2.2. Experiments for each tracer composition profile are conducted at flow rates of 12 and 25 slpm to investigate the effects of flow rate on estimation accuracy.

Although engine emissions profiles in real-world driving scenarios vary considerably according to engine type, fuel and driving cycle, the magnitudes of emissions fluctuations explored in this work resemble those of some engine studies found in the literature. For example, Gierczak et al. measured VOC emissions from a flex-fuel vehicle during a FTP cold start, and found that acetaldehyde, ethanol and formaldehyde emissions varied from 0 to approximately 150, 100 and 10 ppm, respectively [41]. In an investigation of VOC emissions from a gasoline engine operating with different blends of alcohol during the NEDC driving cycle, propylene and ethanol emissions spiked on the order of 100 ppm during the first transient event, while formaldehyde, 1-3 butadiene, benzene and toluene spikes ranged between 30 and 70 ppm [101]. Acetaldehyde and formaldehyde emissions from a 4-stroke gasoline-powered motorcycle regularly fluctuated on the order of 100 ppm during a transient driving cycle in work by Penteado et al. [102]. The durations of emission fluctuations also vary substantially in the literature. For example, measurements of total HC emissions from a GDI engine under the NEDC driving cycle using a fast response chemiluminescence detector showed fluctuations on the order of thousands of ppm with durations ranging from milliseconds to several seconds [103]. The experiments in this work cover an intermediate portion of this duration range, as the lowest duration at which a transient event can be measured is limited by the FTIR measurement frequency, which is 5 Hz. Furthermore, previous analysis demonstrated that inlet composition profiles that fluctuate at frequencies greater than 1.25 Hz are inadequately captured at this measurement frequency, as demonstrated in Chapter 3. This finding guided the selection of the transient profiles explored here.

4.4.2.1 Wave Profiles

Shown in Figures 4-8 and 4-9 are results for wave profiles with frequencies ranging from 0.75 to 1.5 Hz at a sample flow rate of 12 slpm for acetylene and propylene, respectively. Generally, the estimated inlet composition from the UKF follows the true composition more closely than unfiltered FTIR measurements for both species. The unfiltered FTIR measurements fail to capture the extremes and lag the inlet composition profiles due to residence time effects. The UKF, however, leverages measurement changes and state/measurement models to accurately calculate changes in inlet composition. In most cases, better estimations are obtained when the inlet profile has greater amplitudes and lower frequencies. For example, comparing Figures 4-8a, e and i, which correspond to amplitudes of 100, 25 and 10 ppm for the lowest frequency acetylene cases, respectively, it is seen that as amplitude decreases more erroneous estimations appear. Although accurate estimations of amplitude are attained in 6e, there are a few artifacts in the estimated profile, such as the sudden, slight increase in composition near 4.5 s when the true composition is at a trough. At about 4.5 s in Figure 4-8i, the estimated inlet composition increases prematurely as the true composition is still at a trough. These anomalous estimations occur because as amplitude decreases, the magnitude of measurement changes become comparable to that of the measurement noise, masking the true composition profile. Nevertheless, the UKF improves the estimations of inlet composition and provides more accurate estimations of the extremes of the profile, even for some of the 10 ppm cases. It should be noted that the true inlet composition for the smaller amplitudes, especially the 10 ppm cases, appear relatively noisy. This is due to resolution and settling time limitations of the mass flow controllers that prevent accurate control for small set points changes and may contribute to some of the measurement/estimation errors seen for these cases.

As frequency increases beyond 0.75 Hz, the quality of the estimations from the UKF generally deteriorate and the peaks of the inlet composition profile are less accurately estimated. The fact that better estimations are obtained for lower frequencies is partly attributed to the relatively large residence times of sample within the gas cell, which causes the total gas cell composition (or FTIR measurements) to lag the inlet composition. This lagging effect becomes more significant as inlet composition frequency increases, since the total gas cell composition profile has less time to catch up with inlet composition profile before it changes trajectory. This is seen in Figure 4-8d and 4-9d, where the amplitudes of the measurement profiles are significantly less than that of the inlet composition profile for the 100 ppm, 1.5 Hz cases. However, it should be noted that lagging effects are less severe for the modified UKF, since previous inlet composition values are updated by current measurements. The ability to estimate high frequency transients is also limited by the measurement frequency. As the ratio between inlet composition and measurement frequency increases, the magnitude of sampling errors become greater. Nevertheless, the UKF generally yields better estimations of the inlet composition profile than the raw measurements, even for the higher frequency cases.

All other factors being equal, the performance of the UKF with respect to species appears relatively consistent. However, the effects of sampling errors on estimated inlet composition appear more prevalent for propylene compared to acetylene at high composition frequencies. At a frequency of 1.5Hz, the propylene estimations/measurements display an interesting pattern where the composition profile alternates between being adequately and poorly captured at periods of approximately five seconds. This tendency is clearly illustrated in Figure 4-9d, where the FTIR measurements are out of phase with the peaks of the composition profile for the first two seconds, resulting in a flat-lined estimated composition profile. Afterwards, the measurement profile gradually realigns with the composition peaks, yielding improved estimations. While present for both species, these phase effects appear more regularly for propylene. This may be due the elevated levels of centerburst weighting for propylene measurements, which decreases the amount of new information acquired about the composition profile during a forward scan (since forward scan measurements are heavily weighted by the previous composition value). The reduction of the importance of forward scans effectively reduces measurement frequency, increasing the prevalence of sampling errors. For comparison, complete centerburst weighting would effectively cut the measurement frequency in half, which pushes the oscillation frequency in the 1.5Hz profile above the Nyquist limit.

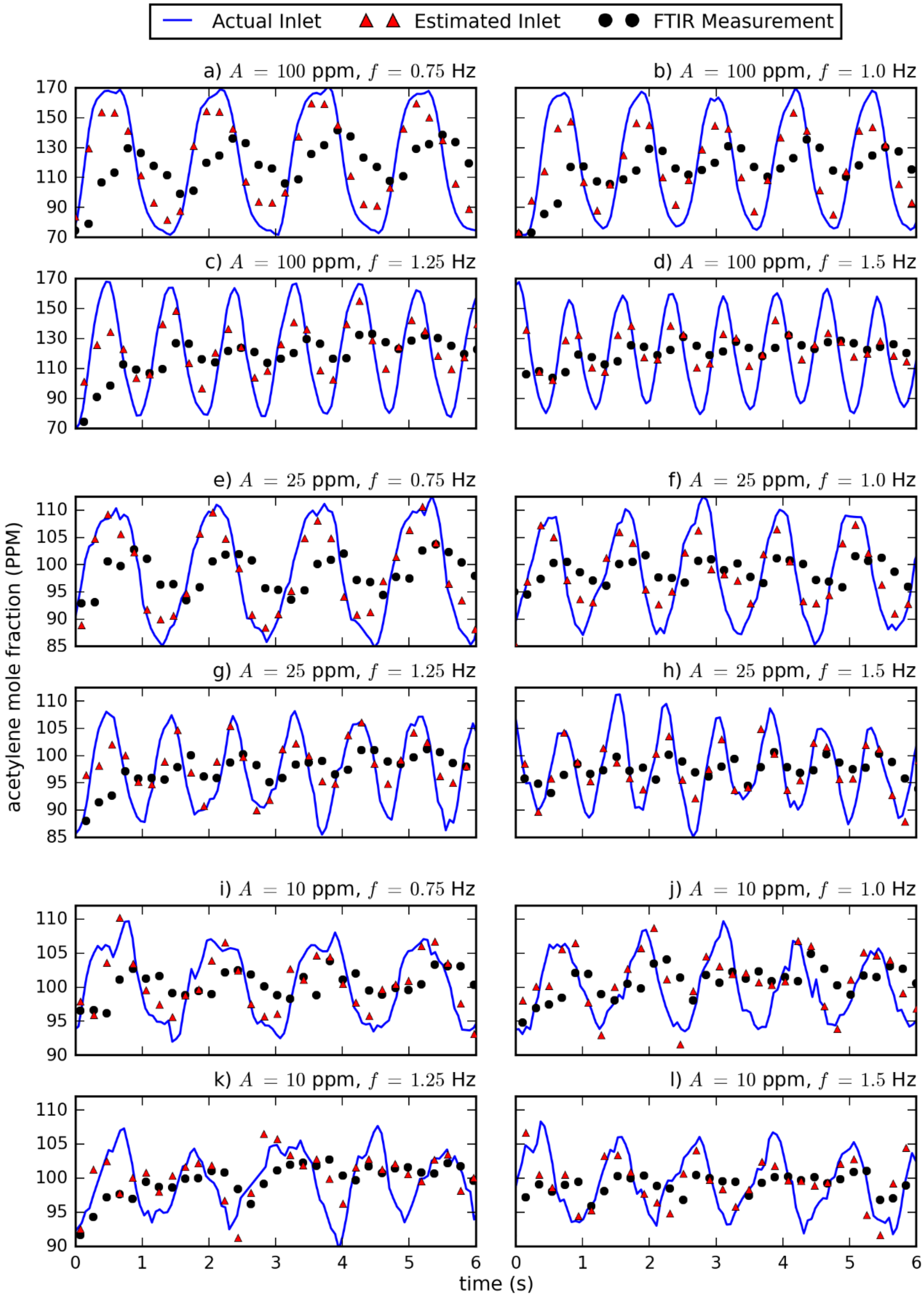

Figure 4-8: Estimations from the UKF of acetylene inlet composition vs FTIR measurements. The frequencies and amplitudes of the transient composition profiles vary from 0.75 to 1.5 Hz, and 10 to 100 ppm, respectively. The sample flow rate is 12 slpm.

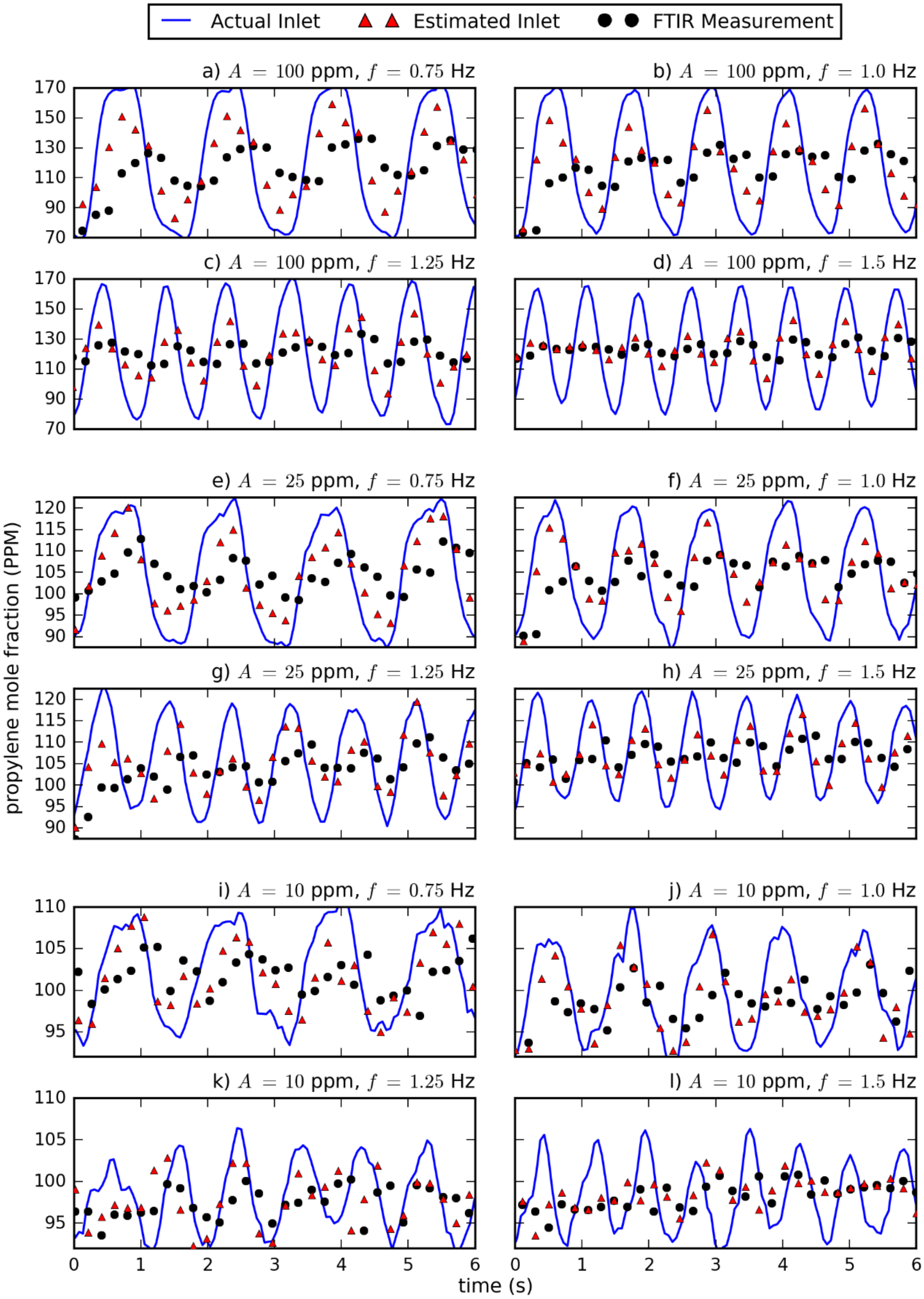

Figure 4-9: Estimations from the UKF of propylene inlet composition vs FTIR measurements. The frequencies and amplitudes of the transient composition profiles vary from 0.75 to 1.5 Hz, and 10 to 100 ppm, respectively. The sample flow rate is 12 slpm.

Figures 4-10 and 4-11 show data for wave inlet composition profiles for experiments conducted at a sample flow rate of 25 slpm for acetylene and propylene, respectively. Many of the trends from the 12 slpm cases are also seen in these figures, namely that lower frequency and higher amplitude result in better estimations. However, more accurate estimations of the amplitudes of the transient inlet composition profiles are generally obtained for the 25 slpm cases when compared with their counterparts in Figures 4-8 and 4-9. This is due to residence time being reduced at higher flow rates. With a lower residence time, old sample within the gas cell is displaced more quickly and the total gas cell composition profiles resemble the inlet composition profiles more closely. This is seen by comparing the measurements in Figures 4-8d and 4-10d, which correspond to the 100 ppm, 1.5 Hz cases for acetylene. For the higher flow rate case, the extremes of the measurement profile are closer to those of the inlet composition profile, which results in the extremes of the inlet composition profile to be more accurately calculated in general. However, even at the higher flow rate, the effects of lagging are still apparent and measurement frequency limitations still apply. This is especially true for the high frequency inlet composition cases. Furthermore, sampling error effects for propylene remain exacerbated by elevated centerburst weighting values at the higher flow rate, as evidenced in Figures 4-11d and 4-11h which display results for the 1.5Hz, 100 and 25 ppm cases, respectively. Distinct regions of accurate estimations and aliasing are apparent in both figures, which are caused by the effective sampling frequency reduction from centerburst weighting.

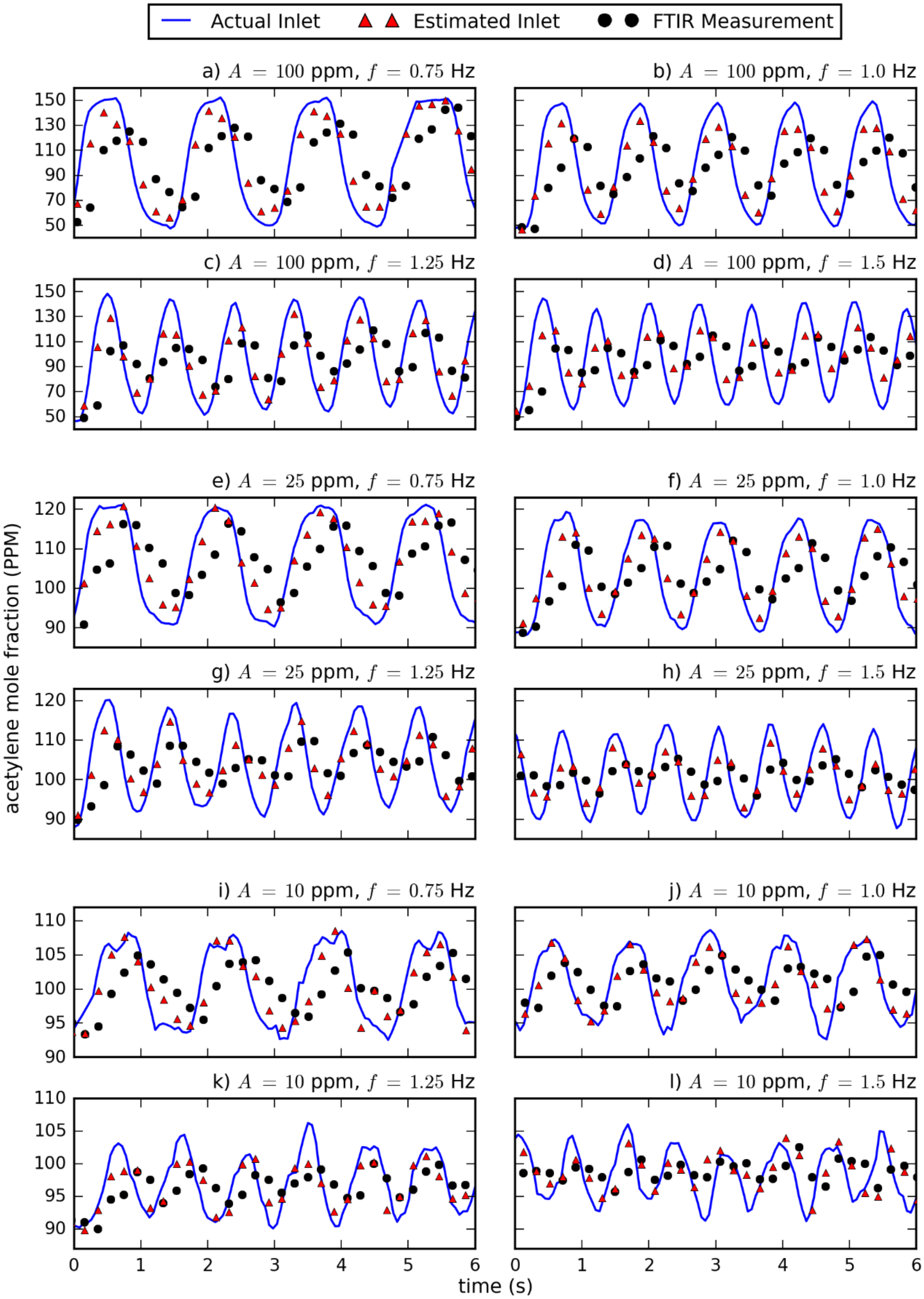

Figure 4-10: Estimations from the UKF of acetylene inlet composition vs FTIR measurements. The frequencies and amplitudes of the transient composition profiles vary from 0.75 to 1.5 Hz, and 10 to 100 ppm, respectively. The sample flow rate is 25 slpm.

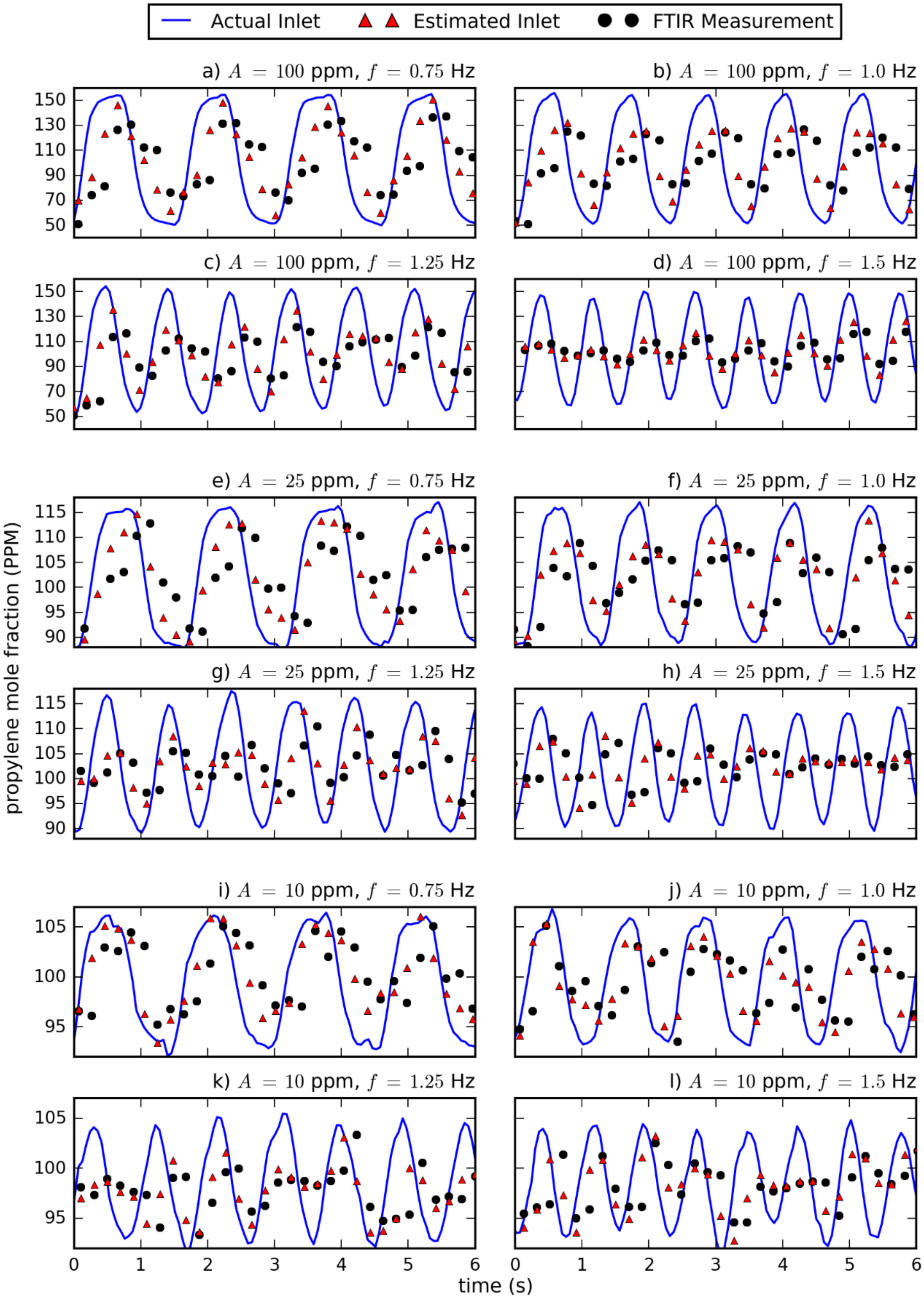

Figure 4-11: Estimations from the UKF of propylene inlet composition vs FTIR measurements. The frequencies and amplitudes of the transient composition profiles vary from 0.75 to 1.5 Hz, and 10 to 100 ppm, respectively. The sample flow rate is 25 slpm.

4.4.2.2 Spline Profiles

Emissions profiles from vehicles undergoing real-world driving cycles, which contain irregular periods of acceleration and deceleration, likely do not resemble to the wave profiles from the experiments presented in Figures 4-8 through 4-11. To simulate more realistic emissions profiles, experiments are conducted for inlet composition spline profiles generated from randomly selected set points within a distribution. Two sets of five spline profiles are used for these experiments, totaling 10 profiles. In the two sets of profiles, set points are separated by 0.4 and 1 s, respectively. Profiles with distinct set point separations (t_s) are used to investigate how performance of the UKF changes with respect to the duration of composition fluctuations. To ensure that the composition profile is relatively smooth and contains minimal steady-state portions, one interpolation point is used midway between set points. This is especially necessary for the set of profiles where t_s is 1 s, as this is less than the settling time of the mass flow controllers. To avoid having two consecutive set points within the resolution limit of the flow controllers, a set point remains unchanged if its randomly selected value is within 1/3 of a standard deviation of the previous set point. This ensures stability of the flow controller. The spline profiles are presented in Figure 4-12. Green and grey lines correspond to profiles where t_s is 0.4 and 1 s, respectively. To investigate how the magnitude of emissions variations affect filter performance, two sets of experiments with different scales are conducted for each spline profile. The standard deviations of the set points ($\sigma_{Z_{in}}$) for both experiments are 15 and 45 ppm, respectively. Thus, inlet composition in the figure is expressed as the difference from the mean inlet composition in terms of standard deviations. As in the wave profile cases, two sets of experiments are conducted for each profile/magnitude combination at sample flow rates of 12 and 25 slpm, respectively.

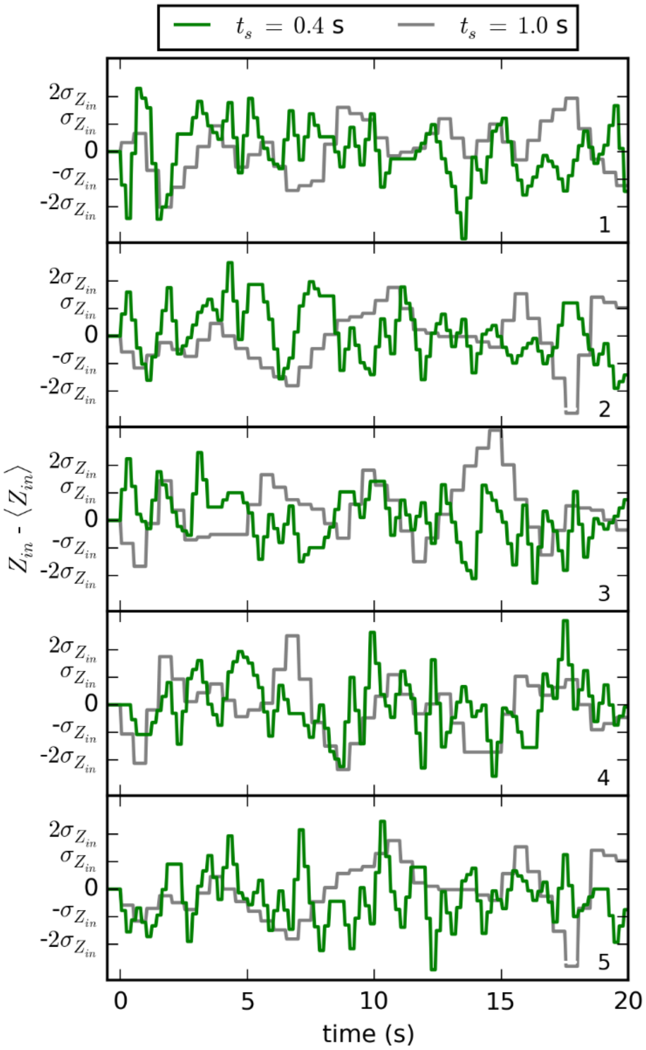

Figure 4-12: Transient inlet tracer composition spline profile set points expressed in terms of standard deviations from the mean.

Figures 4-13 and 4-14 shows results for inlet composition profile 1 of the 0.4 s interval cases for each inlet composition standard deviation and flow rate combination for acetylene and propylene, respectively. In general, the estimated inlet composition from the UKF follows the true inlet composition profile more closely than the unfiltered FTIR measurements. Similar trends as those found in wave profiles are also found in the spline profiles. The peaks and troughs of the unfiltered FTIR measurements are more representative of that of the inlet composition profiles for the higher flow rate cases, due to decreased residence time. As a result, the peaks and troughs of the estimated inlet composition profiles for the high flow rate cases are more accurate as well. This is apparent, for example, when comparing estimations of the first peak from Figures 4-13c and 4-13d, which correspond to the 12 slpm and 25 slpm cases where $\sigma_{Z_{in}}$ is 45 ppm for acetylene as the tracer gas. The estimation in the low flow rate case reaches only about 70% of the true apex, while the high flow rate estimation reaches within a few percent. Qualitatively, fewer anomalous oscillations in estimated inlet composition appear for the cases with higher flow rates and magnitudes of inlet composition changes. This is seen when comparing Figure 4-13a (the 15 ppm, 12 slpm case) with the remaining cases in the figure. Measurement noise is ultimately responsible for these oscillations. Cases with lower flow rates/composition fluctuations are more susceptible to measurement noise effects since the ratios between measurement changes and noise are lower. Estimations of propylene composition appear slightly qualitatively worse. For example, when comparing Figure 4-13a with 4-14a (the 15 ppm, 12 slpm cases), it is seen that the estimated inlet composition profile fails to capture some of the peaks. Again, this is likely due to effective measurement frequency reduction due to centerburst weighting. Nevertheless, the UKF improves estimated composition for both species.

Shown in Figures 4-15 and 4-16 are results for inlet composition profile 1 of the cases where t_s is 1 s for acetylene and propylene, respectively. Many of the same observations from the spline cases with lower duration between set points can be discerned from the data in Figures 4-15 and 4-16. Peaks and troughs are more accurately captured in the high flow rate cases and the effects of measurement noise are appreciable for the 15 ppm, 12 slpm case. The key difference between the results from the two sets of profiles is that the lag between inlet composition and FTIR measurement profiles is less significant for the 1 s interval cases, resulting in more accurate overall estimations for inlet composition. Since the inlet composition changes trajectory less frequently for these cases, the total gas cell composition/FTIR measurements have more time to respond to inlet composition transients. Furthermore, differences in estimation accuracy between acetylene and propylene are less discernable at the slower inlet composition frequency, due to reduced ratios of inlet composition to effective measurement frequency which weaken the aliasing effect of high centerburst weighting.

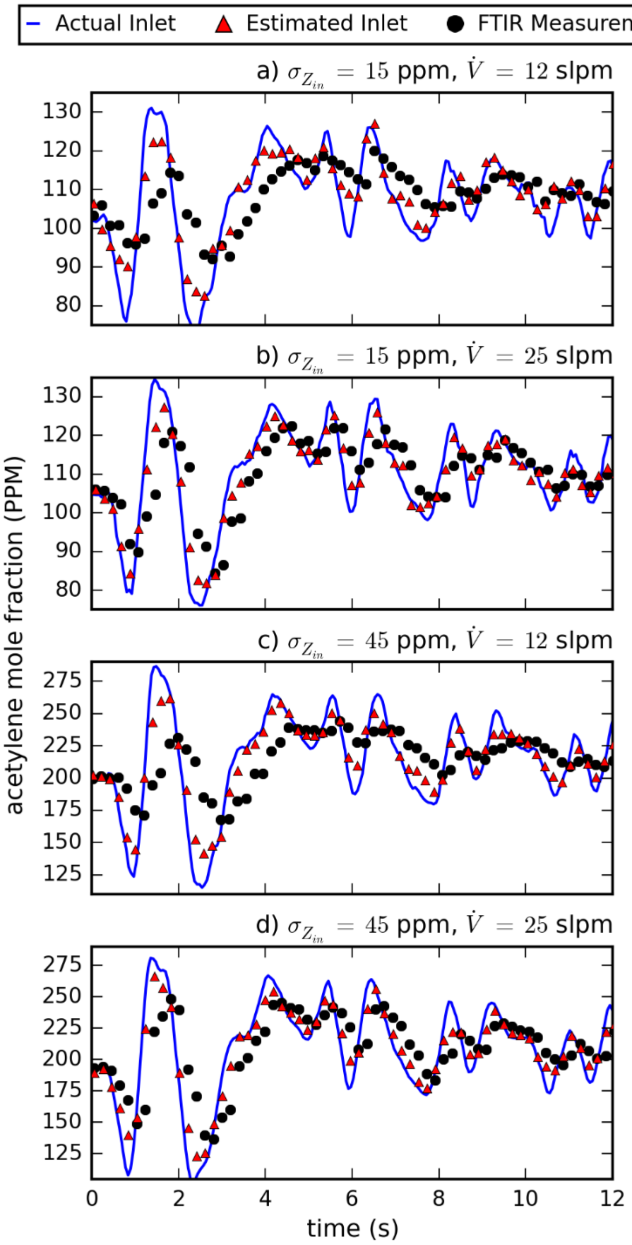

Figure 4-13: Estimations from the UKF of acetylene inlet composition vs FTIR measurements for the first 12 s of spline profile 1 of the t_s = 0.4 s set. Each window presents results for distinct values of $\dot{V}$ and $\sigma_{Z_{in}}$.

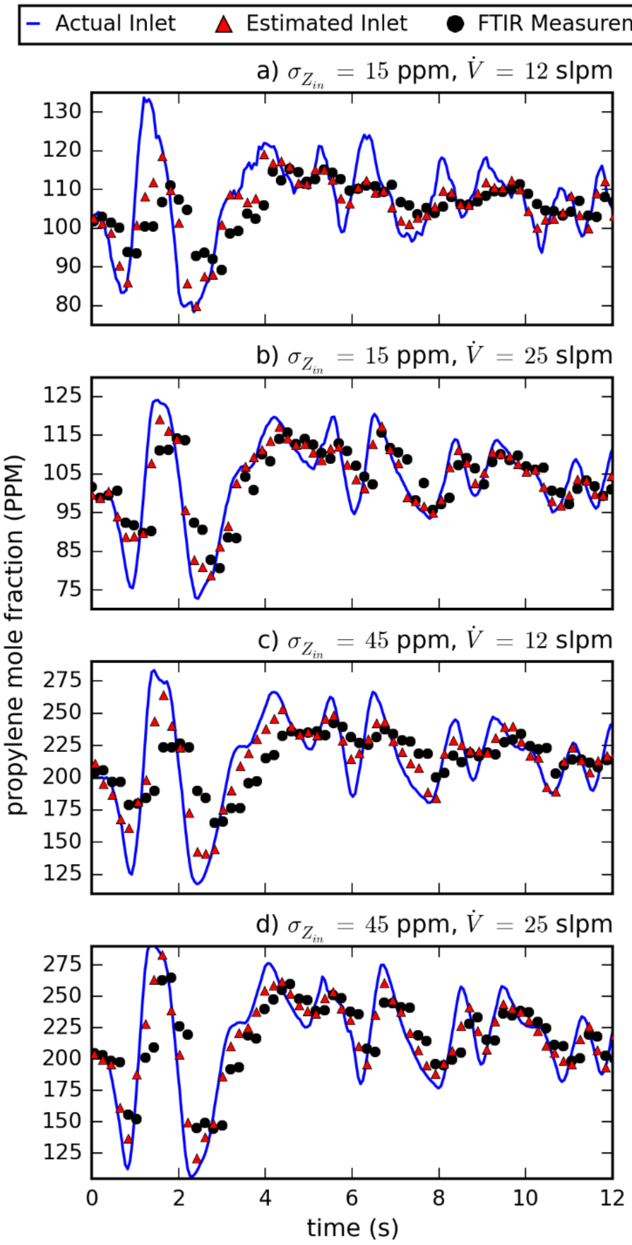

Figure 4-14: Estimations from the UKF of propylene inlet composition vs FTIR measurements for the first 12 s of spline profile 1 of the t_s = 0.4 s set. Each window presents results for distinct values of $\dot{V}$ and $\sigma_{Z_{in}}$.

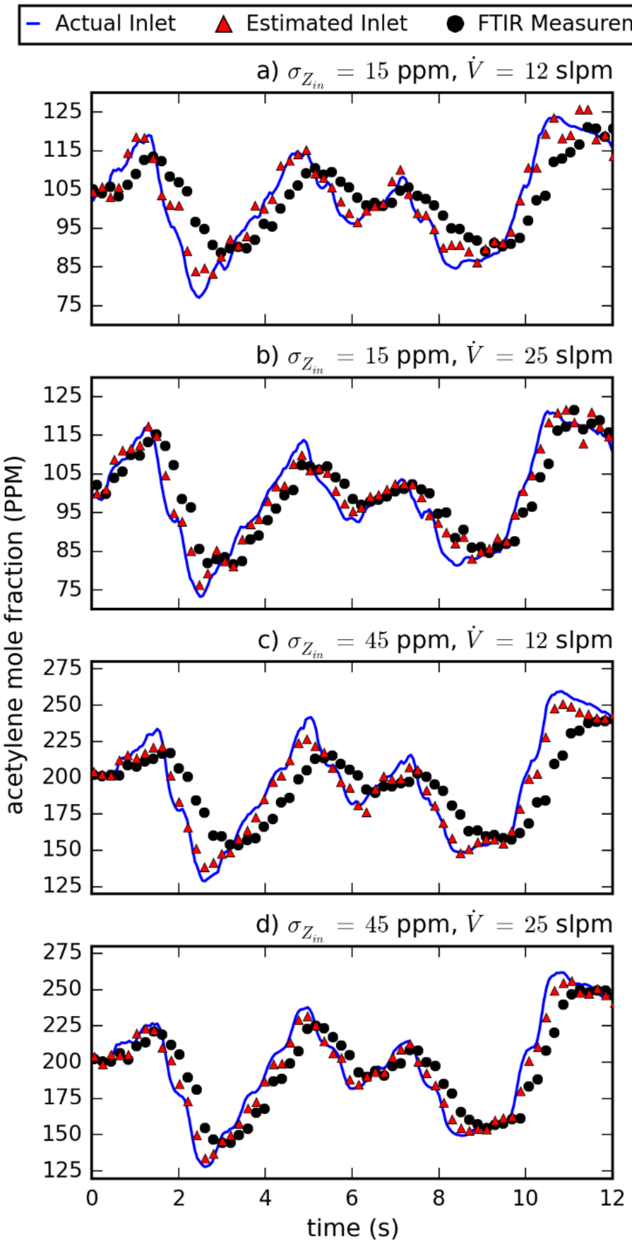

Figure 4-15: Estimations from the UKF of acetylene inlet composition vs FTIR measurements for the first 12 s of spline profile 1 of the t_s = 1 s set. Each window presents results for distinct values of $\dot{V}$ and $\sigma_{Z_{in}}$.

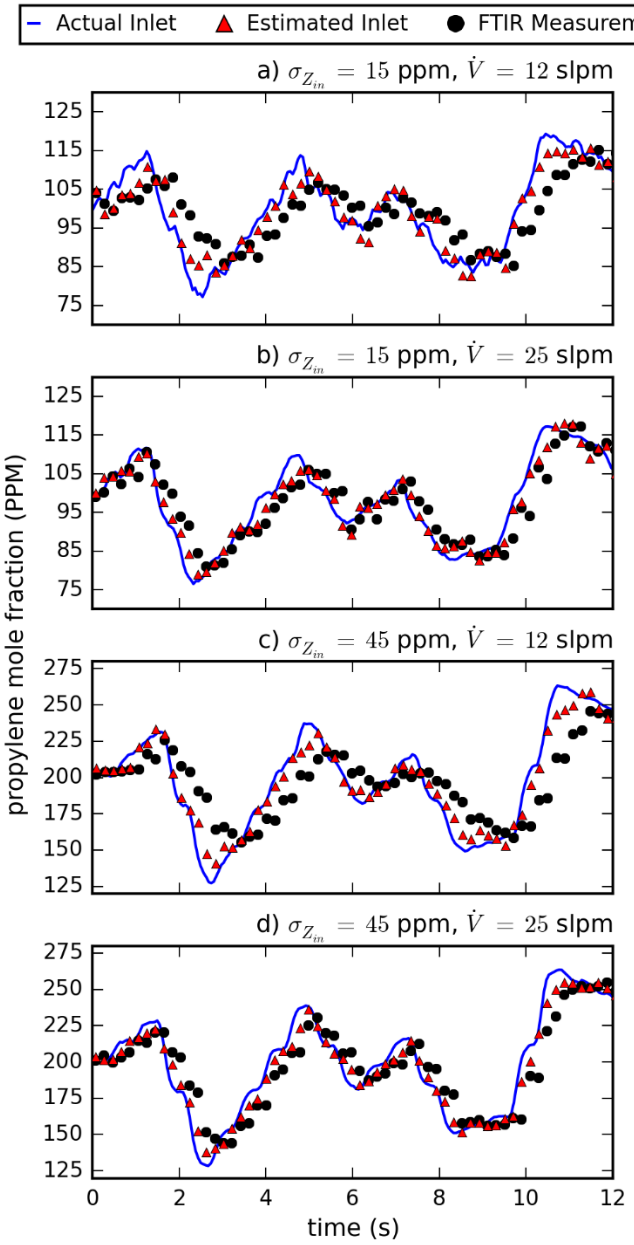

Figure 4-16: Estimations from the UKF of propylene inlet composition vs FTIR measurements for the first 12 s of spline profile 1 of the t_s = 1 s set. Each window presents results for distinct values of $\dot{V}$ and $\sigma_{Z_{in}}$.

To quantify the performance of the UKF for the spline inlet composition profiles and support some of the qualitative observations made in previous paragraphs, data from the spline experiments is consolidated according to flow rate, inlet composition magnitude and duration between set points. These data are presented in Figure 4-17, which shows the average absolute error in estimated inlet composition over all experiments for each category for acetylene and propylene as tracer gases. Average absolute differences between FTIR measurements and true inlet composition is also presented, which serves as a benchmark to which inlet composition estimations are compared. The UKF significantly improves the estimation of the transient inlet composition profiles compared to the raw FTIR measurements in every case for both acetylene and propylene. For the acetylene cases, a maximum relative improvement of 68% is achieved for the case where $\dot{V}$ = 12 slpm, $\sigma_{Z_{in}}$ = 45 ppm and t_s = 1 s, while the case with minimum improvement is the $\dot{V}$ = 25 slpm, $\sigma_{Z_{in}}$ = 15 ppm and t_s = 1 s case at 50%. Propylene shares the same case of maximum relative improvement as acetylene, whose value is 65%, while the case with minimum improvement is the $\dot{V}$ = 12 slpm, $\sigma_{Z_{in}}$ = 15 ppm and t_s = 0.4 s case at 32%. Relative improvements by the UKF for the experimental results generally exceed those of the synthetic FTIR measurements presented in Chapter 3. This is partially due to the modified UKF using current measurements to inform and update previous inlet composition estimations, which mitigates the lagging effect by considering the inlet composition trajectory. Also, inlet composition fluctuation frequencies for the experimental results generally exceed those of the synthetic results, resulting in greater overall measurement error and therefore more opportunity for improvement by the UKF.

Figure 4-17 also illustrates UKF performance trends with respect to the various categories. Lower measurement and estimation errors are achieved for the transient profiles with a t_s value of 1 s compared to that of 0.4 s. The average deviation between FTIR measurements and true inlet composition values is 11.01 and 14.65 ppm for t_s values of 1 and 0.4 s, respectively. For transient profiles with fluctuations of shorter duration, FTIR measurements have less time to respond to these fluctuations which leads to estimations with greater error. The UKF is also more effective for cases where inlet composition fluctuations are of greater magnitude. On average, the UKF improves the estimated composition profile by 50% and 59%

for the cases where $\sigma_{Z_{in}}$ is 15 and 45 ppm, respectively. This is expected, since measurement noise is more comparable to the magnitude of FTIR measurement fluctuations for the 15 ppm cases, resulting in greater masking of the true composition profile. Increasing flow rate from 12 to 25 slpm decreases measurement and estimation errors by 16% and 17% on average, respectively. At higher flow rates, residence times within the gas cell are shortened, reducing the lagging effect and resulting in measurements and estimations that more accurately reflect the true inlet composition.

Perhaps the most interesting tendency emerges when comparing between results for acetylene and propylene. For the t_s = 0.4 s cases, the UKF consistently achieves lower relative improvements for propylene. However, estimation improvements between species are similar for the t_s = 1 s cases. The average improvement percentages by the UKF for acetylene and propylene over all t_s = 0.4 s cases are 57% and 47%, respectively. By comparison, these respective improvements are 57% and 55% for t_s = 1 s. This performance decline for propylene at shorter composition trajectory durations is likely due to increased levels of effective aliasing due to centerburst weighting. Centerburst weighting – which is more substantial for propylene measurements – reduces the amount of new information acquired during a forward scan, since the resulting measurement is highly correlated to the composition acquired during the previous backward scan. For absolute centerburst weighting, the effective Nyquist frequency is reduced to 1.25 Hz. This frequency exceeds that of the composition fluctuations during the t_s = 1 s cases but not the t_s = 0.4 s cases, explaining the slight degradation in estimation accuracy for the latter.

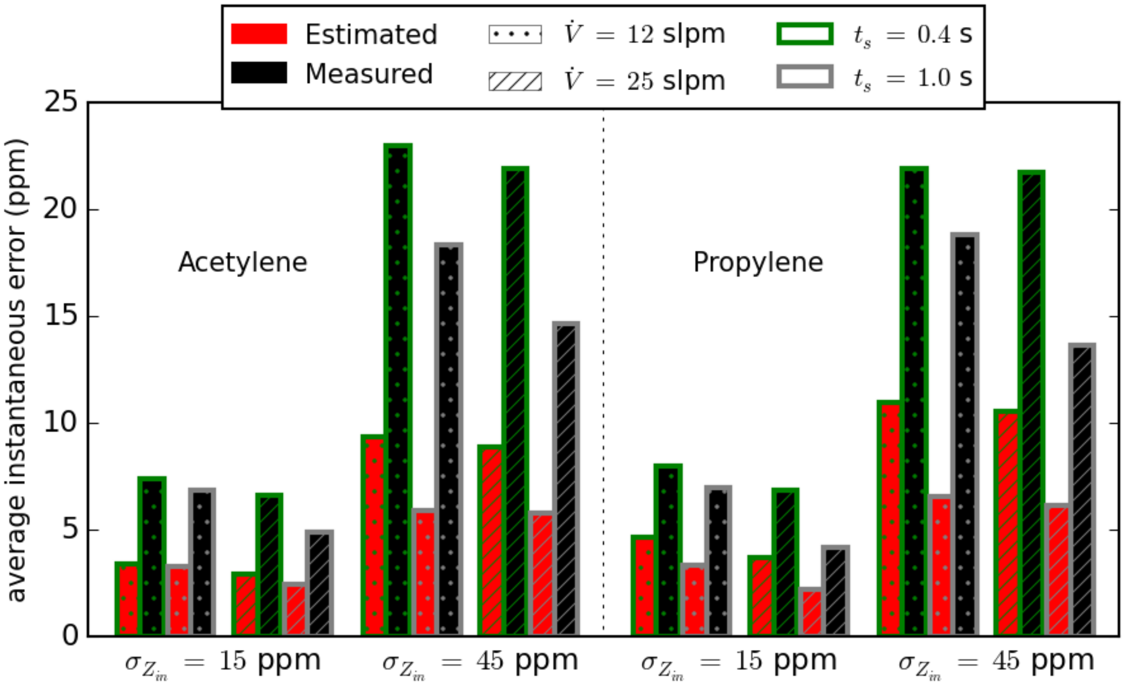

Figure 4-17: Average error in instantaneous acetylene and propylene inlet composition calculated from the UKF (red) and unfiltered FTIR measurements (black) for distinct values of t_s, $\dot{V}$ and $\sigma_{Z_{in}}$.

4.5 Opportunities to Improve the Modified UKF

Despite the demonstrated ability of the modified UKF to improve sample composition estimations from transient FTIR measurements, many simplifying assumptions are invoked in its construction. These assumptions may be inaccurate for certain species and composition profiles, imposing restrictions on the amount of improvement that can be attained by the UKF. These limitations are worth discussing to guide future advancements of the UKF. Each simplifying assumption is listed below in italics, followed by an explanation of the ramifications of the assumption and a discussion of potential solutions if available.

Composition/absorbance/intensity for each species evolves linearly with respect to OPD during a moving mirror scan.

To calculate a centerburst weighting value for a chemical species, the calibrated absorption spectrum of that species is convolved with a linearly evolving power profile with respect to OPD. This provides an estimation of the relationship between the true, transient spectrum during a FTIR scan and the resulting spectrum from the Fourier transform of the interferogram. While the assumption of a linear power profile provides superior composition estimations compared to the standard Fourier transform – which assumes a stationary power – true composition profiles are more complex and time-varying. However, it is difficult to know the exact transient power profile with respect to OPD *a-priori*. Therefore, one must be assumed, the simplest of which is a linear one. However, it is known that when inlet composition is constant, total gas cell composition evolves with an exponential profile. This information could be used to develop more accurate power profiles. However, further analysis is needed to determine if such considerations would result in improvements that warrant adding such complexity.

Along similar lines, it is implicitly assumed within the measurement model of the UKF that time and OPD are linearly related, or that scan speed is constant. Such an assumption is necessary to extract the composition profile with respect to time. In reality, moving mirrors have periods of acceleration and deceleration at the beginning and end of a scan, respectively. However, these effects could be easily incorporated into the UKF if the position/velocity profile of the moving mirror with respect to time is known, although it would create a more complicated convolution. Again, such complex modifications may result in modest improvements. Further analysis is required to determine if this is so.

Composition/absorbance/intensity are linearly related.

The calculation of centerburst weighting is originally formulated based on the assumption that IR intensity evolves linearly with respect to OPD. To estimate the effects of centerburst weighting in terms of composition in a simplified manner, it is further assumed that intensity, absorbance and composition are linearly related. However, absorbance is log-based function of intensity (see Equation 4-12) which is highly non-linear at high levels of absorbance. Furthermore, the relationship between absorbance and composition is non-linear for many narrowly absorbing species due to non-constant absorptivities [104], resulting in underestimations of centerburst weighting. A more rigorous centerburst calculation would identify a specific gas cell composition profile with respect to time/OPD, and calculate a corresponding absorption profile using the Beer-Lambert law and/or absorbance calibrations. This absorption profile would then be transformed to an intensity profile according to Equation 4-12 using base intensities specific to a FTIR, which may vary with respect to wavenumber. The resulting biased intensity spectrum due to evolving power would then be calculated according to modified a version of Equation 4-11, which would then be converted to back to an absorbance spectrum and ultimately a composition via the FTIR's modified least-squares algorithm. If even more rigor is desired, the modified version of Equation 4-11 may account for variations in the power profile with respect to wavenumber (i.e., γ becomes a function of wavenumber), although the derivation of such an equation would be exceedingly complicated. This convolution could even be included within the measurement model itself and performed for each measurement sigma point. Such a modification would increase the accuracy of the measurement error distribution and corresponding composition estimation. However, it would require access to the FTIR's proprietary least-squares algorithm, or the creation of a separate algorithm that maps absorbance and composition. Furthermore, it may add complexity that outweighs the associated benefits.

Interference is negligible.

The analysis regions within FTIR calibrations for a single species are typically selected to minimize interference from other species. However, a certain amount of cross-talk between species is inevitable. While accounted for within the FTIR's least squares algorithm for deducing gas cell concentration from spectral absorbance, interference effects are neglected in the calculations of centerburst weighting for the UKF. This is important to note, since the effects of interference likely manifest themselves differently between stationary and non-stationary measurements. For example, the least squares algorithm within the FTIR likely accounts for interference by simply subtracting out the predicted absorbance levels of interfering components according to their measured compositions. However, if the composition of the interfering component itself is transient, the calculated interfering absorbances are also biased by centerburst weighting, creating additional bias in the resulting composition calculation. This issue could perhaps be addressed by including the convolution itself within the measurement model, as discussed above. However, the convolution would be performed for the entire spectrum, so that the effects of transients for multiple species and their resulting cross-talk could be accounted for.

Clearly, a lot of opportunity remains for further improvement of the UKF. Future work should address the three key simplifying assumptions outlined above and attempt to implement some of the proposed solutions.

4.6 Chapter Summary

The UKF is augmented to combat the biasing effects of non-stationarity on FTIR measurements for the ultimate purpose of attaining time-resolved estimations of the composition of engine emissions. Non-stationarity and its biasing effects on FTIR measurements of chemically evolving samples are introduced, discussed and exemplified in experimental FTIR data. Mathematical analysis is laid out which proves that centerburst weighting and alternating scan direction are indeed a result of non-stationarity and responsible for biases observed in FTIR measurements. This mathematical analysis is expanded to predict the magnitude of centerburst weighting of FTIR measurements of specific species using calibrated absorbance spectra. These centerburst calculations are then incorporated into the UKF, which is modified to deduce gas cell composition from FTIR measurements that are biased by non-stationarity. Experimental validation of the modified UKF is performed by flowing trace, controlled amounts of acetylene and propylene through the FTIR, which have different magnitudes of centerburst weighting. The modified UKF is experimentally demonstrated to overcome biasing effects due to sample recirculation and non-stationarity to accurately infer inlet tracer gas cell composition from FTIR measurements. The following is a list of conclusions from the experimental results presented in this chapter.

- The modified UKF is shown to consistently reproduce wave composition profiles at frequencies up to 1.25 Hz and amplitudes down to 10 ppm from biased FTIR measurements. Amplitudes of estimated composition profiles from the UKF are closer to the true amplitudes than those from unfiltered FTIR measurements, which lag the true profile due to residence time effects.
- The UKF yields quantitative improvements in the estimated sample profile for spline profiles of varying average amplitudes and fluctuation duration. On average, the UKF yields a 58% and 51% improvement in estimated acetylene and propylene inlet composition, respectively, over unfiltered FTIR measurements across all spline profiles and flow rates tested. More accurate estimations are obtained for profiles with fluctuations of greater duration and magnitude, due to residence time and measurement noise effects, respectively.
- Measurement and estimated inlet composition improvements of 16% and 17% are achieved on average for the spline profiles, respectively, when increasing flow rate from 12 to 25 slpm. An overwhelming majority of the emissions measurement literature reports flow rates near 10 slpm. The results from this study indicate that for future emissions measurements, sample flow rate should be maximized while still maintaining appropriate pressures within the FTIR gas cell and avoiding turbulence effects.

- Greater estimation accuracy for highly transient composition profiles is achieved for acetylene relative to propylene. This is due to the effective measurement frequency reduction induced by elevated centerburst weighting associated with propylene measurements. Perhaps future FTIR recipes should maximize the number of narrow absorbing regions within an analysis region to minimize centerburst weighting.
- Three key simplifying assumptions in the formulation of the centerburst weighting calculations and the modified UKF and their potentially negative implications are discussed in detail. These include the assumptions of linearly evolving composition within the gas cell, a linear relationship between intensity/absorbance/composition, and the negligibility of interference effects. Future modifications to the UKF should address these assumptions.

With the UKF developed and experimentally validated, the following chapter will detail a study of engine emissions from a gasoline engine during transients that utilizes the UKF.

CHAPTER 5 EXPLORATION OF HYSTERESIS IN SPECIATED EMISSIONS

Detailed in this chapter is an experimental investigation of transient effects on emissions from a gasoline engine under transient load profiles using the modified UKF. As discussed extensively in the background and motivation portion of this dissertation, there is currently a severe shortage of time-resolved, transient VOC emissions data in the literature. The literature is currently dominated by steady-state data or batch reports of total emissions over an entire driving cycle. While batch reports are useful for assessing the performance of an engine during real-world driving conditions, they provide minimal information on the relationships between specific engine operational conditions and emissions and therefore little insight into opportunities for improving engine design and operation. Furthermore, while such information can be obtained from emissions measurements during steady-state operation at various speeds and loads, such measurements are absent of transient effects and are therefore unrealistic.

Thus, to address the lack of time-resolved, transient VOC emissions data in the literature and elucidate the relationship between species distribution of emissions and engine operational points, exhaust composition from a spark-ignited, port fuel-injected gasoline engine under various transient load ramps is measured and analyzed. Positive and negative ramp load profiles with brake mean effective pressures (BMEP) ranging from 2 to 7 bar at a constant speed setting of 1500 rpm are explored. Emissions are additionally explored at 2000 rpm, and the results are displayed in the appendix. To investigate acceleration and short term transient effects on VOC emissions, ramp durations are varied between 1 and 5 seconds. Periodic ramp waves lasting up 30 seconds are also investigated to explore long term historical effects. Emissions from these experiments are compared to predicted emissions from a quasi-steady model, which utilizes an emissions map generated from experiments conducted at various constant speeds and loads. To gauge whether differences between experimental emissions and those predicted by the quasi-steady model are due to deterministic, repeatable transient effects or stochastic and/or non-repeatable emissions fluctuations, the magnitudes of the stochastic/non-repeatable component of each emissions measurement are estimated. Stochasticity standard deviation is calculated from the emissions data from the steady-state experiments. To address sample recirculation and spectral IR intensity stationarity issues associated with FTIR measurements of sample with rapidly evolving composition, the modified, experimentally validated UKF from Chapter 4 is employed to filter FTIR measurements. The UKF infers the true gas cell inlet composition from biased FTIR measurements, thereby enabling time-resolved, accurate estimates of comprehensive emissions.

5.1 Experimental Methods

Outlined in this subsection are the experimental architecture and methods used to measure and analyze transient engine emissions in this study. These include engine, dynamometer and FTIR specifications, as well as greater detail on the transient load profiles and generation of the steady-state emissions map and emissions stochasticity estimations. Also discussed are additional considerations for applying the UKF to emissions data that are not previously covered, such as estimations of the process and measurement noise covariance matrices.

5.1.1 Experimental Setup

A layout of the experimental setup is provided in Figure 5-1. Experiments are conducted on a 1.5L Kubota WG1605 four-cylinder, port fuel-injected, spark-ignited engine. This engine provides a maximum power output of 55 hp (41 kW) and operates at speeds between 750 and 3200 rpm and brake torques between 0 and 120 lb-ft (13.3 bar in mean effective pressure). A 100 hp (74.5 kW) AC dynamometer from Powertest Inc. is coupled to the engine shaft to impart resistive loading. Control of engine speed and dynamometer load is achieved using the PowerNet LT software package from Powertest. A Bosch LSU 4.9 exhaust wideband oxygen sensor is employed to measure air-to-fuel equivalence ratio downstream of the engine. Equivalence ratio measurements are reported at intervals of approximately 50 ms. Emissions measurements are performed using the same MKS 2030-HS FTIR spectrometer as the work presented in the previous chapter. For convenience, its specifications are briefly reiterated. The MKS 2030-HS measures at a frequency of 5 Hz, a spectral resolution of 0.5 cm^{-1} and an IR pathlength of 5.11 meters. The MKS 2030-HS is also equipped with a silicon carbide radiation source at 1200°C, a liquid nitrogen-cooled mercury cadmium telluride detector, and a helium neon laser is used to generate a reference interferogram.

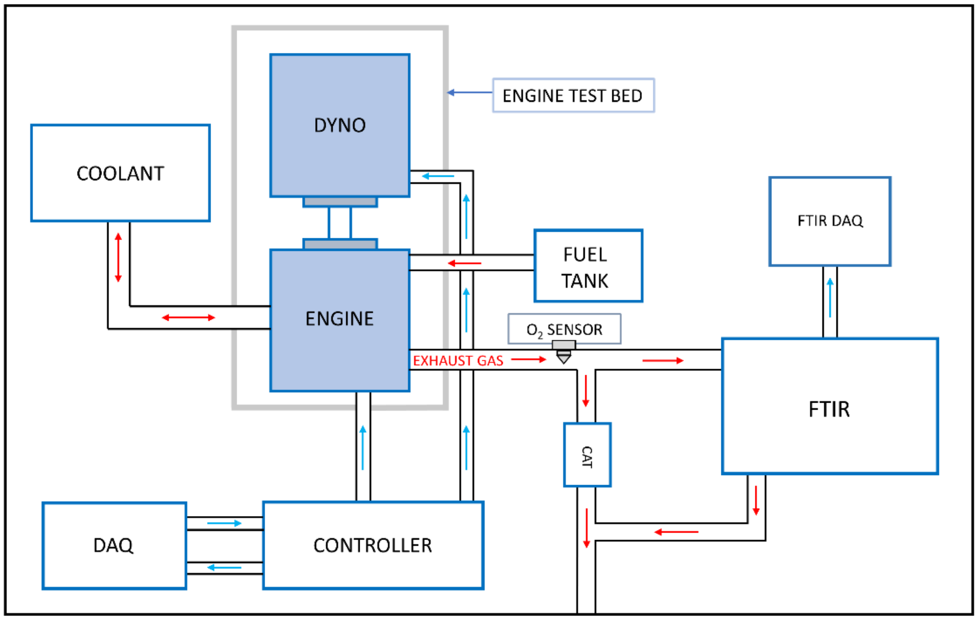

Figure 5-1: Engine test cell schematic.

5.1.2 Engine Load Profiles

Emissions measurements from the Kubota engine are conducted for two sets of engine load profiles. The first set consists of positive and negative load ramps between 2 and 7 bar (in BMEP) with durations of 1, 2.5 and 5 seconds. Different ramp rates are explored to investigate how acceleration and short-term speed/load history influences emissions. To examine the impact of long-term historical effects on emissions, a second set of periodic load ramps are imposed on the engine. The load in these profiles oscillates between the same extrema at the same durations as the single load ramps. These load oscillations are executed for approximately 30 seconds to allow possible long-term emissions trends to develop. The initial load point is maintained for approximately 2 minutes before the first load change to eliminate prior transient effects on the emissions. Experiments are conducted at two constant engine speed settings: 1500 and 2000 rpm. For brevity, only the results for engine speeds of 1500 rpm are presented within this chapter. The results for 2000 rpm are provided in the appendix, as most of the emissions patterns and discerned transient effects are qualitatively similar for both speeds. Two trials are performed for each load profile/engine speed combination to ensure repeatability. The transient load profiles are illustrated in Figure 5-2.

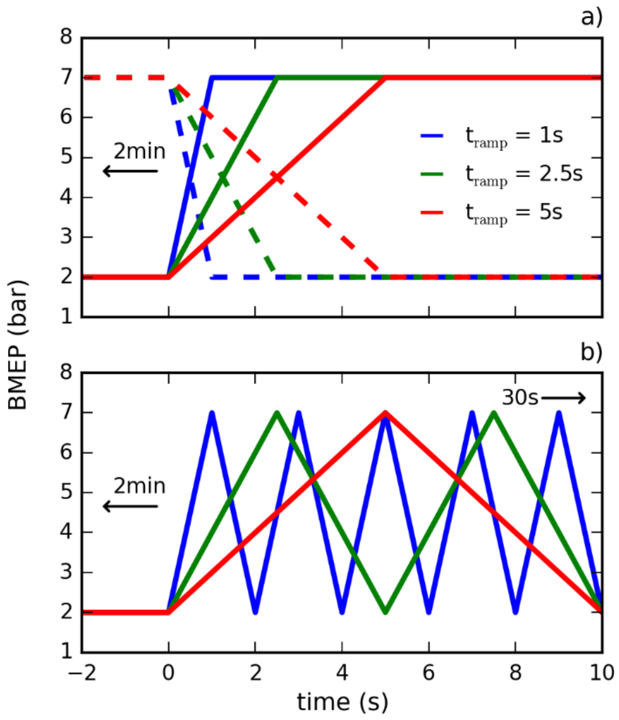

Figure 5-2: Illustration of the transient engine load profiles.

To quantify the transient and historical effects on emissions, each emissions measurement is compared with an estimation from a quasi-steady model. The model calculates each quasi-steady estimation using an emissions map created from experiments at constant speeds and loads. Figure 5-3 shows the speed/load points within the map. Speed ranges from 1000 to 2500 rpm with an interval of 250 rpm, while load (in BMEP) ranges from 2 to 7 bar with an interval of 1 bar. Measurements are taken for a total of three minutes at each speed/load point to determine the corresponding emissions value. Linear interpolation is used to estimate the emissions at intermediate speed/load points. To determine if discrepancies between quasi-steady predictions and experimental emission are due to transient effects (load/speed ramp rate) as opposed to stochastic/non-repeatable fluctuations, the standard deviation of emissions during each steady-state test is calculated for each speed/load point within the steady-state map. These calculations serve as an approximation for the stochasticity standard deviation at each speed/load point, and are used to generate a similar map for stochasticity. To deconvolve measurement noise effects from the calculated stochasticity, the steady-state measurements are filtered with the UKF before standard deviations are calculated. It should be acknowledged that transient effects may influence stochasticity. Thus, second trials are also consulted to judge whether a given emissions fluctuation is mostly stochastic, while stochasticity calculations serve as first approximations. Illustrations of the steady-state emissions and emission stochasticity standard deviation maps are provided in the appendix under *5.1.2 – Emissions Maps*.

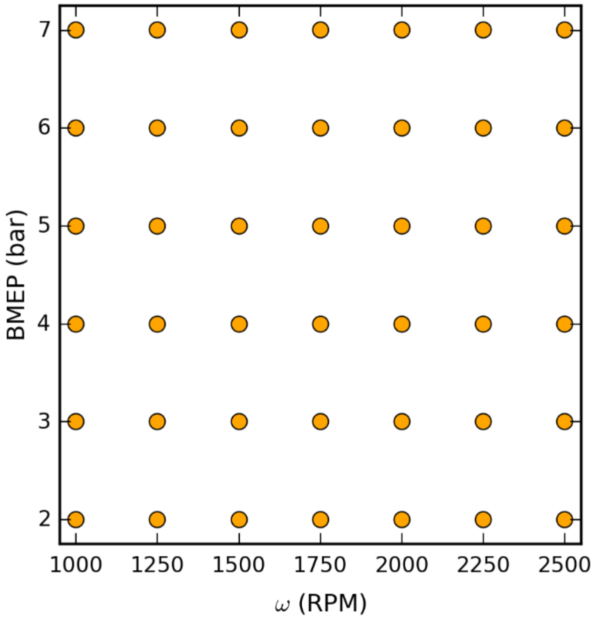

Figure 5-3: Speed/load points on the steady-state emissions map used to formulate the quasi-steady model.

5.2 Emissions Analysis using UKF

FTIR spectroscopy is an attractive diagnostic for comprehensive speciation due to its ability to distinguish individual VOCs according to their IR absorption spectra. However, as thoroughly discussed throughout this dissertation, FTIRs are susceptible to biasing effects that complicate the interpretations of measurements of chemically evolving samples: namely sample recirculation and non-stationarity. These limitations associated with transient FTIR measurements are addressed with the implementation of the modified UKF from Chapter 4. The UKF couples model predictions with FTIR measurements to obtain statistically optimized estimations of the instantaneous engine emissions/gas cell inlet composition, thereby providing accurate, time-resolved emissions profiles. Employed within the UKF is a sample recirculation model which relates total gas cell composition to inlet composition, and a measurement model which deduces the true gas cell composition from FTIR measurements during transients that are biased due to centerburst weighting. The centerburst weighting values utilized for this analysis are the same as those reported in Table 4-1. An overview of the UKF estimation process for estimate engine emissions from FTIR measurements is provided in Figure 5-4.

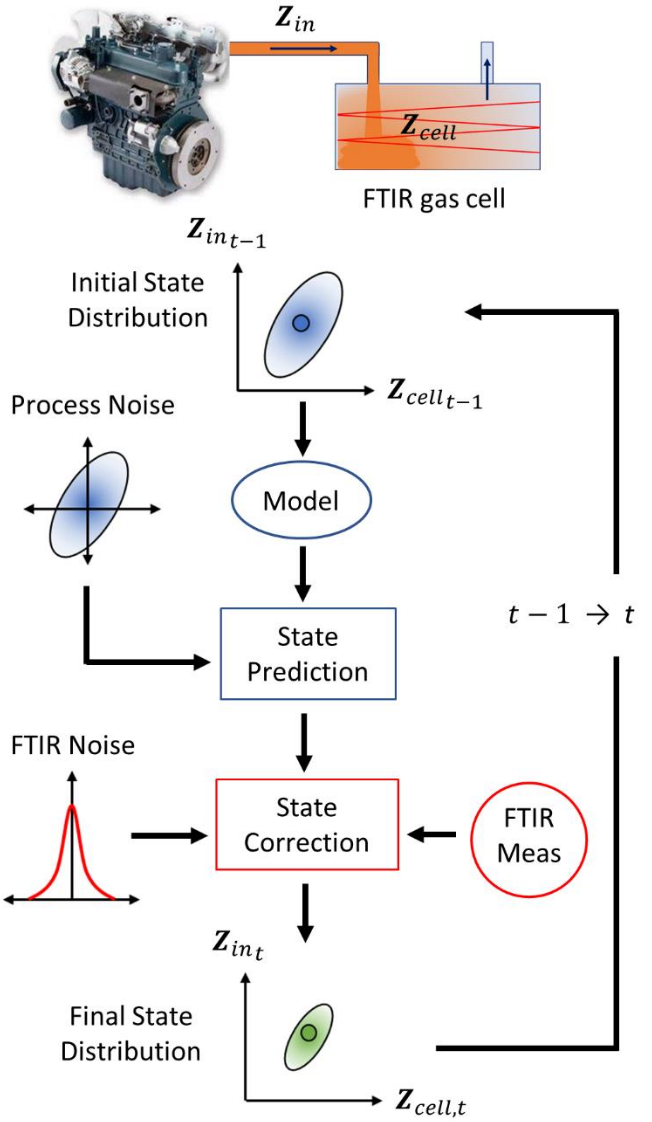

Figure 5-4: UKF flow chart for optimally estimating engine exhaust composition from FTIR measurements.

5.2.1 Process Noise Distribution

As discussed in Chapter 3, a key component of the UKF are the process and measurement noise covariance matrices. Distributions within these matrices guide the UKF when discriminating between measurement noise effects and true state value fluctuations. Reasonable estimations for these values is essential for obtaining statistically optimized emissions estimations. Process noise within the state transition model of the UKF is assumed to originate from fluctuations in inlet composition and mass flow rate, whose variances are represented by $\Phi_{Z_{in}}$ and $\Phi_{\dot{m}}$. The propagation of these fluctuations on total gas cell composition is estimated using the sigma-point transformation process outlined in Section 3.2.2. It is difficult to determine $\Phi_{Z_{in}}$ and $\Phi_{\dot{m}}$ *a-priori*, as the magnitudes of inlet composition/emissions fluctuations with respect to engine operation are the exactly what these experiments are designed to discover. However, reasonable first approximations can be attained using available steady-state emissions data. Thus, $\Phi_{Z_{in}}$ for each species is estimated using the squared difference between the maximum and minimum emissions value within the steady-state map divided by 4. For species for whom this value is less than 5 ppm, the emissions fluctuation is set to 5 ppm. Estimating the emissions fluctuation variances in this way provides appropriate scaling between species, as species whose emissions cover greater ranges on the steady-state map are expected to have greater fluctuations during transients. Other methods which converge on optimal process noise values to reduce estimation uncertainty could also be implemented for this purpose. This method is chosen for simplicity. The emissions fluctuation variance for each species is listed in Table 5-1. The value used for $\Phi_{\dot{m}}$ is the same as in Chapter 4 – 0.25 slpm. This value is a reasonable approximation of the fluctuations occur during load changes. Estimating the variance in composition measurements of engine exhaust due to noise is slightly more involved, and is detailed in the following subsection.

5.2.2 FTIR Composition Measurement Noise Distribution

For the UKF to accurately deduce the composition of engine emissions from FTIR measurements, the measurement noise statistics must be reasonably estimated. Since the UKF is expressed in terms mass/molar compositions, it is necessary to express the noise in terms of composition (as opposed to signal level) as well. However, typical FTIR algorithms – which convert the measured spectral intensity to chemical composition – use the intensity at several wavenumbers to infer composition to reduce noise effects. Moreover, for a given level of signal noise, the corresponding composition noise becomes greater as absorbance (composition) increases due to the decreasing signal-to-noise ratio. Even more, two or more species may absorb in the same spectral regions, and FTIR algorithms must be somewhat complex to account for this cross-talk. Thus, analytically determining the statistics of composition measurement noise is a difficult task, and is not as simple as using the signal-to-noise ratio at a single wavenumber. Therefore, composition measurement noise is estimated in this work using a Monte-Carlo-like method.

The first step in this method is to select one or more measurements for which the noise statistics are of interest. For this work, a measurement at approximately the midpoint of the engine load transient for the 1500 rpm, 2.5s upward load ramp is selected. Due to the tediousness of this method, it is only performed for this single measurement and the resulting statistics are applied to all remaining measurements. This measurement is selected since it occurs at the midway point of the loads explored in this work and is from an experiment with moderate ramp rate. In the second step, a series of FTIR noise measurements are conducted. In these measurements, the FTIR gas cell is filled with an unabsorbing gas (such as nitrogen), so that differences in spectral transmittance between each measurement are due to noise only. Thus, the spectral transmittance noise for a single measurement can be estimated by subtracting the average spectral transmittance from all measurements with that of the single measurement. Detector noise is the dominant form of noise in most commercial FTIRs [100]. Since detector noise is additive [100], the effects of measurement noise can be simulated by adding each transmittance noise spectrum to the transmittance spectrum from the measurement of interest. The resulting composition noise variance for each species is then estimated by operating on each synthetic spectrum with the FTIR algorithm to calculate a corresponding composition. The variance of the composition distribution is then calculated. A diagram of the process for estimating composition measurement noise is provided in Figure 5-5. For this work, approximately 1500 noise spectra are utilized. This number of spectra is determined to be sufficient, as analysis with 750 spectra changes the composition variance by less than 5% for each species. Measurement noise variance for each species is provided in Table 5-1 below.

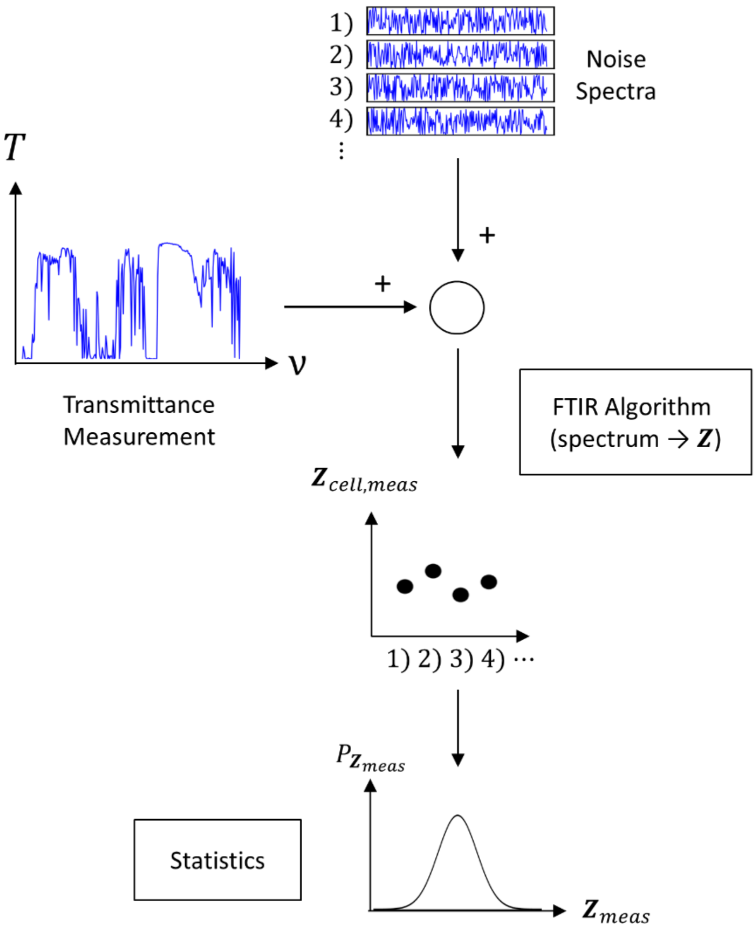

Figure 5-5: Illustration of process for estimating magnitudes of FTIR noise effects on measured species.

Species	Inlet Composition Process Noise Variance ($\Phi_{Z_{in}}$) (PPM)	Measurement Noise Variance ($\boldsymbol{R}_{vv,Z_{cell}}$) (PPM)
1,3 butadiene (C_4H_6)	5.00	4.60
Acetylene (C_2H_2)	63.50	1.48
Benzene (C_6H_6)	5.00	78.52
Cyclohexane (C_6H_{12})	5.00	0.29
Ethanol (C_2H_5OH)	31.76	6.52
Ethylene (C_2H_4)	94.92	1.39
Formaldehyde (CH_2O)	6.69	0.47
Methane (CH_4)	25.65	0.37
Pentane (C_5H_{12})	235.37	10.64
Toluene (C_7H_8)	8.86	63.60

Table 5-1: Estimated inlet composition process noise, FTIR measurement noise values used within the UKF for each species.

5.3 Results and Discussion

The emissions of various species with respect to engine speed, load and equivalence ratio for each transient profile are presented in this section. Transient engine emissions are estimated from FTIR measurements using the UKF. Predicted emissions from the quasi-steady model are presented alongside the estimated transient emissions for comparison. To determine if the differences between estimated transient emissions and quasi-steady predictions are statistically significant, the UKF estimations are presented with error bars which represent emissions uncertainty to one standard deviation. For clarity, error bars are only present for every other estimation. Quasi-steady predictions are also presented with a surrounding shaded region that represents the predicted standard deviation of stochastic emissions fluctuations. Such information provides an idea of whether the differences between the quasi-steady predictions and estimated emissions are simply due to stochastic fluctuations, or if there is a deterministic component of the transient emissions that can be predicted with a more sophisticated model. It should be noted that the quantified stochasticity in this analysis includes the possible effects of air-to-fuel equivalence ratio oscillations on emissions, which may be considered deterministic since these oscillations are the result of the engine control working to maintain stoichiometry. However, such effects are difficult to separate from other factors that may be considered stochastic and contribute to quasi-steady model errors in the same way. Furthermore, the timing of these oscillations with respect to the load profile may be considered random or stochastic. Air-to-fuel equivalence ratio measurements are presented for each speed/load profile. It should also be noted that since quasi-steady model predictions are ultimately derived from FTIR measurements, both the transient estimations (from the FTIR measurements and UKF) and the quasi-steady model predictions should be subject to similar systematic errors. Thus, discrepancies between the two should be indicative of transient effects, regardless of offsets due to systematic error.

A series of three fuel components and four reaction intermediates are plotted for each transient profile. The fuel components presented are cyclohexane, ethanol and pentane, while the intermediates presented are acetylene, ethylene, formaldehyde and methane. Due to the low concentrations and high measurement noise of benzene and toluene in this work, the ability to form substantial conclusions regarding the transient emissions of these species is limited. Thus results for these species are not presented, but a discussion of the factors that contribute to their elevated levels of measurement noise is provided in the last subsection of the chapter. Emissions of 1,3 butadiene are presented and discussed separately from the other species, as it is the only species where its emissions appear mostly dominated by stochasticity. Emissions for the 2000 rpm cases are included in the appendix under *5.3 – Experimental Emissions Data at an Engine Speed of 2000 RPM*.

5.3.1 Single Ramp Profiles

Figure 5-6 displays the emissions profiles for the fuel components for the downward load ramp cases, along with engine speed/load and equivalence ratio (λ). Transient effects are apparent, as experimental emissions vary significantly from quasi-steady predictions in most cases, although the degree of variance differs according to load profile and species. The emissions profiles for cyclohexane, ethanol and pentane are qualitatively similar in each case. For each of these species, the emissions at the onset of the load ramp drop for both the experimental values and quasi-steady predictions. However, the rate of decline is more significant for the experimental emissions, and the two profiles are significantly separated at the trough of the drop, as the error bars of the experimental emissions are outside of the area representing the stochastic effects of the quasi-steady emissions. Furthermore, while the experimental profiles eventually settle upward toward the quasi-steady values, the settling appears delayed by roughly a second after the conclusion of the load ramp. It is interesting to note that significant differences between transient emissions and quasi-steady predictions exist despite air-to-fuel ratio being maintained at near stoichiometric quantities throughout the load ramps, aside from the 1s load ramps which exhibit oscillations with a magnitude of approximately 0.05. Although it is difficult to speculate the exact causes and their relative contribution to these differences, some important transient effects can be listed. These include developing levels of residual exhaust gases within the engine cylinder (due to changing throttle positions and volumetric efficiency) and developing temperature levels.

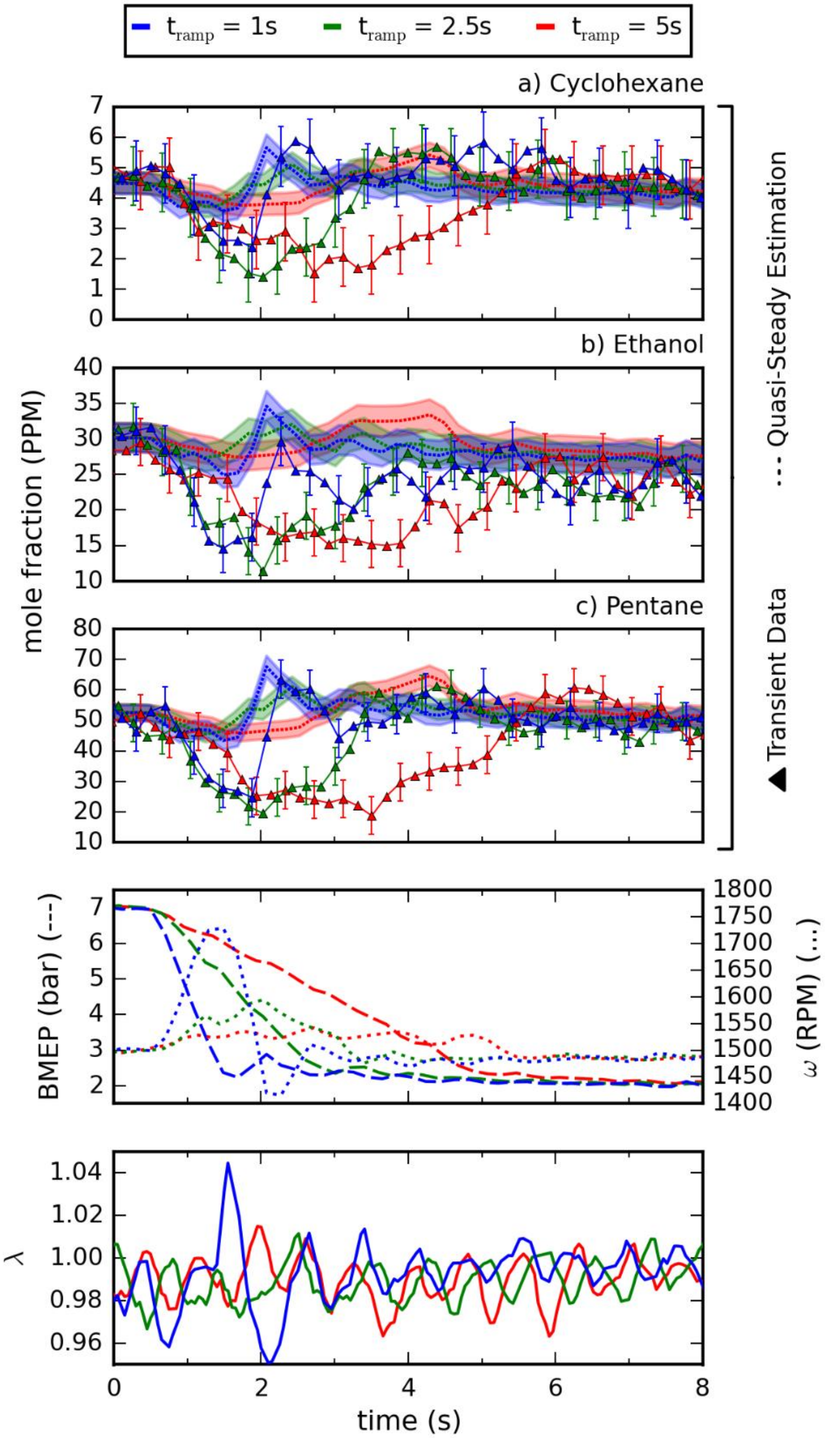

Figure 5-6: Emissions of various fuel components, engine speed/load and air-fuel equivalence ratio for the downward ramp load profile, 1500 rpm case. Error bars reflect the uncertainty standard deviation of a transient emissions estimation from a FTIR measurement. The shaded area surrounding the quasi-steady predictions represents the estimated standard deviation of stochastic emissions fluctuations for the current engine speed/load.

Shown in Figure 5-7 are the experimental emissions and quasi-steady predictions of the intermediate species for downward load ramp cases. Again, significant discrepancies exist between the two emissions profiles for certain species and load ramp rates. However, unlike the fuel component emissions which each display qualitatively similar profiles between species, considerable variability exists between the emissions of intermediate species. For acetylene and methane, a 1s load ramp causes a significant upward spike in emissions that exceeds the magnitude predicted by the quasi-steady model by a factor of about 2. This is followed by a brief downward spike whose level is captured relatively well by the quasi-steady model. For the 2.5 and 5s load ramp cases, a brief uptick in the emissions of acetylene and methane occur after the conclusion of the load ramp. The upticks appear statistically significant for both species, as the error bars of the estimated emissions lie outside of the shaded region surrounding the quasi-steady predictions, which represents the estimated magnitude of stochastic fluctuations. These upticks indicate a historical influence on emissions for these two species, since they occur after the end of the load ramp.

Experimental ethylene and formaldehyde emissions behave in an opposite manner as the quasi-steady predictions. The load ramp results in decreased emissions, while the quasi-steady model predicts an increase. Interestingly, ethylene emissions do not respond immediately to the load ramp. Instead, they remain relatively steady for about a second after the initiation of the load ramp, regardless of the ramp rate. For the 1s ramp case, there is a brief downward spike of about 10 ppm that occurs after the load ramp but before the engine speed settles. A similar downward spike is predicted in the quasi-steady model, although its magnitude is smaller (<5 ppm). The 2.5 ramp rate case also contains an initial brief downward spike followed by a steep upward ramp near the conclusion of the load ramp. Overall, the quasi-steady model fails to predict these downward spikes, and predicts an emissions rise that precedes that of the experimental data. It should be noted that ethane emissions (which are omitted for brevity) also display a similar lagging effect with respect to downward load ramps. Formaldehyde arguably displays the most interesting trend of all the species. For the 1s ramp case, the magnitude of the rise predicted by the quasi-steady model (~10 ppm) is equally matched by a descent in the experimental emissions. Furthermore, the spike in the experimental emissions precedes that of the quasi-steady predictions, and does not settle to its final value until about 5 seconds after the conclusion of the load ramp. It is also interesting to note that the trough of the descent aligns well with the peak air-to-fuel equivalence ratio. For the 2.5 and 5s load ramps, the experimental emissions gradually descend by about 5 ppm before rapidly ascending to their final, steady-state values at approximately 5 and 6 seconds, respectively. Interestingly, both of these rapid ascensions occur after their respective load ramps are finished, indicating a historical influence on formaldehyde emissions.

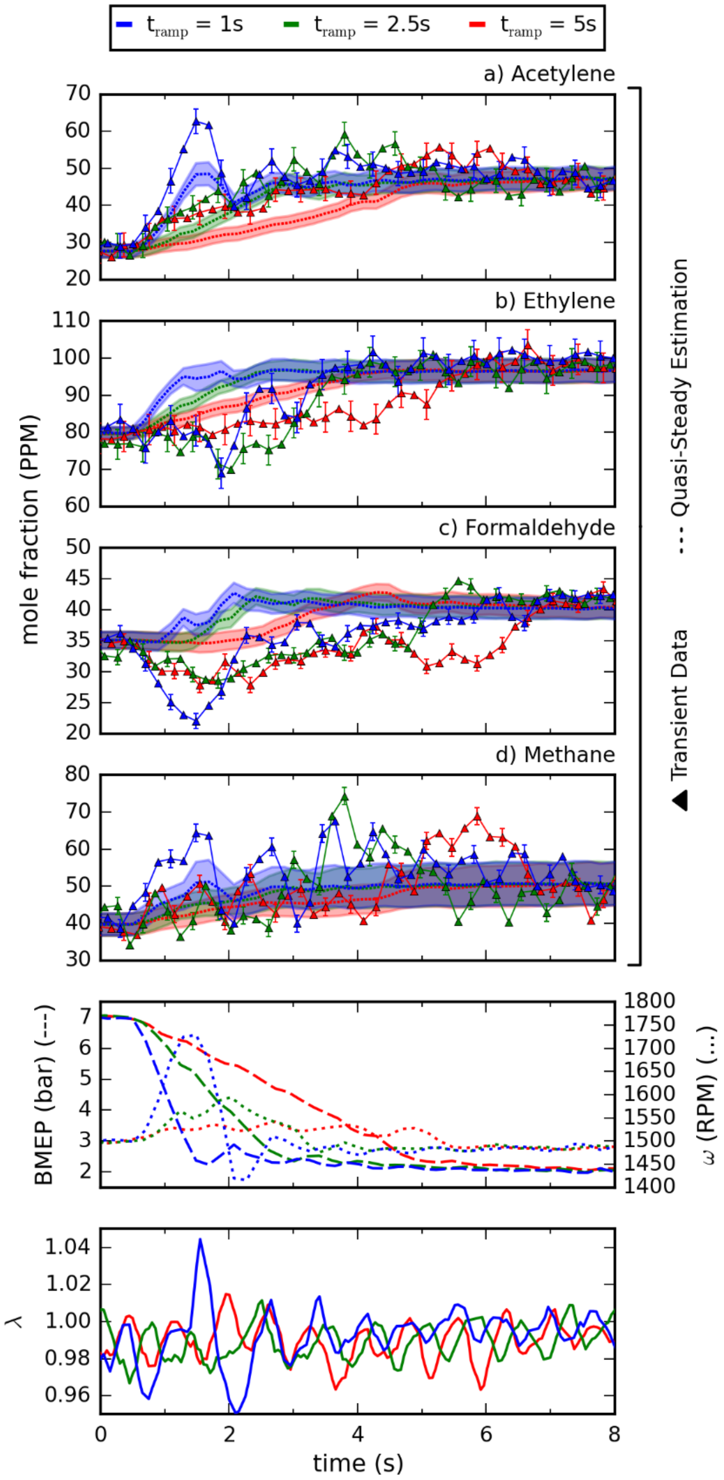

Figure 5-7: Emissions of various intermediates, engine speed/load and air-fuel equivalence ratio for the downward ramp load profile, 1500 rpm case. Error bars reflect the uncertainty standard deviation of a transient emissions estimation from a FTIR measurement. The shaded area surrounding the quasi-steady predictions represents the estimated standard deviation of stochastic emissions fluctuations for the current engine speed/load.

Figures 5-8 and 5-9 show emissions of fuel components and intermediates during the upward load ramps, respectively, along with engine speed/load and equivalence ratio. Overall, the discrepancies between the quasi-steady predictions and experimental emissions are moderate compared to the downward load ramp cases. However, significant disagreement persists for some species, particularly cyclohexane and pentane. As shown in Figure 5-8, the quasi-steady model underpredicts the magnitude of the cyclohexane and pentane spikes for both the 1 and 2.5s load ramps. Furthermore, the downward settling of the experimental emissions lag those of the quasi-steady model by at least half a second. Additionally, the peak of the experimental emissions of pentane for the 5s ramp case is greater than the peak of the quasi-steady model by a statistically significant quantity. The low end of the uncertainty of the experimental peak lies approximately 2 ppm above to the concurrent stochastic region of the quasi-steady prediction. It is interesting to note that the most significant lag between the experimental and predicted emissions occurs for the 2.5s ramp case for both cyclohexane and pentane; yet virtually no lag exists for the 5s ramp case. This indicates a complex historical effects on emissions, and suggests that a sophisticated model may be needed to accurately predict the emissions of species.

Experimental ethanol emissions generally agree with the quasi-steady predictions well for the upward load ramp cases. The initial emissions spikes during the load ramps are predicted well by the quasi-steady model, with only a few experimental points lying outside of one uncertainty standard deviation from quasi-steady region. The most glaring discrepancy occurs after the load ramps, as the experimental emissions settle at a composition that is several ppm greater than the quasi-steady prediction. This is likely not an error in the steady-state map. Recall that the final setpoint for the upward load ramps are the same as the initial setpoint for the downward ramps cases. In these former cases, the initial ethanol emissions agree well with the quasi-steady predictions. Another interesting feature of the transient emissions is that they remain slightly elevated following the upward load ramp, indicating historical effects.

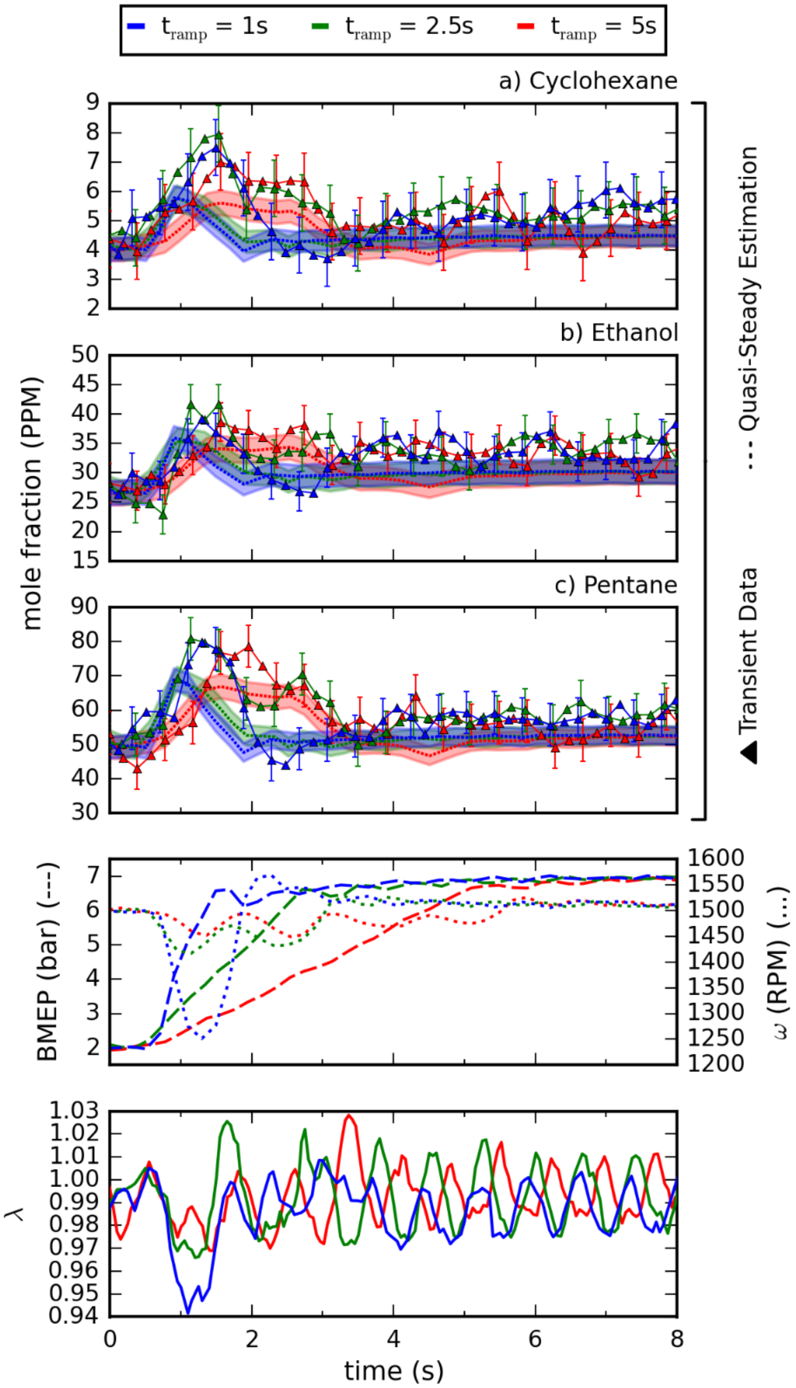

Figure 5-8: Emissions of various fuel components, engine speed/load and air-fuel equivalence ratio for the upward ramp load profile, 1500 rpm case. Error bars reflect the uncertainty standard deviation of a transient emissions estimation from a FTIR measurement. The shaded area surrounding the quasi-steady predictions represents the estimated standard deviation of stochastic emissions fluctuations for the current engine speed/load.

Shown in Figure 5-9 are the emissions profiles of the intermediate species for the upward load ramp cases. As in the downward load ramp cases, the profile for each intermediate species is relatively unique. For acetylene, the quasi-steady predictions agree reasonable well with the experimental emissions. The only glaring discrepancy occurs for 1s ramp case, where the experimental profile features an upward spike of approximately 7 ppm that begins nearly halfway through the load ramp, and doesn't settle back down until after the two second mark. An upward spike is absent in the quasi-steady predictions. Reasonable agreement exists between the quasi-steady predictions and experimental emissions for ethylene as well. For the 5s ramp case, each experimental emissions point is within one uncertainty standard deviation of the stochastic region for the quasi-steady predictions, indicating that the quasi-steady model is adequate for predicting ethylene composition at this load rate. The trough of the experimental emissions profile for the 2.5s ramp case lies just outside of one uncertainty standard deviation from the quasi-steady stochastic region. However, all remaining points lie sufficiently close to the quasi-steady predictions. The 1s load ramp is arguably the only case where the quasi-steady model yields significant error, as it underpredicts the magnitude of the emissions drop by roughly 5 ppm. However, when considering the experimental emissions uncertainty and stochastic effects, the true error may be as little as 1 or 2 ppm.

For formaldehyde, significant discrepancy exists between the quasi-steady and experimental emissions, although the degree of discrepancy is milder than that of downward step. The experimental emissions profile for the 1s ramp case consists of initial positive and negative spikes at approximately 1 and 1.75 seconds, respectively, followed by 5s period of high emissions. Interestingly, none of these features are predicted by the quasi-steady model. Similarly, the formaldehyde emissions for 2.5s and 5s load ramp cases contain numerous statistically significant oscillations during and after the load ramp that the quasi-steady model fails to predict. The most notable of these is the positive spike of ~10 ppm midway through load transient for the 5s ramp case. It is difficult to discern an obvious relationship between formaldehyde emissions and engine operation/equivalence ratio from this data, as emissions oscillations do not immediately appear to correspond to changes in load or speed in a consistent way. However, these complex emissions patterns are statistically significant and repeatable, indicating that they are indeed deterministic. Repeatability for formaldehyde emissions is demonstrated in Section 5.3.3.

Non-repeatable effects are apparent within the methane emissions, as the stochastic region surrounding the quasi-steady predictions spans 10 ppm at the initial load and the experimental emissions display substantial variation. However, a deterministic positive spike in methane emissions can be discerned near the end of the 1s load ramp. Furthermore, a significant portion of the emissions following the load ramp oscillate below the stochastic region surrounding the quasi-steady predictions. While the exact timing of these oscillations is not repeated in the other trial, the overall magnitudes are. This suggests that stochastic effects (or effects outside of engine speed and load) may be greater than initially estimated for methane for this load ramp. It is possible that the stochasticity statistics are also affected by historical engine speed/load, and that stochastic fluctuations temporarily increase in response to the rapid load ramp. For the other two load ramps, the experimental emissions appear mostly within the predicted regions by the quasi-steady model. However, for the 2.5s ramp case, two positive emissions spikes during the load transient exist that are substantially outside the region predicted by the quasi-steady model.

It also appears possible that these fluctuations may not be truly stochastic, but may be due to fluctuations in air-to-fuel ratio. As will be shown in the wave profile data, there is reason to believe that methane emissions are more sensitive to equivalence ratio than other species. More analysis is needed to elucidate the relationships between methane emission and air-to-fuel equivalence ratio and determine if there are correlations between the two.

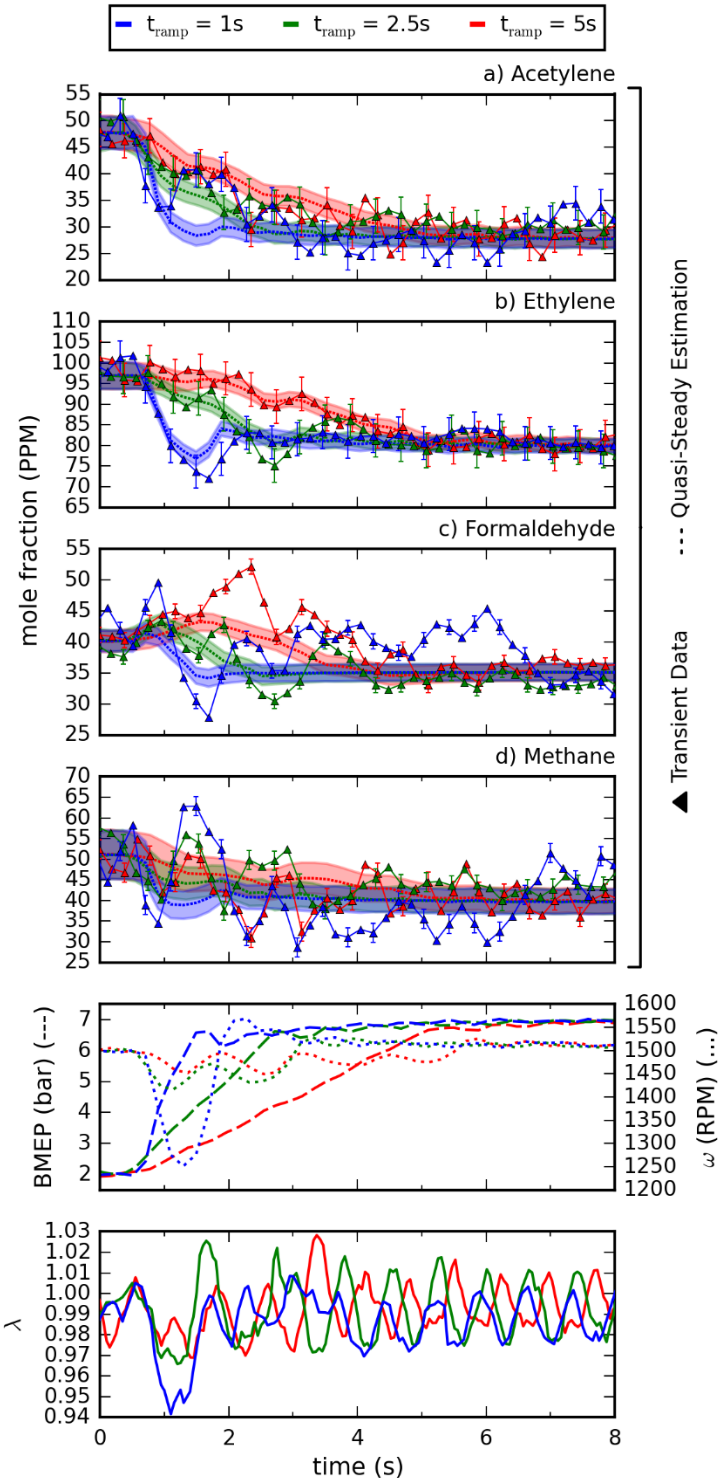

Figure 5-9: Emissions of various intermediates, engine speed/load and air-fuel equivalence ratio for the upward ramp load profile, 1500 rpm case. Error bars reflect the uncertainty standard deviation of a transient emissions estimation from a FTIR measurement. The shaded area surrounding the quasi-steady predictions represents the estimated standard deviation of stochastic emissions fluctuations for the current engine speed/load.

5.3.2 Wave Profiles

To determine if there are any long-term relationships between emissions and engine load that are not discernable from single load ramp experiments, experiments with load ramp waves are conducted. As in the single load ramp experiments, emissions of fuel components and intermediates are presented separately, which are shown in Figures 5-10 and 5-11, respectively. For clarity, only the experimental emissions are presented and error bars are removed. No long-term trends are easily discernable in the emissions for any fuel component or intermediate species, as the emissions trends appear relatively stationary throughout each cycle. This suggests that historical effects on emissions, while significant as evidenced from the single load ramp experiments, do not extend beyond several seconds. This is important information for future emissions models, as it suggests an approximate limit on the amount of historical data needed to properly train or develop these models.

For the most part, emissions during the wave load ramps behave as expected given the data from the single load ramps. However, some subtle differences exist. For example, the cyclohexane composition peaks during the 1s load ramp waves are consistently greater than those of the other ramp rates by roughly a ppm, although differences often lie within the uncertainty. Conversely, the peaks of the cyclohexane emissions during the single upward load ramps are all within a ppm. For cyclohexane, ethanol and pentane during the 2.5 and 5s ramp waves, the emissions display an interesting pattern where a peak is reached midway through the upper load ramp, followed by a steady, modest drop that is capped off with an upward inflection at the end of the ramp. Furthermore, as the emissions begin to drop during the downward load ramp, the trough is reached well before the load ramp's end. In the context of the results for the single upward and downward load ramps, these results make sense. Recall that cyclohexane and ethanol emissions during the single upward load ramp also contain an early peak followed by a temporary downward inflection, while the downward load ramp results in an early trough that occurs just midway through the load ramp. Arguably the only profound difference is that for the 5s load ramp, the inflection for the cyclohexane emissions during the load waves are greater than that of the single upward load ramp.

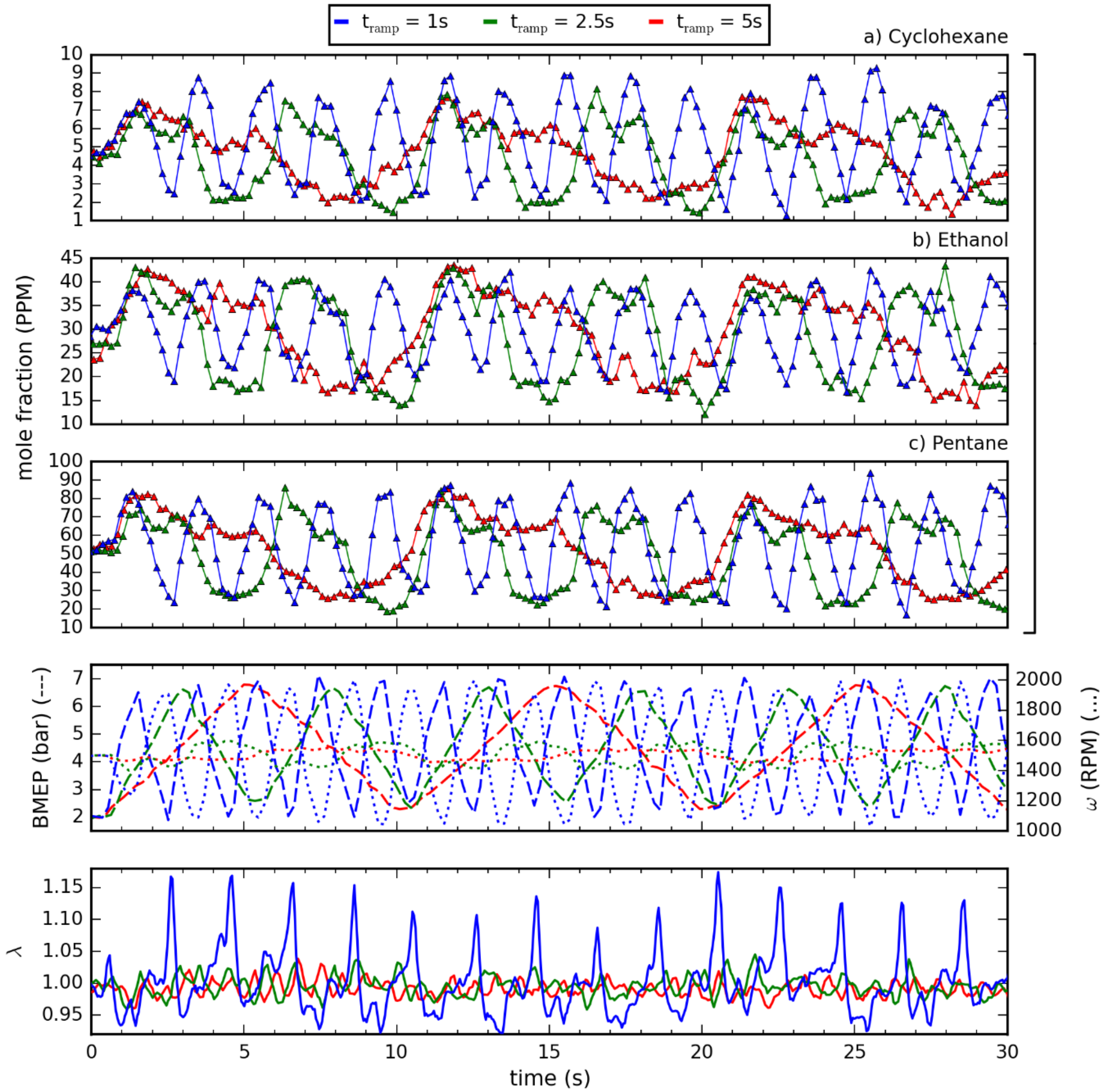

Figure 5-10: Emissions of various fuel components, engine speed/load and air-fuel equivalence ratio for the wave load profile, 1500 rpm case.

Overall, emissions of intermediate species appear to display greater stochasticity than the fuel components emissions for the wave load profiles, although some general relationships with engine parameters can still be perceived. Acetylene emissions behave mostly as expected given the single load ramp cases, as emissions peaks correspond to load troughs and vice versa. However, moderate dips followed by steep upward spikes are observed following the emissions peaks for the 2.5s ramp case. This contradicts the single upward load ramp case where the emissions fall relatively steadily. These oscillations may be caused by a historical effect from the previous downward load ramp. As in the single load ramp experiments, ethylene emissions display interesting patterns that contrast the emissions of other intermediate species. The dc component (or average) of the ethylene emissions during the wave load profiles drops as the load ramp rate increases. Average composition for the 1s and 5s load ramps are approximately 75 and 85 ppm, respectively. This is due to the lagged response of ethylene emissions to downward load ramps, as illustrated earlier in Figure 5-7. Ethylene emissions drop due to the initial upward load ramp, and remain at/near the trough for the remainder of the wave profile, as emissions fail to rise during the downward load ramp. Interestingly, this effect is more pronounced for the shorter load ramps, revealing a historical effect that is not observed in the data from the single load ramps. While the overall emissions profiles appear somewhat correlated to load for the 2.5 and 5s ramp cases, there are many oscillations that appear stochastic. The emissions for the 1s ramp case are dominated by stochastic fluctuations, as many of the peaks and troughs do not correspond to specific points in the speed/load profiles. It should also be noted that ethane emissions, while present in smaller quantities (~10 ppm), also display similar trends.

Formaldehyde emissions, as illustrated in the single load ramp results, have a complicated relationship with engine parameters. However, the emissions profile for the 1s load ramp case displays a simple wave pattern, although amplitude of the wave is 5-10 ppm lower than expected given the single load ramp data. The emissions profile for the 2.5s case displays a complicated, albeit repeatable pattern consisting of two moderate spikes surrounding a central, significant upwards spike. The emissions for the 5s ramp case make the most sense in the context of the single load ramp data, as peaks occur midway through the upward load transient, and emissions are relatively constant during the downward load transient. While deterministic patterns are present in formaldehyde emissions, clearly a complex model is needed to predict them. Interestingly, the methane emissions for the 1s ramp wave case have values that far exceed that of the single step cases. Some of the methane peaks reach compositions greater than 90 ppm, while 65 ppm is the maximum reached for either of the single load ramp cases. Coincidentally, air-to-fuel equivalence ratio peaks reach much higher values during the wave ramps (~1.15) than for the single step load ramps (~1.05). Spikes in methane emissions and equivalence ratio also happen to coincide in time. This, along with repeated fluctuations in the methane emissions with similar frequencies as equivalence ratio oscillations, suggest that methane emissions may be more sensitive to air-to-fuel ratio than other species. For the other two load ramp rates, stochasticity appears dominant as fluctuations seem uncorrelated with changes in engine parameters.

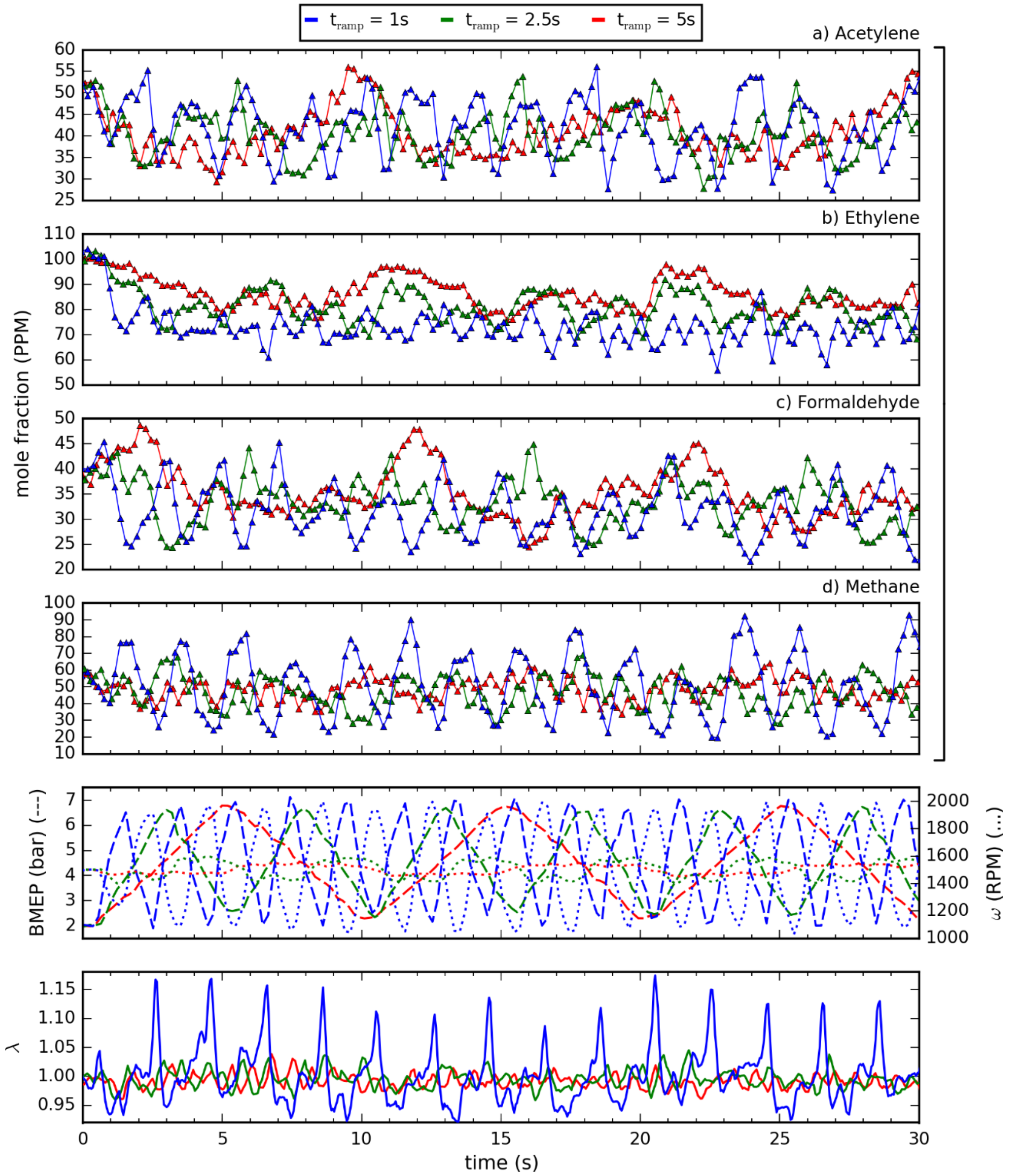

Figure 5-11: Emissions of various intermediates, engine speed/load and air-fuel equivalence ratio for the wave load profile, 1500 rpm case.

The standard error between the experimental emissions and quasi-steady predictions for each species during the wave load ramp profiles are plotted in Figure 5-12. To determine if the quasi-steady prediction errors are statistically significant, the estimated stochasticity standard deviation and experimental emissions standard uncertainty are also plotted for each species and load profile. Reduced chi-square statistics for the deviations between experimental and predicted emissions relative to stochasticity and uncertainty statistics are calculated for each case and presented above their corresponding bars in Figure 5-12. Higher chi-square statistics corresponds to higher likelihood that there are deterministic discrepancies between experimental and predicted emissions, and that these discrepancies are due to transient effects, as opposed to noise and random fluctuations. As seen from the figure, the standard prediction errors are greater than standard uncertainty and stochasticity in all cases, suggesting that transient and historical effects indeed influence emissions in a compelling way. Chi-square statistics are greater than 3.84 (which corresponds to 95% confidence) in 14 of the 21 cases, with the exceptions being all the cyclohexane cases, ethanol at 1s load ramps, acetylene at 2.5 and 5s load ramps, and ethylene at 5s load ramps. Cyclohexane emissions are contained within single digits in every load profile. At such small quantities, deterministic fluctuations are expected to rival uncertainty. The remaining exceptions are consistent with the overall tendencies observed in the data, which are discussed below.

For the intermediate species, quasi-steady prediction error increases as load ramp rate increases. It is anticipated that the magnitude of transient effects should scale with load ramp rate. However, for all the fuel component species, the quasi-steady model performs the poorest for the 2.5s load ramp, and the best for the 1s ramp. It is difficult to speculate as to why the 2.5s ramps yield the greatest deviation between experimental emissions and quasi-steady predictions for fuel components. One possible explanation is that for the faster ramps, historical effects have insufficient time to fully materialize, yielding emissions that are closer to the average values. Nevertheless, these results indicate that there are indeed transient, deterministic effects on VOC emissions during speed and load changes, suggesting that the emissions of these species can be predicted with a sufficiently complex model. It should be noted that some of the quasi-steady prediction error may be attributed to additional stochasticity introduced by the load ramps. For example, the methane emissions for the 1s single load ramp cases appear more stochastic than predicted by the stochasticity from the quasi-steady model. Coincidentally, the greatest quasi-steady prediction error is for methane for the 1s load ramp case. However, this additional stochasticity is likely only consequential for a few species and load profiles, as most of the statistically significant deviations in this study are repeatable, as discussed and illustrated in the next subsection.

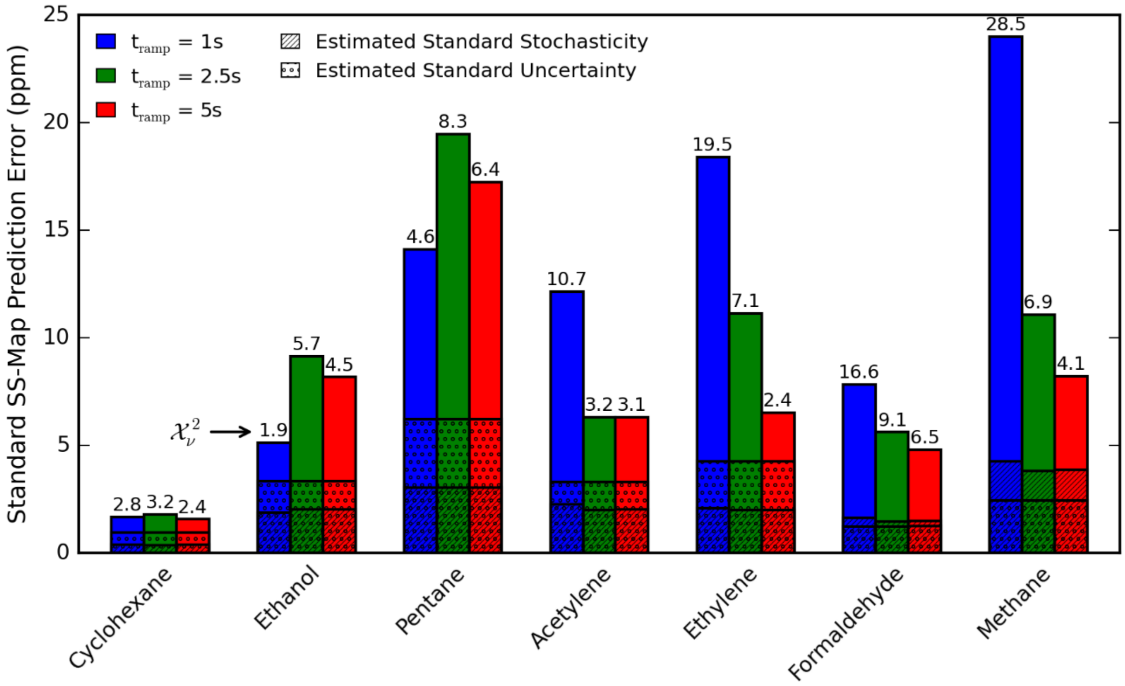

Figure 5-12: Standard error between experimental emissions and quasi-steady predictions for various species and profiles, compared with estimated standard deviation of stochastic fluctuations, as well as standard uncertainty of experimental emissions for the wave profile, 1500 rpm cases. Calculated reduced chi-square statistics lie above each bar, indicating the statistical significances of quasi-steady prediction errors relative to stochasticity and uncertainty.

5.3.3 Repeatability

To demonstrate the repeatability of some of the deterministic fluctuations identified in the experimental emissions, formaldehyde emissions from both trials for each upward, downward and wave load ramp case are presented in Figure 5-13. Formaldehyde is chosen for this purpose as experimental formaldehyde emissions contain frequent fluctuations that contradict the quasi-steady model, some of which appear completely uncorrelated to engine conditions at first glance. Thus, repeatability improves confidence that these discrepancies are indeed deterministic and due to transient effects. Also, the quality of repeatability in formaldehyde emissions is similar to that of the other species aside from the stochastic methane fluctuations identified earlier. Repeatability is apparent in all the initial fluctuations at the onset of the load transients. For the upward, 1s load ramp, the initial upward and downward oscillations for the two trials practically overlap one another in this region, as do the initial emissions drops for the downward 1s load ramp. The spike near 2 seconds for the 5s upward load ramp is also repeated in each trial, although the magnitudes of the spikes disagree by a few ppm. Even the intricate patterns in the 2.5s ramp wave profile are repeated, such as the brief uptick near 2 seconds. The only aspect where repeatability is not observed is in the timing at which long-term emissions fluctuations settle to their final, steady values. For example, the emissions profile for the 1s, upward load ramp begins descending toward its final value near 6 seconds for the first trial, while the emissions remain near 45 ppm past the 8 second window for the second trial. A similar, less dramatic discrepancy in settling time exists for the 5s downward load ramp case. This difference in settling time is unique to formaldehyde, and its cause may be stochastic and/or difficult to predict given conventional engine data such as load, speed and equivalence ratio.

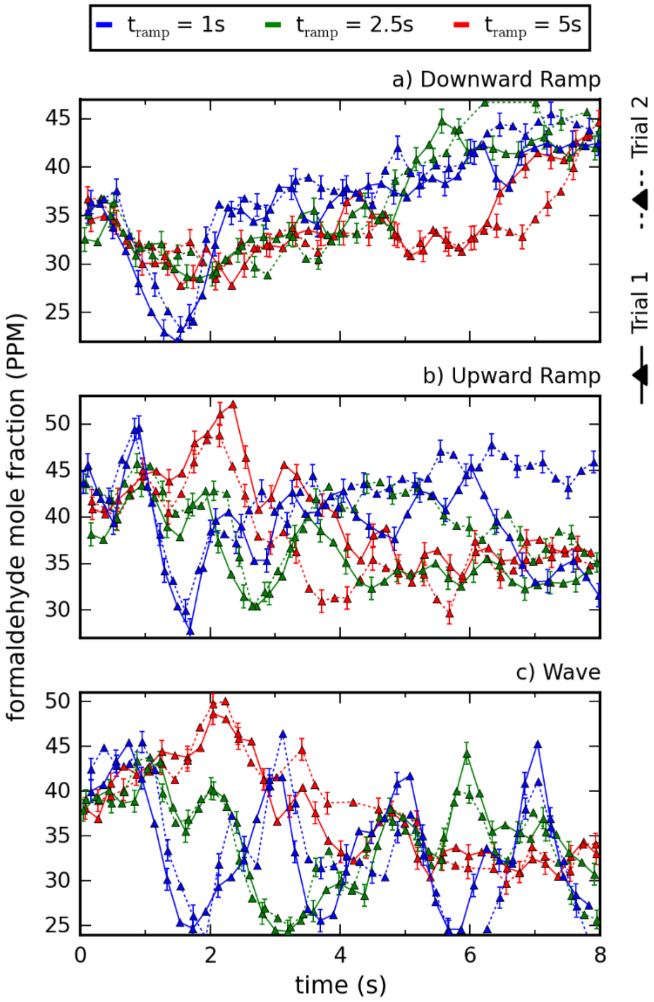

Figure 5-13: Emissions of formaldehyde from the first and second trials for the upward, downward and wave ramp load profiles for the 1500 rpm case. Error bars reflect the uncertainty standard deviation of a transient emissions estimation from a FTIR measurement.

5.3.4 1,3 Butadiene, Benzene and Toluene Emissions

The emissions of 1,3 butadiene, benzene and toluene are notably absent from the analysis above, despite the fact that each of these species are identified as toxins by the California Air Resources Board [105]. While these species are indeed measured in this work, 1,3 butadiene emissions are completely dominated by stochasticity and minimally influenced by engine load, while measurement noise and low compositions prevent a legitimate analysis of benzene and toluene emissions. The chaotic measurements obtained for benzene and toluene are corroborated by the Monte-Carlo analysis for estimating measurement noise presented in Section 5.2.2. Estimated measurement noise variances for benzene and toluene are 78.5 and 63.6 PPM, respectively. For reference, the next highest measurement noise variance is 10.6 PPM for pentane, while the remaining species lie between 0.3 and 6.5 PPM (see Table S1 in the supporting information). The exacerbated noise of these species are caused by a combination of low absorptivity, low concentration, and the strong presence of highly interfering major combustion products. To illustrate this point, the analysis absorption spectra of toluene and benzene at 18.63 and 93.17 ppm (the lowest calibrated compositions), respectively, are presented in Figure 5-14 along with the absorption spectra of carbon dioxide and water at typical compositions within combustion products. First, it is shown that moderate compositions of these species produce modest absorbances (<<0.05) that are somewhat comparable to noise levels. To worsen the problem, the analysis spectra of these species are almost completely engulfed by the absorbance spectra of water and/or carbon dioxide. As absorbance increases in a spectral region, the power of the available signal diminishes, increasing the relative effects of noise. Thus, the presence of these major combustion products further reduces the fidelity of benzene and toluene measurements. While benzene and toluene measurements are impaired for the low compositions encountered in this work, it should be mentioned that FTIR measurements of these species remain valid at higher quantities.

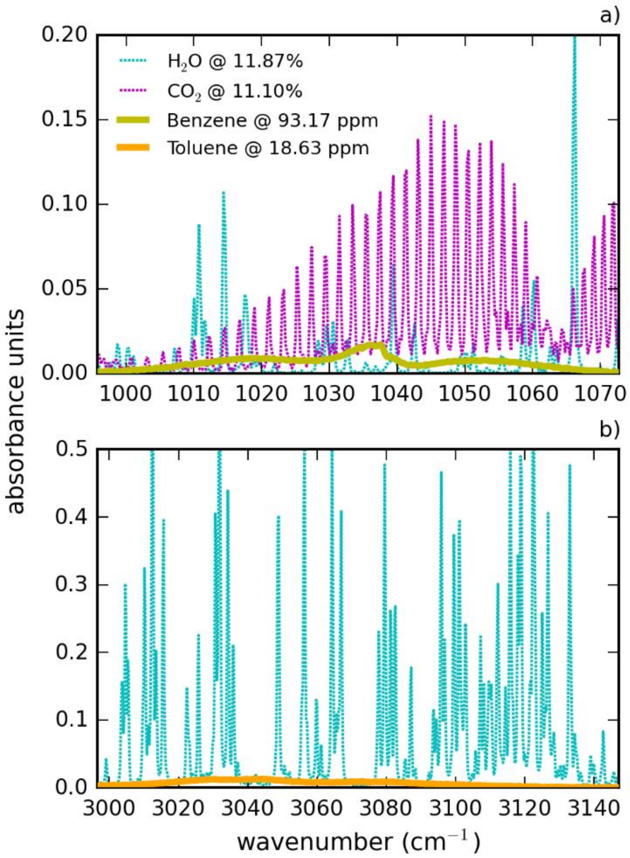

Figure 5-14: Calibrated spectral absorbances for a) benzene at a composition of 93.17 ppm and b) toluene at a composition of 18.63 compared to absorbance spectrums of water and carbon dioxide at compositions that are typical within combustion products.

Shown in Figure 5-15 are 1,3 butadiene emissions for the upward, downward and wave load ramp profiles, along with error bars located near 1s which represent the standard uncertainty for the experimental emissions throughout each experiment. Clearly, any deterministic relationships between 1,3 butadiene emissions and engine load are overshadowed by stochasticity and obscured by high measurement noise as indicated by the sizeable uncertainty error bars. The standard deviation of stochastic component of 1,3 butadiene emissions is predicted to cover a span of approximately 2 ppm, which mirrors the fluctuations observed in the experimental emissions during the transient load profiles and eclipses the predicted deterministic changes in emissions due to load (~1 ppm). However, it is somewhat difficult to differentiate between stochastic vs. deterministic components of emissions due to elevated uncertainty standard deviations, which cover a span of approximately 4 ppm. Thus, unlike the species presented previously, it’s difficult to form conclusions about the 1,3 butadiene emissions patterns with respect to load with high confidence. However, it should also be noted that the composition range covered by the experimental emissions (including uncertainty) spans around 10 ppm, which is modest. Thus, it can be said with a moderate degree of confidence that 1,3 butadiene emissions are overall relatively unaffected by engine speed and load compared to other species (aside from cyclohexane).

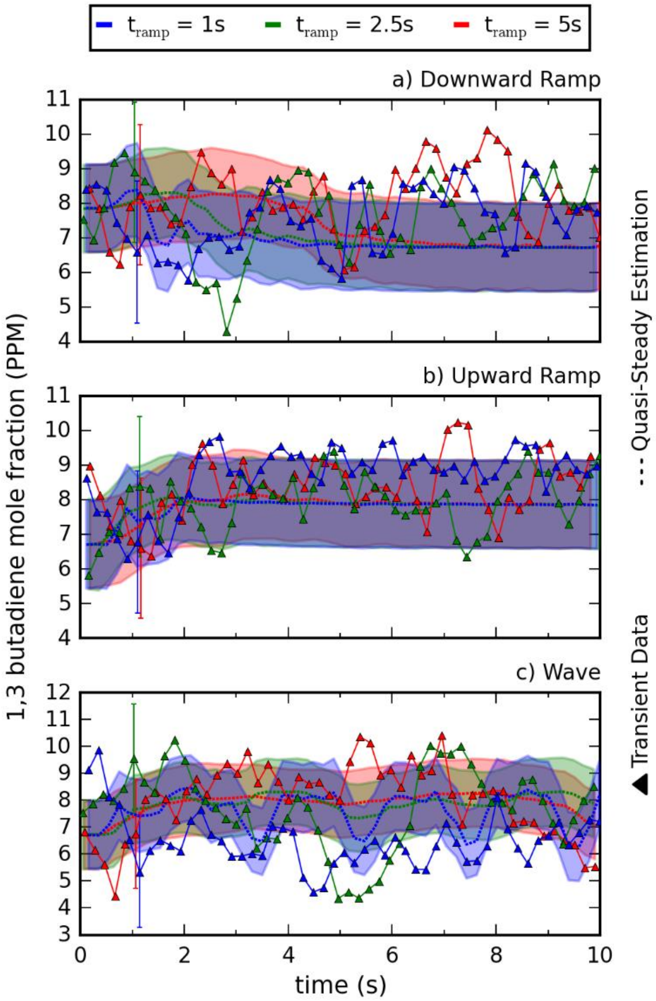

Figure 5-15: Emissions of 1,3 butadiene for the upward, downward and wave ramp load profiles for the 1500 rpm case. Error bars reflect the uncertainty standard deviation of a transient emissions estimation from a FTIR measurement. The shaded area surrounding the quasi-steady predictions represents the estimated standard deviation of stochastic emissions fluctuations for the current engine speed/load.

5.4 Chapter Summary

Emissions of various fuel component and reaction intermediate VOCs from a 1.5L Kubota WG1605 four-cylinder, port fuel-injected, spark-ignited engine are measured for a collection of transient load profiles. These load profiles consist of single upward and downward load ramps and waves spanning durations of 1, 2.5 and 5 seconds. Emissions are measured using FTIR spectroscopy, and measurements are processed with a previously developed UKF to mitigate the biasing effects of sample recirculation and signal non-stationarity. These emissions estimations are compared to predictions from a quasi-steady model - which predicts emissions according to the current engine speed/load – and estimated magnitudes of the stochastic component of emissions fluctuations. The data shows that emissions during speed/load transients generally deviate from quasi-steady predictions to a degree that cannot be explained by stochasticity and/or equivalence ratio fluctuations alone, indicating that transient effects such as speed/load history significantly influence VOC emissions. Conclusions from this study are summarized in the following bullet point list.

- Greater deviations between the quasi-steady predictions and experimental emissions occur for the downward load ramp cases compared to upward ramps for all species, with deviations higher than 2, 10 and 30 ppm encountered during the downward load ramps for cyclohexane, ethanol and pentane, respectively. The quasi-steady model predicts upward fluctuations during the load ramps for these species, while the experimental emissions drop significantly.
- Emissions of the fuel components cyclohexane, ethanol and pentane are well correlated with one another, displaying peaks/troughs at similar times.
- Intermediate species display greater variations in their responses to load transients. Formaldehyde possesses the most complicated, albeit deterministic relationship with engine conditions during transients, as multiple emissions fluctuations emerge that result in quasi-steady prediction errors as high as 15 ppm. Ethylene emissions display unique characteristics that include a lagged response to downward load ramps by several seconds. This characteristic is shared by ethane emissions, which are unreported.
- For the wave profiles, standard quasi-steady prediction errors surpass the combined effects of stochasticity and uncertainty by statically significant quantities (p>95%) in 14 out of 21

cases according to reduced chi-square statistics. This indicates the presence of transient and historical effects on VOC emissions.

- Steeper load ramps result in greater quasi-steady prediction error for intermediate species. Interestingly, moderate ramp rates (the 2.5s ramp cases) result in the greatest deviation for cyclohexane, ethanol and pentane.
- Conclusions cannot be formed for benzene and toluene due to low quantities and excessive measurement noise.
- 1,3 butadiene emissions are affected minimally by engine load/speed and appear dominated by stochasticity.

Since VOC emissions are shown to be influenced by transient effects in a deterministic fashion, future work should entail developing a model to predict these emissions, which could play a key role in answering the question of whether control methods can be implemented to mitigate selective VOCs. However, this works shows that relationships between engine parameters and emissions are complicated; and the elucidation of these relationships may require a machine learning method (such as a neural network) or a detailed consideration of engine physics.

CHAPTER 6 DISSERTATION SUMMARY

This dissertation details the development, validation and application of a UKF for filtering FTIR measurements of VOC emissions during transient engine operation. Anthropogenic VOC emissions, which lead to tropospheric ozone formation and contribute to the greenhouse effect, are comprised largely of engine exhaust. While FTIR spectroscopy is a critical technique for speciating VOC emissions from engines, it is susceptible to biasing effects when emissions are non-steady, impairing its applicability to studying emissions during practical, realistic engine operation. These biasing effects include sample recirculation within a FTIR gas cell, which effectively reduces the time-resolution of measured emissions profiles due to historical influences on current FTIR measurements. This issue motivates the development of the UKF, which addresses sample recirculation by estimating the instantaneous gas cell inlet composition according to the evolution of FTIR measurements. The UKF utilizes a simple model of the mixing dynamics within the gas cell, as well as measurement noise and inlet composition fluctuation statistics to achieve its estimations. A second biasing effect of transient FTIR measurements is identified in this work: non-stationarity. Non-stationarity refers to the evolution of the spectral power of the IR beam during a FTIR scan due to changing concentrations within the gas cell. The resulting calculated IR spectrum from such a measurement is heavily weighted by the true IR intensity at/near the centerburst location. Coupled with the alternating scanning directions of the FTIR moving mirror, non-stationarity produces artificial oscillations in measured emissions profiles. The original UKF is augmented to account for centerburst weighting to deduce the true gas cell compositions corresponding to biased FTIR measurements. With the UKF fully formulated to combat both biasing effects, it is utilized to study transient effects on VOC emissions from a spark-ignited, port fuel-injected engine during transient load sequences. This study reveals that transient effects are indeed substantial, as deviations between experimental emissions and quasi-steady predictions exceed the estimated contributions of stochastic emissions fluctuations. The findings presented in each chapter are summarized in greater detail in the remaining paragraphs.

In Chapter 3, the original UKF for addressing sample recirculation is developed. The UKF’s equations and specific sub-models pertaining to FTIR measurements are introduced. CFD and MN models are used to rigorously simulate the mixing dynamics within the FTIR gas cell to evaluate the fidelity of the well-mixed sub-model within the UKF. The well-mixed model is shown to adequately represent the relationship between inlet and gas cell composition to allow accurate estimations of inlet composition. Synthetic NO emissions are generated for the FTP driving cycle using an emissions model, and corresponding FTIR measurements with various noise levels are simulated using total gas cell composition calculations from the MN model. These NO measurements are filtered with the UKF, which is shown to improve emissions estimations by 38.4%, 18.9%, 4.9% and 6.2% for measurement noise standard deviations of 10, 20, 40 and 80 ppm, respectively, compared to unfiltered FTIR measurements for a sample flow rate of 25 lpm. It is also demonstrated that greater sample flow rate reduces residence times, resulting in improved estimations.

The effects of non-stationarity on FTIR measurements and the ensuing adaptations of the UKF are the focus of Chapter 4. First, period-dependent patterns in FTIR measurements of transient concentrations of acetylene and propylene are identified, with these patterns being more apparent for propylene measurements. The Fourier transform of a length power signal (i.e. synthetic interferogram) composed from a uniform, finitely broadened spectrum with linearly evolving power is derived. This calculation reveals that the Fourier transform weighs spectra at/near the centerburst location more heavily than those at further OPDs, with the degree of weighting scaling with spectral broadening width. Centerburst weighting is proposed as the cause of the period-dependent oscillations in FTIR measurements. This analysis is extended to practical FTIR measurements to determine unique values of centerburst weighting for individual species using their calibrated absorption spectra. These calculations for centerburst weighting are incorporated into the UKF, and the fidelity of these modifications are validated using measurements of transient acetylene and propylene compositions. The modified UKF is shown to improve estimations of acetylene and propylene composition for various transient profiles by 58% and 51% on average, respectively, compared to unfiltered FTIR measurements. These profiles consist of composition fluctuations of 0.5Hz or 1.25Hz. The UKF yields greater relative improvement for faster composition changes, due lagging effects in the measurements. Lagging effects are shown to be more prevalent in propylene measurements, due to greater effective aliasing from elevated centerburst weighting.

In Chapter 5, the UKF is utilized to study transient emissions of various fuel component and intermediate species from a spark-ignited, port fuel-injected gasoline engine under transient operation. Experimental emissions during upward, downward and alternating load ramps – which are determined by filtering FTIR measurements with the UKF – are shown to differ from steady-state map predictions by a magnitudes that exceed estimated stochastic fluctuations, indicating the presence of significant transient effects on VOC emissions. Downward load ramps yield the greatest deviations from predicted emissions compared to other profiles, with differences for cyclohexane, ethanol and pentane surpassing 2, 10 and 30 ppm, respectively. Transient emissions for the fuel components are shown to be highly correlated, while the emissions profiles displayed by intermediate species acetylene, ethylene, formaldehyde and methane are unique. Formaldehyde emissions arguably possess the most intricate relationship with engine operation, as frequent emissions fluctuations emerge during and after load transients that yield quasi-steady prediction errors as high as 15 ppm. Of the 21 combinations of species/wave load profiles explored in this study, emissions from 14 deviate from quasi-steady predictions in a statistically significant manner according to reduced chi-squared statistics. The cases of insignificant deviation consist primarily of intermediate species at gradual load ramps and fuel components at steep load ramps. 1,3 butadiene emissions are shown to be minimally affected by engine speed/load, while benzene and toluene measurements are dominated by noise.

Future work motivated by this dissertation includes addressing the three simplifying assumptions invoked in the calculations of centerburst weighting for FTIR measurements outlined near the end of Chapter 4. While these assumptions permit a clear, tractable derivation of centerburst weighting for practical FTIR measurements using existing calibrations, they could lead to errors in cases of significant absorbance evolution, non-constant absorptivity and significant spectral interference. Chapter 5 clearly indicates the presence of transient effects on VOC emissions. This work could be extended by identifying, quantifying and modelling these effects with the ultimate purpose of determining if control and/or design strategies for reducing the emissions of selective VOCs are possible. The procedures executed in this work can also be applied to other engines and transient load profiles. Such a study would be especially interesting if applied to advanced combustion strategies such as gasoline direct injection, which is known to emit elevated quantities of VOCs [106].

BIBLIOGRAPHY

[1] U.S. Environmental Protection Agency, “Technical Overview of Volatile Organic Compounds.” [Online]. Available: https://www.epa.gov/indoor-air-quality-iaq/technical-overview-volatile-organic-compounds#2. [Accessed: 15-Aug-2018].

[2] R. Atkinson, “Atmospheric chemistry of VOCs and NO(x),” *Atmos. Environ.*, vol. 34, no. 12–14, pp. 2063–2101, 2000.

[3] W. Chiemchaisri, C. Visvanathan, and S. W. Jy, “Effects of trace volatile organic compounds on methane oxidation,” *Brazilian Arch. Biol. Technol.*, vol. 44, no. 2, pp. 135–140, 2001.

[4] K. S. Carslaw, O. Boucher, D. V. Spracklen, G. W. Mann, J. G. L. Rae, S. Woodward, and M. Kulmala, “Atmospheric aerosols in the earth system: a review of interactions and feedbacks,” *Atmos. Chem. Phys. Discuss.*, vol. 9, no. 3, pp. 11087–11183, 2009.

[5] J. L. Jimenez, M. R. Canagaratna, N. M. Donahue, A. S. H. Pŕ ev̂ ot, Q. Zhang, J. H. Kroll, P. F. DeCarlo, J. D. Allan, H. Coe, N. L. Ng, A. C. Aiken, K. D. Docherty, I. M. Ulbrich, A. P. Grieshop, A. L. Robinson, J. Duplissy, J. D. Smith, K. R. Wilson, V. A. Lanz, C. Hueglin, Y. L. Sun, A. Laaksonen, T. Raatikainen, J. Rautiainen, P. Vaattovaara, M. Ehn, M. Kulmala, J. M. Tomlinson, D. R. Collins, M. J. Cubison, E. J. Dunlea, J. A. Huffman, T. B. Onasch, M. R. Alfarra, P. I. Williams, K. Bower, Y. Kondo, J. Schneider, F. Drewnick, S. Borrmann, S. Weimer, K. Demerjian, D. Salcedo, L. Cottrell, R. Griffin, A. Takami, T. Miyoshi, S. Hatakeyama, A. Shimono, J. Y. Sun, Y. M. Zhang, K. Dzepina, J. R. Kimmel, D. Sueper, J. T. Jayne, S. C. Herndon, A. M. Trimborn, L. R. Williams, E. C. Wood, C. E. Kolb, U. Baltensperger, and D. R. Worsnop, “Evolution of Organic Aerosols in the Atmosphere: A New Framework Connecting Measurements to Models,” *Science (80-.).*, vol. 326, no. December, pp. 1525–1529, 2009.

[6] E. G. Olumayede, “Atmospheric Volatile Organic Compounds and Ozone Creation Potential in an Urban Center of Southern Nigeria,” *Int. J. Atmos. Sci.*, vol. 2014, no. x, pp. 1–7, 2014.

[7] R. Atkinson, *Kinetics and Mechanisms of the Gasphase Reactions of the Hydroxyl Radical with Organic Compounds*. American Chemical Society, 1989.

[8] R. G. Derwent, M. E. Jenkin, and S. M. Saunders, “Photochemical ozone creation potentials for a large number of reactive hydrocarbons under European conditions,” *Atmos. Environ.*, vol. 30, no. 2, pp. 181–199, 1996.

[9] R. G. Derwent, M. E. Jenkin, S. M. Saunders, and M. J. Pilling, “Photochemical ozone creation potentials for organic compounds in northwest Europe calculated with a master chemical mechanism,” *Atmos. Environ.*, vol. 32, no. 14–15, pp. 2429–2441, 1998.

[10] T. M. Butler, M. G. Lawrence, D. Taraborrelli, and J. Lelieveld, “Multi-day ozone production potential of volatile organic compounds calculated with a tagging approach,” *Atmos. Environ.*, vol. 45, no. 24, pp. 4082–4090, 2011.

[11] M. Kampa and E. Castanas, “Human health effects of air pollution,” *Environ. Pollut.*, vol.

151, no. 2, pp. 362–367, 2008.

[12] A. R. Crebelli, F. Tomei, A. Zijno, S. Ghittori, M. Imbriani, D. Gamberale, A. Carere, R. Crebelli, F. Tomei, A. Zijno, S. Ghittori, M. Imbriani, D. Gamberale, A. Martini, and A. Carere, "Exposure to Benzene in Urban Workers : Environmental and Biological Monitoring of Traffic Police in Rome Exposure to benzene in urban workers : environmental and biological monitoring of traffic police in Rome," *Occup. Environmetal Med.*, vol. 58, no. 3, pp. 165–171, 2016.

[13] H. Bahadar, S. Mostafalou, and M. Abdollahi, "Current understandings and perspectives on non-cancer health effects of benzene: A global concern," *Toxicol. Appl. Pharmacol.*, vol. 276, no. 2, pp. 83–94, 2014.

[14] L. J. Bloemen, A. Youk, T. D. Bradley, K. M. Bodner, and G. Marsh, "Lymphohaematopoietic cancer risk among chemical workers exposed to benzene," *Occup. Environ. Med.*, vol. 61, no. 3, pp. 270–274, 2004.

[15] U.S. Environmental Protection Agency, "U.S. EPA. Health Assessment of 1,3-Butadiene," Washington, D.C., 2002.

[16] U.S. Environmental Protection Agency, "Profile of version 1 of the 2014 National Emissions Inventory," 2017. [Online]. Available: https://www.epa.gov/sites/production/files/2017-04/documents/2014neiv1_profile_final_april182017.pdf. [Accessed: 01-Jun-2017].

[17] D. D. Parrish, W. C. Kuster, M. Shao, Y. Yokouchi, Y. Kondo, P. D. Goldan, J. A. de Gouw, M. Koike, and T. Shirai, "Comparison of air pollutant emissions among mega-cities," *Atmos. Environ.*, vol. 43, no. 40, pp. 6435–6441, 2009.

[18] S. G. Brown, A. Frankel, and H. R. Hafner, "Source apportionment of VOCs in the Los Angeles area using positive matrix factorization," *Atmos. Environ.*, vol. 41, no. 2, pp. 227–237, 2007.

[19] A. K. H. Lau, Z. Yuan, J. Z. Yu, and P. K. K. Louie, "Source apportionment of ambient volatile organic compounds in Hong Kong," *Sci. Total Environ.*, vol. 408, no. 19, pp. 4138–4149, 2010.

[20] Y. Song, M. Shao, Y. Liu, S. Lu, W. Kuster, P. Goldan, and S. Xie, "Source apportionment of ambient volatile organic compounds in Beijing," *Environ. Sci. Technol.*, vol. 41, no. 12, pp. 4348–4353, 2007.

[21] C. Cai, F. Geng, X. Tie, Q. Yu, and J. An, "Characteristics and source apportionment of VOCs measured in Shanghai, China," *Atmos. Environ.*, vol. 44, no. 38, pp. 5005–5014, 2010.

[22] World Health Organization, "WHO ambient (outdoor) air quality database: Summary results, update 2018," 2018.

[23] U.S. Environmental Protection Agency, "Control of Air Pollution from Motor Vehicles: Tier 3 Motor Vehicle Emission and Fuel Standards," 2014.

[24] California Air Resources Board, *CALIFORNIA 2015 AND SUBSEQUENT MODEL CRITERIA POLLUTANT EXHAUST EMISSION STANDARDS AND TEST PROCEDURES AND 2017 AND SUBSEQUENT MODEL GREENHOUSE GAS EXHAUST EMISSION STANDARDS AND TEST PROCEDURES FOR PASSENGER CARS, LIGHT-DUTY TRUCKS, AND MEDIUM-DUTY VEHIC*. 2012, p. E-5.

[25] J. Wang, L. Jin, J. Gao, J. Shi, Y. Zhao, S. Liu, T. Jin, Z. Bai, and C. Y. Wu, "Investigation of speciated VOC in gasoline vehicular exhaust under ECE and EUDC test cycles," *Sci. Total Environ.*, vol. 445–446, pp. 110–116, 2013.

[26] Y. Nakashima, N. Kamei, S. Kobayashi, and Y. Kajii, "Total OH reactivity and VOC analyses for gasoline vehicular exhaust with a chassis dynamometer," *Atmos. Environ.*, vol. 44, no. 4, pp. 468–475, 2010.

[27] W. Hong-li, J. Sheng-ao, L. Sheng-rong, H. Qing-yao, L. Li, T. Shi-kang, H. Cheng, Q. Li-ping, and C. Chang-hong, "Volatile organic compounds (VOCs) source profiles of on-road vehicle emissions in China," *Sci. Total Environ.*, vol. 607–608, pp. 253–261, 2017.

[28] C. D. Rakopoulos, A. M. Dimaratos, E. G. Giakoumis, and D. C. Rakopoulos, "Evaluation of the effect of engine, load and turbocharger parameters on transient emissions of diesel engine," *Energy Convers. Manag.*, vol. 50, no. 9, pp. 2381–2393, 2009.

[29] E. G. Giakoumis, C. D. Rakopoulos, A. M. Dimaratos, and D. C. Rakopoulos, "Exhaust emissions of diesel engines operating under transient conditions with biodiesel fuel blends," *Prog. Energy Combust. Sci.*, vol. 38, no. 5, pp. 691–715, 2012.

[30] Z. Filipi, H. Fathy, J. Hagena, A. Knafl, R. Ahlawat, J. Liu, D. Jung, D. Assanis, H. Peng, and J. Stein, "Engine-in-the-loop testing for evaluating hybrid propulsion concepts and transient emissions - HMMWV case study," *2006 SAE World Congr.*, vol. 2006, no. 724, 2006.

[31] E. Ericsson, "Variability in urban driving patterns," *Transp. Res. Part D Transp. Environ.*, vol. 5, pp. 337–354, 2000.

[32] B. K. Gullett, A. Touati, L. Oudejans, and S. P. Ryan, "Real-time emission characterization of organic air toxic pollutants during steady state and transient operation of a medium duty diesel engine," *Atmos. Environ.*, vol. 40, no. 22, pp. 4037–4047, 2006.

[33] J. R. Hagena, Z. S. Filipi, and D. N. Assanis, "Transient Diesel Emissions: Analysis of Engine Operation During a Tip-In," *SAE Tech. Pap.*, 2006.

[34] M. Lindgren and P. A. Hansson, "Effects of Transient Conditions on Exhaust Emissions from two Non-road Diesel Engines," *Biosyst. Eng.*, vol. 87, no. 1, pp. 57–66, 2004.

[35] C. D. Rakopoulos, A. M. Dimaratos, E. G. Giakoumis, and D. C. Rakopoulos, "Study of turbocharged diesel engine operation, pollutant emissions and combustion noise radiation during starting with bio-diesel or n-butanol diesel fuel blends," *Appl. Energy*, vol. 88, no. 11, pp. 3905–3916, 2011.

[36] C. D. Rakopoulos, A. M. Dimaratos, E. G. Giakoumis, and D. C. Rakopoulos, "Investigating the emissions during acceleration of a turbocharged diesel engine operating

with bio-diesel or n-butanol diesel fuel blends," *Energy*, vol. 35, no. 12, pp. 5173–5184, 2010.

[37] N. V. Heeb, A. M. Forss, and M. Weilenmann, "Pre- and post-catalyst-, fuel-, velocity- and acceleration-dependent benzene emission data of gasoline-driven EURO-2 passenger cars and light duty vehicles," *Atmos. Environ.*, vol. 36, no. 30, pp. 4745–4756, 2002.

[38] N. V. Heeb, C. J. Saxer, A. M. Forss, and S. Brühlmann, "Trends of NO-, NO2-, and NH3-emissions from gasoline-fueled Euro-3- to Euro-4-passenger cars," *Atmos. Environ.*, vol. 42, no. 10, pp. 2543–2554, 2008.

[39] M. M. Maricq, D. H. Podsiadlik, and R. E. Chase, "Examination of the size-resolved and transient nature of motor vehicle particle emissions," *Environ. Sci. Technol.*, vol. 33, no. 10, pp. 1618–1626, 1999.

[40] G. T. Drozd, Y. Zhao, G. Saliba, B. Frodin, C. Maddox, R. J. Weber, M. C. O. Chang, H. Maldonado, S. Sardar, A. L. Robinson, and A. H. Goldstein, "Time Resolved Measurements of Speciated Tailpipe Emissions from Motor Vehicles: Trends with Emission Control Technology, Cold Start Effects, and Speciation," *Environ. Sci. Technol.*, vol. 50, no. 24, pp. 13592–13599, 2016.

[41] C. A. Gierczak, L. L. Kralik, A. Mauti, A. L. Harwell, and M. M. Maricq, "Measuring NMHC and NMOG emissions from motor vehicles via FTIR spectroscopy," *Atmos. Environ.*, vol. 150, pp. 425–433, 2017.

[42] N. V. Heeb, A. M. Forss, C. Bach, S. Reimann, A. Herzog, and H. W. Jäckle, "A comparison of benzene, toluene and C2-benzenes mixing ratios in automotive exhaust and in the suburban atmosphere during the introduction of catalytic converter technology to the Swiss Car Fleet," *Atmos. Environ.*, vol. 34, no. 19, pp. 3103–3116, 2000.

[43] K. Sentoff, M. Robinson, and B. Holmén, "Second-by-Second Characterization of Cold-Start Gas-Phase and Air Toxic Emissions from a Light-Duty Vehicle," *Transp. Res. Rec. J. Transp. Res. Board*, vol. 2158, pp. 95–104, 2010.

[44] R. Isermann and H. Sequenz, "Model-based development of combustion-engine control and optimal calibration for driving cycles: general procedure and application," *IFAC-PapersOnLine*, vol. 49, no. 11, pp. 633–640, 2016.

[45] M. Benz, M. Hehn, C. H. Onder, and L. Guzzella, "Model-Based Actuator Trajectories Optimization for a Diesel Engine Using a Direct Method," *J. Eng. Gas Turbines Power*, vol. 133, no. 3, p. 032806, 2011.

[46] C. Ericson, B. Westerberg, and R. Egnell, "Transient Emission Predictions With Quasi Stationary Models," *SAE Tech. Pap.*, 2005.

[47] P. J. Maloney, "Objective Determination of Minimum Engine Mapping Requirements for Optimal SI DIVCP Engine Calibration," *SAE Tech. Pap.*, 2009.

[48] J. H. Ng, H. K. Ng, and S. Gan, "Engine-out characterisation using speed-load mapping and reduced test cycle for a light-duty diesel engine fuelled with biodiesel blends," *Fuel*, vol. 90, no. 8, pp. 2700–2709, 2011.

[49] S. Curran, R. Hanson, R. Wagner, and R. D. Reitz, “Efficiency and Emissions Mapping of RCCI in a Light-Duty Diesel Engine,” 2013.

[50] J. D. K. Bishop, M. E. J. Stettler, N. Molden, and A. M. Boies, “Engine maps of fuel use and emissions from transient driving cycles,” *Appl. Energy*, vol. 183, pp. 202–217, 2016.

[51] L. Pelkmans, P. Debal, T. Hood, G. Hauser, and M.-R. Delgado, “Development of a Simulation Tool to Calculate Fuel Consumption and Emissions of Vehicles Operating in Dynamic Conditions,” *SAE Tech. Pap.*, 2004.

[52] Z. Gao, J. C. Conklin, C. S. Daw, and V. K. Chakravarthy, “A proposed methodology for estimating transient engine-out temperature and emissions from steady-state maps,” *Int. J. Engine Res.*, vol. 11, no. 2, pp. 137–151, 2010.

[53] D. Liu, H. Javaherian, O. Kovalenko, and T. Huang, “Adaptive critic learning techniques for engine torque and air-fuel ratio control,” *IEEE Trans. Syst. Man, Cybern. Part B Cybern.*, vol. 38, no. 4, pp. 988–993, 2008.

[54] R. J. Schalkoff, *Artificial neural networks*. New York: McGraw-Hill Higher Education, 1997.

[55] R. F. Turkson, F. Yan, M. K. A. Ali, and J. Hu, “Artificial neural network applications in the calibration of spark-ignition engines: An overview,” *Eng. Sci. Technol. an Int. J.*, vol. 19, no. 3, pp. 1346–1359, 2016.

[56] M. Fischer, *Transient NOx estimation using artificial neural networks*, vol. 46, no. 21. IFAC, 2013.

[57] A. Domínguez-Sáez, G. A. Rattá, and C. C. Barrios, “Prediction of exhaust emission in transient conditions of a diesel engine fueled with animal fat using Artificial Neural Network and Symbolic Regression,” *Energy*, vol. 149, pp. 675–683, 2018.

[58] U.S. Environmental Protection Agency, “Air Toxic Emissions from On-road Vehicles in MOVES2014,” 2016. [Online]. Available: https://www.epa.gov/moves/moves-technical-reports.

[59] U.S. Environmental Protection Agency, “Using MOVES for Estimating State and Local Inventories of Onroad Greenhouse Gas Emissions and Energy Consumption.” [Online]. Available: https://www.epa.gov/moves/moves-technical-reports.

[60] R. K. Maurya and N. Akhil, “Numerical investigation of ethanol fuelled HCCI engine using stochastic reactor model. Part 2: Parametric study of performance and emissions characteristics using new reduced ethanol oxidation mechanism,” *Energy Convers. Manag.*, vol. 121, pp. 55–70, 2016.

[61] Y. Wei, S. Liu, F. Liu, J. Liu, Z. Zhu, and G. Li, “Formaldehyde and methanol emissions from a methanol/gasoline-fueled spark-ignition (SI) engine,” *Energy and Fuels*, vol. 23, no. 6, pp. 3313–3318, 2009.

[62] J. H. Tsai, H. L. Chiang, Y. C. Hsu, H. C. Weng, and C. Y. Yang, “The speciation of volatile organic compounds (VOCs) from motorcycle engine exhaust at different driving

modes," *Atmos. Environ.*, vol. 37, no. 18, pp. 2485–2496, 2003.

[63] H.-J. Hübschmann, *Handbook of GC-MS: Fundamentals and Applications*. 2015.

[64] S. G. Poulopoulos, D. P. Samaras, and C. J. Philippopoulos, "Regulated and unregulated emissions from an internal combustion engine operating on ethanol-containing fuels," *Atmos. Environ.*, vol. 35, no. 26, pp. 4399–4406, 2001.

[65] S. M. Corrêa and G. Arbilla, "Aromatic hydrocarbons emissions in diesel and biodiesel exhaust," *Atmos. Environ.*, vol. 40, no. 35, pp. 6821–6826, 2006.

[66] W. K. Cheng, T. Summers, and N. Collings, "The fast-response flame ionization detector," *Prog. Energy Combust. Sci.*, vol. 24, no. 2, pp. 89–124, 1998.

[67] N. Wright and D. Osborne, "Comparison of Hydrocarbon Measurement with FTIR and FID in a Dual Fuel Locomotive Engine," *SAE Tech. Pap.*, 2016.

[68] S. Machado Corrêa and G. Arbilla, "Carbonyl emissions in diesel and biodiesel exhaust," *Atmos. Environ.*, vol. 42, no. 4, pp. 769–775, 2008.

[69] J. Mohn, A.-M. Forss, S. Brühlmann, K. Zeyer, R. Lüscher, L. Emmenegger, P. Novak, and N. Heeb, "Time-resolved ammonia measurement in vehicle exhaust," *Int. J. Environ. Pollut.*, vol. 22, no. 3, pp. 342–356, 2004.

[70] S. Inomata, H. Yamada, and H. Tanimoto, "Investigation on VOC Emissions from Automobile Sources by Means of Online Mass Spectrometry," *Curr. Pollut. Reports*, vol. 2, no. 3, pp. 188–199, 2016.

[71] F. H. Field, "Chemical Ionization Mass Spectrometry," *Acc. Chem. Res.*, vol. 1, no. 2, pp. 42–49, 1968.

[72] F. K. Tadjimukhamedov and P. B. C. Forbes, *Monitoring of Air Pollutants: Sampling, Sample Preparation and Analytical Techniques*, 70th ed. 2015.

[73] P. Sulzer, A. Edtbauer, E. Hartungen, S. Jürschik, A. Jordan, G. Hanel, S. Feil, S. Jaksch, L. Märk, and T. D. Märk, "From conventional proton-transfer-reaction mass spectrometry (PTR-MS) to universal trace gas analysis," *Int. J. Mass Spectrom.*, vol. 321–322, pp. 66–70, 2012.

[74] Z. Nadir, M. S. Brown, M. L. Comer, and C. A. Bouman, "A Model-Based Iterative Reconstruction Approach to Tunable Diode Laser Absorption Tomography," *IEEE Trans. Comput. Imaging*, vol. 3, no. 4, pp. 876–890, 2017.

[75] G. W. Harris, G. I. Mackay, T. Iguchi, H. I. Schiff, and D. Schuetzle, "Measurement of NO2 and HNO3 in Diesel Exhaust Gas by Tunable Diode Laser Absorption Spectrometry," *Environ. Sci. Technol.*, vol. 21, no. 3, pp. 299–304, 1987.

[76] O. Diemel, R. Honza, C. P. Ding, B. Böhm, and S. Wagner, "In situ sensor for cycle-resolved measurement of temperature and mole fractions in IC engine exhaust gases," *Proc. Combust. Inst.*, vol. 37, no. 2, pp. 1453–1460, 2018.

[77] C. J. Manning and P. R. Griffiths, “Noise Sources in Step-Scan FT-IR Spectrometry,” *Appl. Spectrosc.*, vol. 51, no. 8, pp. 1092–1101, 1997.

[78] H. Li, G. E. Andrews, D. Savvidis, B. Daham, K. Ropkins, M. Bell, and J. Tate, “Comparisons of the Exhaust Emissions for Different Generations of SI Cars under Real World Urban Driving Conditions,” *SAE Tech. Pap.*, 2008.

[79] B. Daham, G. Andrews, H. Li, B. Rosario, M. Bell, and J. Tate, “Application of a portable FTIR for measuring on-road emissions,” *SAE Tech. Pap.*, 2005.

[80] J. P. Szybist, A. L. Boehman, D. C. Haworth, and H. Koga, “Premixed ignition behavior of alternative diesel fuel-relevant compounds in a motored engine experiment,” *Combust. Flame*, vol. 149, pp. 112–128, 2007.

[81] T. J. Truex, J. F. Collins, J. J. Jetter, and B. Knight, “Measurement of Ambient Roadway and Vehicle Exhaust Emissions – An Assessment of Instrument Capability and Initial On-Road Test Results with an Advanced Low Emission Vehicle,” *SAE Tech. Pap.*, 2000.

[82] T. Wallner and R. Frazee, “Study of regulated and non-regulated emissions from combustion of gasoline , alcohol fuels and their blends in a DI-SI engine,” *SAE Tech. Pap.*, 2010.

[83] P. Bielaczyc, J. Woodburn, D. Klimkiewicz, P. Pajdowski, and A. Szczotka, “An examination of the effect of ethanol-gasoline blends’ physicochemical properties on emissions from a light-duty spark ignition engine,” *Fuel Process. Technol.*, vol. 107, pp. 50–63, 2013.

[84] R. Suarez-Bertoa, A. A. Zardini, and C. Astorga, “Ammonia exhaust emissions from spark ignition vehicles over the New European Driving Cycle,” *Atmos. Environ.*, vol. 97, pp. 43–53, 2014.

[85] R. Suarez-Bertoa, A. A. Zardini, V. Lilova, D. Meyer, S. Nakatani, F. Hibel, J. Ewers, M. Clairotte, L. Hill, and C. Astorga, “Intercomparison of real-time tailpipe ammonia measurements from vehicles tested over the new world-harmonized light-duty vehicle test cycle (WLTC),” *Environ. Sci. Pollut. Res.*, vol. 22, pp. 7450–7460, 2015.

[86] D. Wilson and C. Allen, “A Bayesian Estimation Model for Transient Engine Exhaust Characterization Using Fourier Transform Infrared Spectroscopy,” *Energy & Fuels*, vol. 31, no. 10, pp. 11156–11168, 2017.

[87] T. Huai, T. D. Durbin, J. Wayne Miller, and J. M. Norbeck, “Estimates of the emission rates of nitrous oxide from light-duty vehicles using different chassis dynamometer test cycles,” *Atmos. Environ.*, vol. 38, pp. 6621–6629, 2004.

[88] J. V. Candy, *Bayesian Signal Processing: Classical, Modern, and Particle Filtering Methods*. Hoboken, New Jersey: John Wiley and Sons, 2016.

[89] A. H. Mohamed and K. P. Schwartz, “Adaptive Kalman Filtering for INS/GPS,” *J. Geod.*, no. 73, pp. 193–203, 1999.

[90] P. Li, T. Zhang, and B. Ma, “Unscented Kalman filter for visual curve tracking,” *Image*

Vis. Comput., vol. 22, no. 2, pp. 157–164, 2004.

[91] R. Inglesi-Lotz, “The evolution of price elasticity of electricity demand in South Africa: A Kalman filter application,” *Energy Policy*, vol. 39, no. 6, pp. 3690–3696, 2011.

[92] A. J. Volponi, H. Depold, and R. Ganguli, “The Use of Kalman Filter and Neural Network Methodologies in Gas Turbine Performance Diagnostics: A Comparative Study,” *J. Eng. Gas Turbines Power*, vol. 125, pp. 917–924, 2003.

[93] S. J. Julier and J. K. Uhlmann, “A New Extension of the Kalman Filter to Nonlinear Systems,” in *Proceedings of AeroSense: The 11th International Symposium on Aerospace/Defence Sensing, Simulation and Controls*, 1997.

[94] E. A. Wan and R. van der Merwe, “The unscented Kalman filter for nonlinear estimation,” in *Proceedings of the IEEE 2000 Adaptive Systems for Signal Processing, Communications, and Control Symposium*, 2000.

[95] A. Cappiello, I. Chabini, E. K. Nam, A. Lue, and A. Zeid, “A Statistical Model of Vehicle Emissions and Fuel Consumption,” in *The IEEE 5th International Conference on Intelligent Transportation Systems*, 2002, pp. 801–809.

[96] H. Chen and B. Moshfegh, “Comparing k-ε models on predictions of an impinging jet for ventilation of an office room,” in *The 12th International Conference on Air Distribution in Rooms*, 2011.

[97] M. Adachi, “Emission measurement techniques for advanced powertrains,” *Meas. Sci. Technol.*, vol. 11, no. 10, pp. R113–R129, 2000.

[98] K. K. C. Yu, N. R. Watson, and J. Arrillaga, “An adaptive Kalman filter for dynamic harmonic state estimation and harmonic injection tracking,” *IEEE Trans. Power Deliv.*, vol. 20, no. 2, pp. 1577–1584, 2005.

[99] L. Jetto, S. Longhi, and G. Venturini, “Development and experimental validation of an adaptive extended Kalman filter for the localization of mobile robots,” *IEEE Trans. Robot. Autom.*, vol. 15, no. 2, pp. 219–229, 1999.

[100] P. R. Griffiths and J. A. De Haseth, *Fourier Transform Infrared Spectrometry*. New York: John Wiley & Sons Inc., 1986.

[101] F. Zhang, J. Wang, D. Tian, J.-X. Wang, and S.-J. Shuai, “Research on Unregulated Emissions from an Alcohols-Gasoline Blend Vehicle Using FTIR, HPLC and GC-MS Measuring Methods,” *SAE Int. J. Engines*, vol. 6, no. 2, pp. 2013-01-1345, 2013.

[102] R. Penteado, L. Daemme, and T. Melo, “An Experimental Investigation on Regulated and Unregulated Emissions from Four 4-Stroke Gasoline-Powered Motorcycle,” 2012.

[103] M. S. Peckham, A. Finch, and B. Campbell, “Analysis of Transient HC, CO, NOx and CO2 Emissions from a GDI Engine using Fast Response Gas Analyzers,” *SAE Int. J. Engines*, vol. 4, no. 1, pp. 2011-01-1227, 2011.

[104] MKS Instruments Inc., “MKS MG2000^{TM} Software Manual.” Wilmington, MA, 2015.

[105] California Air Resources Board, “Toxic Air Contaminant Identification List,” 2011. [Online]. Available: https://www.arb.ca.gov/toxics/id/taclist.htm.

[106] C. L. Myung, K. Choi, J. Kim, Y. Lim, J. Lee, and S. Park, “Comparative study of regulated and unregulated toxic emissions characteristics from a spark ignition direct injection light-duty vehicle fueled with gasoline and liquid phase LPG (liquefied petroleum gas),” *Energy*, vol. 44, no. 1, pp. 189–196, 2012.

APPENDIX

4.2.2 – Proof of Validity of Absorbance Evolution Slope Calculation of Equation 4-14

To estimate the magnitude of centerburst weighting during a FTIR measurement, a normalized absorbance slope (γ) with respect to OPD must be selected to simulate the effects of non-stationarity. In Equation 4-14, γ is calculated so that absorbance is initially equal to the spectrum $A_{\nu,cal,1}$ at the centerburst position, and evolves to become the final spectrum $A_{\nu,cal,2}$ at the maximum OPD (δ). However, Equation 4-14 uses the calibrated versions of these spectra ($\hat{A}_{\nu,cal,1}$ and $\hat{A}_{\nu,cal,2}$) – which are altered by the effects of truncation and apodization – to calculate these slopes, as the true spectra are unknown. However, as long as the relative slopes across wavenumbers are consistent (i.e. γ is a scalar), Equation 4-14 yields the true value for γ. The following is a proof of this conjecture.

Consider the following equation relating the true initial and final spectra and the absorbance slope γ. This equation fulfills the requirements laid out in the previous paragraph.

$$A_{\nu,cal,2}(\nu) - A_{\nu,cal,1}(\nu) = \gamma\delta A_{\nu,cal,1}(\nu) \tag{A-1}$$

Since both sides of Equation 4-1 are themselves spectra, they can be convolved with the truncation/apodization spectrum $D(\nu)$. This spectrum simulates the effects of truncation/apodization.

$$\left(A_{\nu,cal,2}(\nu) - A_{\nu,cal,1}(\nu)\right) \ * \ D(\nu) = \gamma\delta A_{\nu,cal,1}(\nu) \ * \ D(\nu) \tag{A-2}$$

The convolution operation is distributive, allowing the both spectra on the left-hand side to be convolved with $D(\nu)$ separately. Furthermore, convolutions are also associative with respect to scalars, allowing the total, relative power evolution to be pulled from the convolution. These updates are applied in Equation A-3.

$$A_{\nu,cal,2}(\nu) * D(\nu) - A_{\nu,cal,1}(\nu) * D(\nu) = \gamma\delta\left(A_{\nu,cal,1}(\nu) * D(\nu)\right) \tag{A-3}$$

Each true spectra in A-3 is convolved individually with the truncation/apodization spectrum, yielding the known calibration spectra as shown in Equation A-4. Notice that this equation is identical to Equation A-1, with the only exception being that true absorbance spectra are replaced by calibrations.

$$\hat{A}_{\nu,cal,2}(\nu) - \hat{A}_{\nu,cal,1}(\nu) = \gamma\delta\hat{A}_{\nu,cal,1}(\nu) \qquad \text{(A-4)}$$

Thus, the scalar absorbance slopes calculated from calibration spectra are identical to the true absorbance slopes during a FTIR scan.

$$\gamma = \frac{A_{\nu,cal,2}(\nu) - A_{\nu,cal,1}(\nu)}{A_{\nu,cal,1}(\nu)\delta} = \frac{\hat{A}_{\nu,cal,2}(\nu) - \hat{A}_{\nu,cal,1}(\nu)}{\hat{A}_{\nu,cal,1}(\nu)\delta} \qquad \text{(A-5)}$$

Therefore, as long as γ is indeed somewhat consistent across wavenumbers, Equation 4-14 should yield reasonable approximations of absorbance profiles with respect to OPD for linearly evolving compositions during FTIR scans.

5.1.2 – Emissions Maps

Presented in this section are illustrations of the steady-state emissions maps used to formulate the quasi-steady emissions and emissions stochasticity models for each species from Chapter 5. These maps are generated using the average and standard deviation of emissions during each steady-state experiment at each speed/load point.

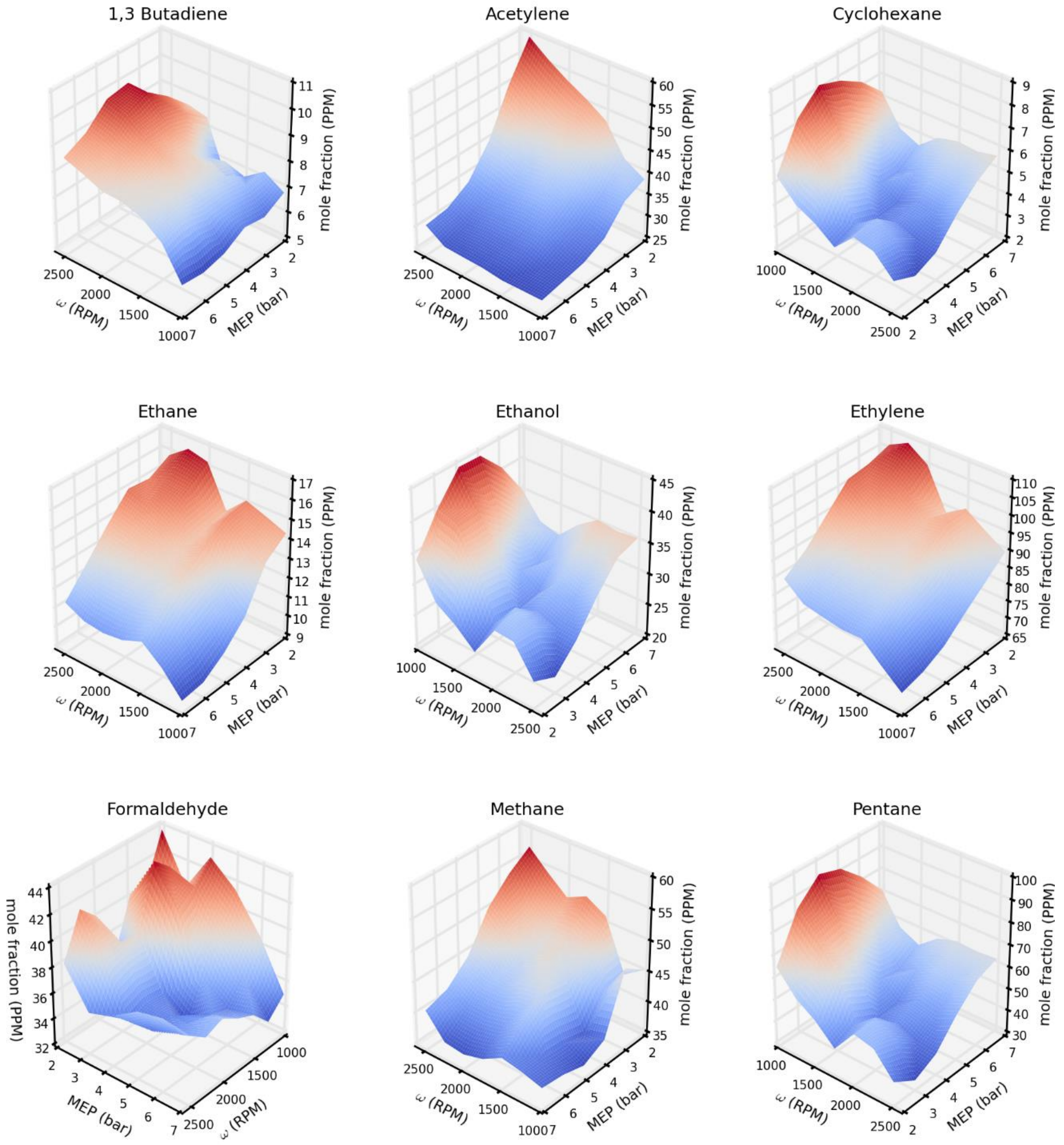

Figure A-1: Steady-state emissions maps for each species with respect to engine speed and load.

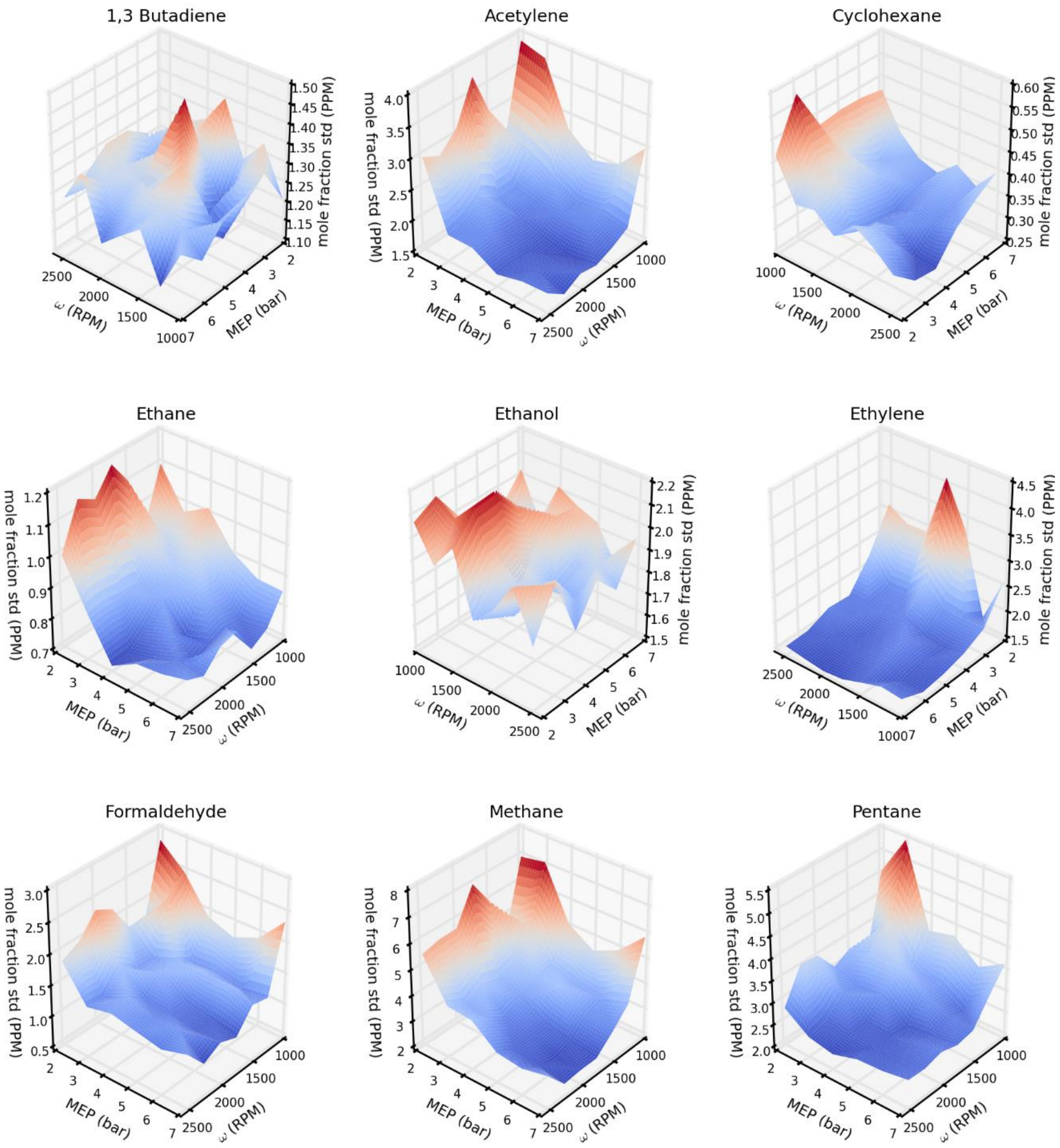

Figure A-2: Map of estimated stochastic emissions fluctuation standard deviation for each species with respect to engine speed and load.

5.3 – Experimental Emissions Data at an Engine Speed of 2000 RPM

Provided herein are experimental emissions data and quasi-steady predictions from Chapter 5 for experiments where the engine speed setting is 2000 rpm. This data is omitted from the body of the dissertation due to its similarity to the 1500 rpm data and to maintain concision.

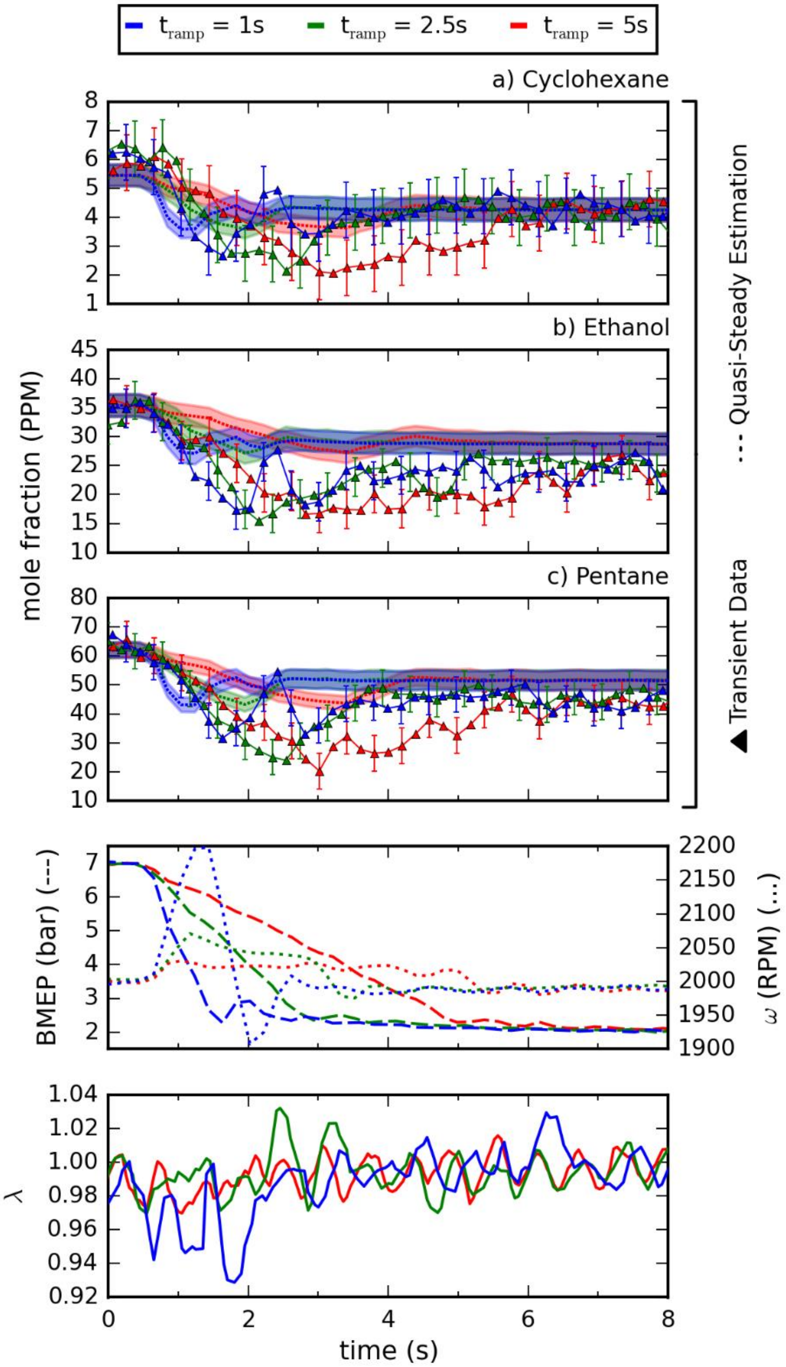

Figure A-3: Emissions of various fuel components, engine speed/load and air-fuel equivalence ratio for the downward ramp load profile, 2000 rpm case. Error bars reflect the uncertainty standard deviation of a transient emissions estimation from a FTIR measurement. The shaded area surrounding the quasi-steady predictions represents the estimated standard deviation of stochastic emissions fluctuations for the current engine speed/load.

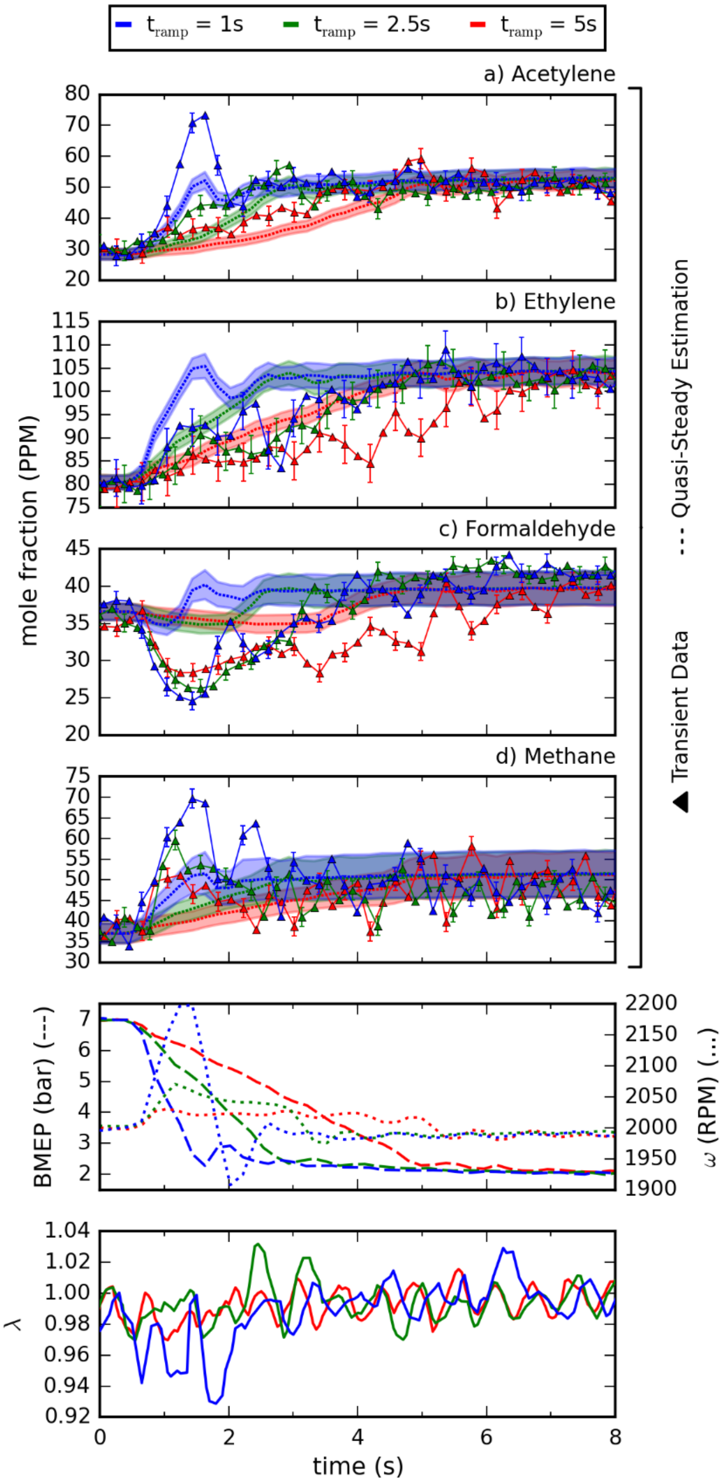

Figure A-4: Emissions of various intermediates, engine speed/load and air-fuel equivalence ratio for the downward ramp load profile, 2000 rpm case. Error bars reflect the uncertainty standard deviation of a transient emissions estimation from a FTIR measurement. The shaded area surrounding the quasi-steady predictions represents the estimated standard deviation of stochastic emissions fluctuations for the current engine speed/load.

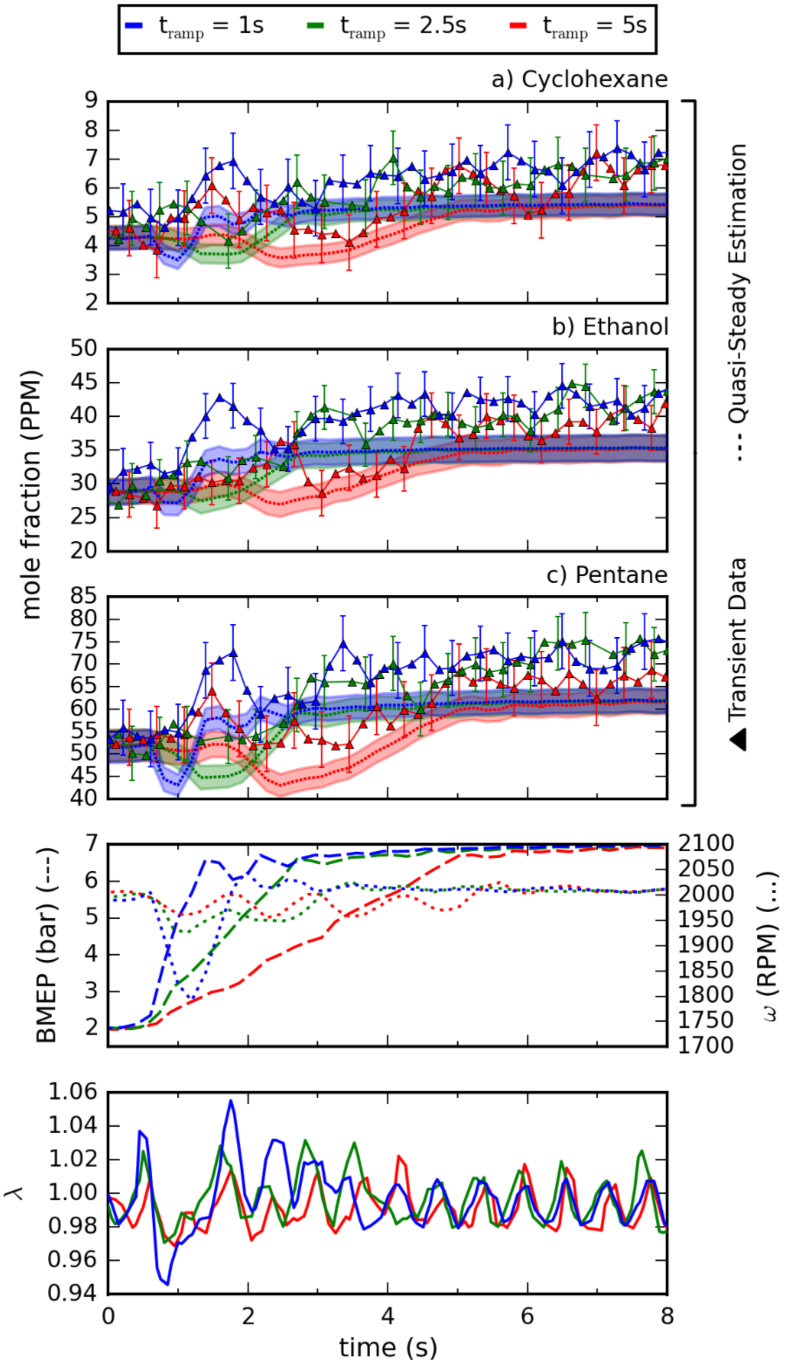

Figure A-5: Emissions of various fuel components, engine speed/load and air-fuel equivalence ratio for the upward ramp load profile, 2000 rpm case. Error bars reflect the uncertainty standard deviation of a transient emissions estimation from a FTIR measurement. The shaded area surrounding the quasi-steady predictions represents the estimated standard deviation of stochastic emissions fluctuations for the current engine speed/load.

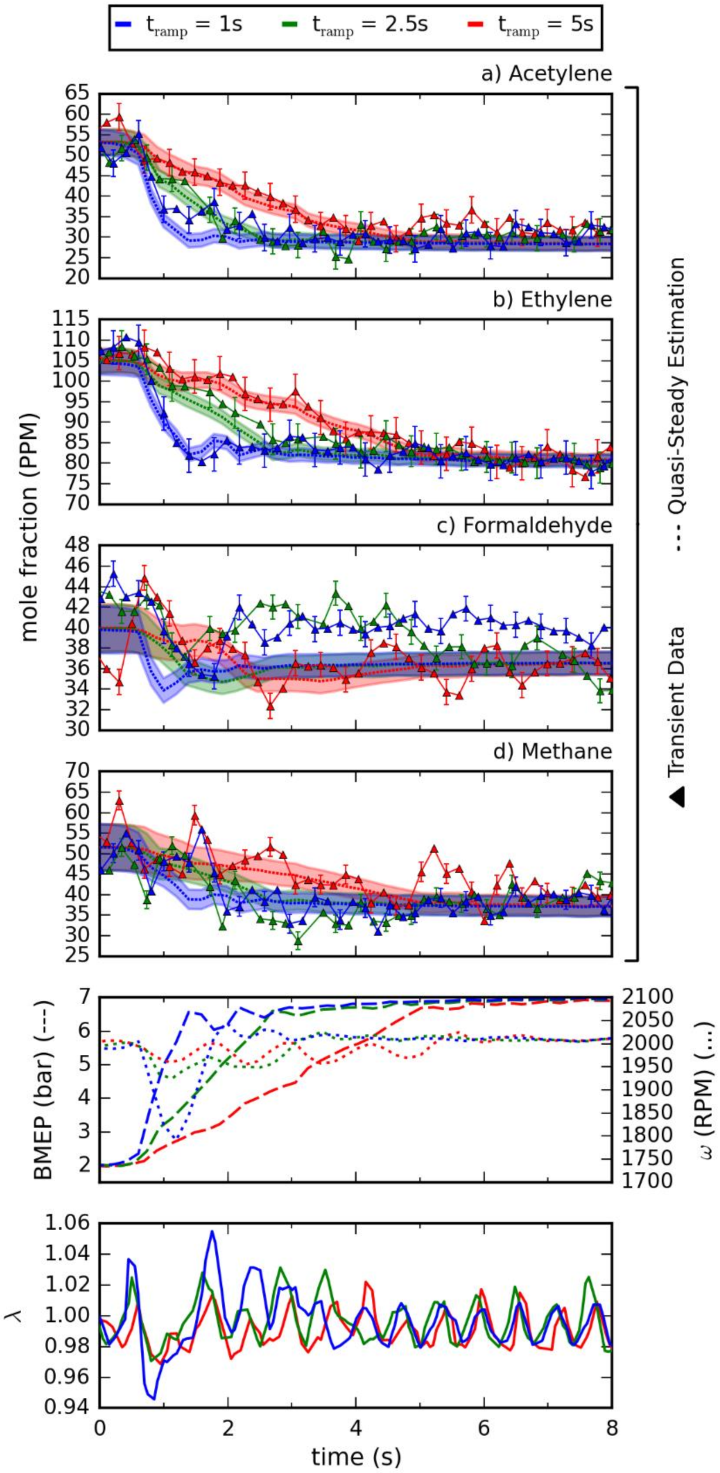

Figure A-6: Emissions of various intermediates, engine speed/load and air-fuel equivalence ratio for the upward ramp load profile, 2000 rpm case. Error bars reflect the uncertainty standard deviation of a transient emissions estimation from a FTIR measurement. The shaded area surrounding the quasi-steady predictions represents the estimated standard deviation of stochastic emissions fluctuations for the current engine speed/load.

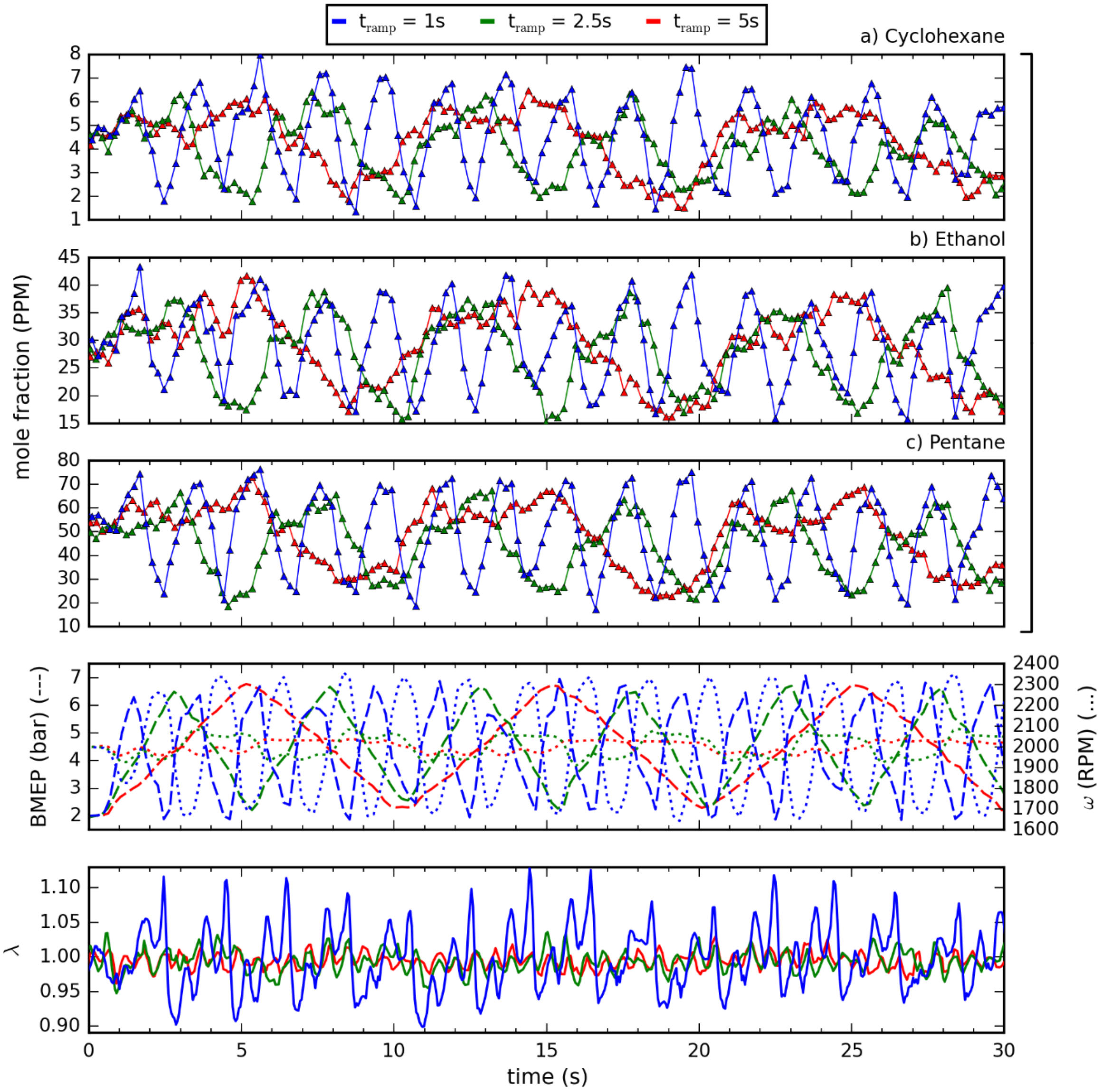

Figure A-7: Emissions of various fuel components, engine speed/load and air-fuel equivalence ratio for the wave load profile, 2000 rpm case.

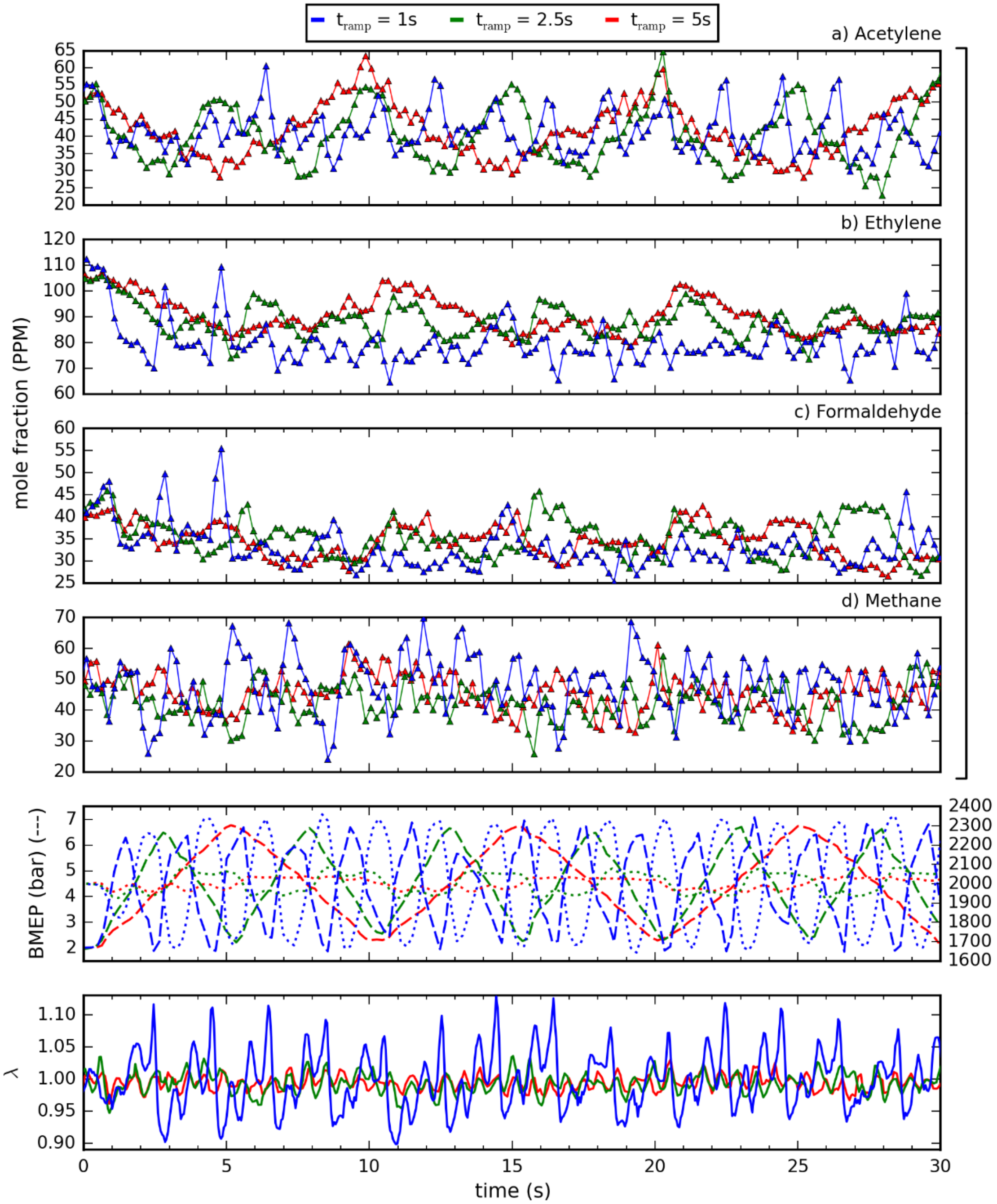

Figure A-8: Emissions of various intermediates, engine speed/load and air-fuel equivalence ratio for the wave load profile, 2000 rpm case.